

## ABSTRACT

PADGETT, ASHLY BROOK. Terrestrial Paleoclimate and Geology during Unusual Climate States – Utilizing Isotope Geochemistry across Ellesmere and Axel Heiberg Islands, Arctic Canada (Under the direction of Dr. Ethan G. Hyland).

Terrestrial proxy data for sensitive polar regions like the Canadian Arctic during past warm intervals are currently limited. Developing accurate records of paleoclimate and paleoenvironments during past warm periods like the late Paleocene and early Eocene is necessary to predict potential consequences of future anthropogenic warming, particularly in polar regions that may experience dramatic responses to climate change due to their role in carbon storage and surface albedo feedbacks. Ellesmere and Axel Heiberg Islands in the Canadian Arctic preserve long-term paleoclimate and geologic archives in terrestrial fluvio-deltaic, floodplain, and paludal deposits from the late Paleocene to middle Eocene (approximately 59 to 45 Ma). This work expands on existing stratigraphic, paleontological, and natural resource explorations from the Canadian Arctic Archipelago through the addition of stable ( $\delta^{13}\text{C}$ ,  $\delta^{18}\text{O}$ ) and clumped ( $\Delta_{47}$ ) isotope analyses on palustrine carbonates.

$\delta^{13}\text{C}$  isotope values range from -4.6 to +12.3‰ (VPDB), and  $\delta^{18}\text{O}$  isotope values range from -23.1 to -15.2‰ (VPDB). Samples are classified into four fabric types: Micritic, Micritic to Microspar, Microspar, and Sparry, with carbon isotopic values ( $\delta^{13}\text{C}$ ) averaging 9.8‰, 4.5‰, 3.4‰, 2.0‰, and oxygen isotopic values ( $\delta^{18}\text{O}$ ) averaging -17.2‰, -17.8‰, -18.0‰, -18.9‰ respectively. Both carbon and oxygen stable isotope averages decrease with an increased level of alteration. Unusually positive carbon isotope values suggest carbonates experienced repeated dissolution-precipitation enrichment cycles. Arctic monsoonal conditions may have resulted in summer carbonate dissolution due to significant rainfall followed by winter carbonate re-precipitation. Clumped ( $\Delta_{47}$ ) isotope values range from 0.505 to 0.621‰ (CDES), with resulting

temperature estimates from 52 to 121 °C. Temperatures were on average hotter for samples that had experienced greater alteration (Spar and Microspar, 86 °C; Micritic and Micritic-to-Microspar, 60 °C). Isotopic values and carbonate fabrics indicate burial-related diagenetic recrystallization for many samples, and solid-state reordering of clumped isotopes occurred during a regional burial event.  $\Delta_{47}$  values were used to model maximum burial temperatures spatially across Axel Heiberg and Ellesmere Islands. Temperature variability at sample locations corresponds to faults, which resulted in differential cooling of surfaces following the Eurekan Orogeny. Clumped isotope-derived burial temperatures (104 to 171 °C) generally agree with other thermal maturity studies for the area and can serve as a method complementary to apatite fission track thermochronometry and vitrinite reflectance for sedimentary basin diagenetic temperature reconstruction.

© Copyright 2020 by Ashly Padgett

All Rights Reserved

Terrestrial Paleoclimate and Geology during Unusual Climate States – Utilizing Isotope  
Geochemistry across Ellesmere and Axel Heiberg Islands, Arctic Canada

by  
Ashly Brook Padgett

A thesis submitted to the Graduate Faculty of  
North Carolina State University  
in partial fulfillment of the  
requirements for the degree of  
Master of Science

Marine, Earth, and Atmospheric Sciences

Raleigh, North Carolina  
2020

APPROVED BY:

---

Dr. Ethan G. Hyland  
Committee Chair

---

Dr. Karl W. Wegmann

---

Dr. Elana L. Leithold

## **DEDICATION**

To my world: Audry, Amber, and Alex for always being there for me through everything, I love you so much. To my parents for sacrificing so much to provide me with a great life and education, I am forever grateful for your support. And to my best friends Esther, Peter, Katie, Lillian, and Sandrine for making my time in college wonderful years filled with incredible memories.

## **BIOGRAPHY**

Growing up, I moved nine different times and lived across the United States and overseas in Europe and Asia. I consider Seattle to be my home, where I graduated from the University of Washington in 2016, and lived prior to moving to Raleigh for my Master's degree at North Carolina State University. I am a music-lover, runner, and rabid Seattle Seahawks fan.

## ACKNOWLEDGMENTS

I would like to thank my advisor and committee chair, Dr. Ethan Hyland for the help and mentorship throughout this process. I would also like to thank committee members Dr. Lonnie Leithold and Dr. Karl Wegmann for their advice and support. I am extremely grateful to have had the opportunity to learn and receive guidance from such a knowledgeable committee. I am also very grateful for the insightful feedback of collaborators Dr. Landon Burgener and Dr. Christopher West. I would like to acknowledge collaborators Dr. David Greenwood, Dr. James Basinger, and the University of Saskatchewan's Paleobotanical Collection (USPC) for providing the Arctic samples used in this research study. Thank you Dr. Greg Tierney and Katie Boaggio, I am so grateful for your advice and support. I appreciate the project funding from the Geological Society of America Graduate Student Research Grant and NCSU Marine, Earth, and Atmospheric Sciences Department Graduate Student Association Research Grant. I would also like to acknowledge IsoLab, at the University of Washington Earth and Space Sciences Department, for running initial samples to compare to our data results. An additional thank you to the members of the Paleo<sup>3</sup> Research Group at North Carolina State University for their lab assistance and suggestions. Finally, thank you so much to my wonderful and selfless friends; I am very appreciative of your support!

## TABLE OF CONTENTS

LIST OF TABLES .....	vii
LIST OF FIGURES .....	viii
<b>1. Introduction</b> .....	<b>1</b>
1.1. Research Motivation .....	1
1.2. Thesis Purpose .....	2
<b>2. Background</b> .....	<b>4</b>
2.1. Late Paleocene and Early Eocene Climate .....	4
2.1.1. Existing Arctic Isotope and Climate Data .....	5
2.1.2. Arctic Monsoonal Climate Debate.....	6
2.1.3. Existing Arctic Paleontological Data.....	7
2.2. Nunavut Geologic Background.....	8
2.2.1. Current Setting.....	8
2.2.2. Sverdrup Basin Geologic History .....	9
2.2.3. Eureka Sound Group Stratigraphy .....	11
2.2.4. Eureka Sound Group Samples .....	17
2.3. Stable and Clumped Isotope Geochemistry.....	17
2.3.1. Palustrine Carbonate Formation .....	17
2.3.2. Stable Isotopes in Palustrine Carbonates .....	18
2.3.2.a. Primary Features .....	19
2.3.2.b. Secondary Features .....	20
2.3.3. Carbonate Clumped Isotopes .....	24
2.3.3.a. Clumped Isotope Complications .....	25
2.3.3.b. Reordering for Burial History .....	25
2.3.3.c. Secondary Carbonate $\Delta_{47}$ for Diagenetic History .....	26
<b>3. Methodology</b> .....	<b>27</b>
3.1. Physical Collection .....	27
3.2. Sample Evaluation .....	28
3.3. Analytical Methods.....	32
<b>4. Results</b> .....	<b>33</b>
4.1. Sample Descriptions .....	33
4.2. Stable Isotopes .....	33
4.3. Clumped Isotopes.....	39
<b>5. Discussion</b> .....	<b>42</b>
5.1. Sample Interpretations .....	42
5.2. Primary Carbonate Stable Isotope Interpretations .....	43
5.2.1. Primary Carbon Isotopes.....	43
5.2.2. Primary Oxygen Isotopes.....	47
5.3. Secondary Carbonate Stable Isotope Interpretations .....	49
5.4. Clumped Isotope Interpretations.....	50
5.4.1. Reordering Burial Temperatures.....	51
5.4.1.a. Reordering Model Parameters.....	53
5.4.1.b. Reordering Model Output .....	55
5.4.2. Spar Formation Burial Temperatures.....	57
5.4.3. Comparing $\Delta_{47}$ Burial Temperatures to Past Thermal Reconstructions .....	62

5.4.4. Basin Dynamics and Cooling Story .....	68
<b>6. Conclusions</b> .....	69
6.1. Data Summary .....	69
6.2. Concluding Thesis Objectives .....	69
<b>References</b> .....	73
<b>Appendices</b> .....	84
Appendix A. Clumped Isotope Reordering Model .....	85
Appendix B. Listed Data Output .....	88

**LIST OF TABLES**

Table 1.	Table of alteration approximations and sample fabrics.....	29
Table 2.	Stable Isotope Data.....	34
Table 3.	Clumped Isotope Data.....	39
Table 4.	Table of calculated burial temperatures. Spar formation temperatures (Spar Formation °C) were derived by using a micrite and diagenetic spar two-component end-member mixing model. Reordering temperatures (Reordering Temp °C) were derived by using a model of the predictable clumped isotope reordering rate associated with prolonged burial heating. Both “Spar Formation” and “Reordering Temp” provide a burial temperature for heated Eureka Sound Group deposits.....	62

## LIST OF FIGURES

- Figure 1. Maps of Axel Heiberg and Ellesmere Islands.  
 A) Topographic sample map for Axel Heiberg and Ellesmere Islands. Axel Heiberg Island contains the sample locations: Buc and Strd. Ellesmere Island contains the sample locations: Haz, HW, Mos, FAW, FAE, Sthc, Splt, and Stk. Sample locations are displayed on the topographic map in a yellow color gradient corresponding to the localities on the stratigraphic column: Stenkul Fiord, Split Lake, Axel Heiberg, Strathcona Fiord, Fosheim Peninsula, and Lake Hazen. Topographic data from GeoMapApp (Ryan et al., 2009). B) Map of sample placement at sample localities. Map on the right. Blue points show each sample, and circles in the yellow color gradient correspond to the sample localities used in Figure 3. .... 3
- Figure 2. Placement of Sverdrup Basin over the Canadian Arctic Archipelago. Shaded islands are the Canadian Arctic Archipelago in the Nunavut territory. The black lines show approximate outline of the Sverdrup Basin. Deformation is shown by pink (highly deformed), yellow (mildly deformed), and green (very mild deformation). Clastic sediment source areas are shown by arrows and labels. Information from Embry & Beuchamp (2008). .... 9
- Figure 3. Simplified stratigraphic column with sample placement. Stratigraphic column displaying relevant formations (Mt. Lawson, Mt. Moore, Margaret, Mokka Fiord, and Buchanan Lake Formations) within the Eureka Sound Group and the approximate sample ages. Yellow color gradient corresponds to map localities. Base column created by West (2019) and adapted to the samples. Pink shaded regions indicate major climatic events. .... 13
- Figure 4. Sverdrup Basin sequence stratigraphy and environmental reconstructions. Displayed through the mid-Paleocene, late Paleocene, early Eocene, and middle Eocene. Base illustrations taken directly from Ricketts & Stephenson (1994) and superimposed with some sample locations highlighted during the times they were deposited or altered. The yellow color gradient corresponds to the map (Figure 1) and stratigraphic column (Figure 3). .... 16
- Figure 5. Plain light images of thin sections. Microscope image size is 700  $\mu\text{m}$  by 400  $\mu\text{m}$ , and images are of a random location in the middle of each slide with no specific features highlighted. Pictures beneath each microscope image is a zoomed out thin section photograph, approximately 22 mm by 8 mm. Sample localities are marked by a dot in the yellow color gradient corresponding to Figures 1 and 3, and sample fabric is labeled by a green, yellow, orange, or red box. .... 30

Figure 6.	Sample placement map displaying carbonate fabrics. Circles in the yellow color gradient correspond to the sample localities used in Figure 3. Sample names and locations are labeled at each point. (Mic = green, Mic/MSp = yellow, MSp = orange, Spar = red).....	31
Figure 7a.	Visual Alteration Coefficient vs. carbon isotope compositions.....	34
Figure 7b.	Visual Alteration Coefficient vs. oxygen isotope compositions.....	35
Figure 8a.	Stable carbon isotope data plotted against fabric classification. Isotope data averaged within each fabric type, vertical lines show standard deviation .....	35
Figure 8b.	Stable oxygen isotope data plotted against fabric classification. Isotope data averaged within each fabric type, vertical lines show standard deviation .....	36
Figure 9a.	Stable carbon isotope data plotted spatially on Ellesmere and Axel Heiberg. Stable isotope data plotted spatially alongside location code and visual alteration class (Mic = green, Mic/MSp = yellow, MSp = orange, Spar = red).....	37
Figure 9b.	Stable oxygen isotope data plotted spatially on Ellesmere and Axel Heiberg. Stable isotope data plotted spatially alongside location code and visual alteration class (Mic = green, Mic/MSp = yellow, MSp = orange, Spar = red).....	38
Figure 10.	Plot of $T(\Delta_{47})$ versus Visual Alteration Coefficient.....	40
Figure 11.	Clumped isotope-derived temperatures plotted spatially. Temperatures plotted alongside visual alteration class (Mic = green, Mic/MSp = yellow, MSp = orange, Spar = red) and locality zone (yellow color gradient ellipses correspond to Figures 1 and 3).....	41
Figure 12.	Regional burial and uplift signal modeled within the micritic samples. The general time approximations of burial and uplift for the region were used to assign each event duration. LP-EE samples shows the timing of late Paleocene to early Eocene samples, while Mid E sample shows the timing of the middle Eocene sample. Thermal events and tectonic settings information directly taken from Figure 2 in Dewing & Sanei (2009). .....	52
Figure 13a.	Clumped Isotope Reordering Model for late Paleocene to early Eocene. US261: 0.589‰ in green, US438: 0.596‰ in red, US191: 0.589‰ in cyan. Heating a carbonate (formed at $2^\circ\text{C} = 0.7651\text{‰}$ ) to a maximum burial temperature of $156^\circ\text{C}$ results in a reordered $\Delta_{47}$ value of 0.621‰, $157.5^\circ\text{C}$ results in a reordered $\Delta_{47}$ value of 0.596‰, and $158^\circ\text{C}$ results in a reordered $\Delta_{47}$ value of 0.589‰.....	56

- Figure 13b. Clumped Isotope Reordering Model for Middle Eocene. US119 in purple. Heating a carbonate (formed at  $2\text{ }^{\circ}\text{C} = 0.7651\text{‰}$ ) to a maximum burial temperature of  $155\text{ }^{\circ}\text{C}$  results in a reordered  $\Delta_{47}$  value of  $0.604\text{‰}$ . ..... 57
- Figure 14. A spatial plot of calculated maximum burial temperatures. Sample locations with two spar formation temperatures were averaged for clarity. Faults nearby sample locations are shown on the map in light blue, and crosses over the hexagons and triangles if it cuts through the sample locations. Temperatures less than  $125\text{ }^{\circ}\text{C}$  are shown in dark blue, temperatures greater than  $125\text{ }^{\circ}\text{C}$  are shown in dark red. Fault locations are taken from Figure 40.1 in Harrison et al. (2011), and only relevant faults nearby sample locations are shown here. .... 60
- Figure 15. Maximum burial temperatures plotted with vitrinite reflectance temperatures. Clumped isotope burial temperature approximations (in  $^{\circ}\text{C}$ ) for the Eureka Sound Group (approximated from reordering and diagenetic spar formation temperatures) plotted alongside Arne et al. (2002) vitrinite maximum temperature approximations prior to cooling. .... 64
- Figure 16.  $\Delta_{47}$  burial temperature ranges and vitrinite-derived maximum burial temperature ranges across Fosheim Peninsula. On a north to south transect across Fosheim Peninsula, the vitrinite wells (purple diamonds) are Neil O-15 (immediately North of Fosheim Peninsula), Taleman J-34 (upper middle Fosheim Peninsula); Fosheim N-27 (lower middle Fosheim Peninsula); and Depot Point L-24 (immediately South of Fosheim Peninsula), vitrinite data from Arne et al. (2002). From north to south, the clumped isotope samples (teal circles) compared were Hot Weather Creek (HW;  $145\text{ }^{\circ}\text{C}$ ), Mosquito Creek (Mos;  $104\text{ }^{\circ}\text{C}$ ), Fosheim Anticline East (FAE;  $171\text{ }^{\circ}\text{C}$ ), and Fosheim Anticline West (FAW;  $170\text{ }^{\circ}\text{C}$ ). Clumped range includes model uncertainty. .... 66
- Figure 17. Crossplot of vitrinite burial temperature averages by  $\Delta_{47}$  burial temperatures for Fosheim Peninsula. Vitrinite wells are Neil O-15 ( $\sim 120\text{ }^{\circ}\text{C}$ ), Taleman J-34 ( $\sim 93\text{ }^{\circ}\text{C}$ ); Fosheim N-27 ( $\sim 158\text{ }^{\circ}\text{C}$ ); and Depot Point L-24 ( $\sim 158\text{ }^{\circ}\text{C}$ ), vitrinite data from Arne et al. (2002). Compared clumped isotope samples were Hot Weather Creek (HW;  $145\text{ }^{\circ}\text{C}$ ), Mosquito Creek (Mos;  $104\text{ }^{\circ}\text{C}$ ), Fosheim Anticline East (FAE;  $171\text{ }^{\circ}\text{C}$ ), and Fosheim Anticline West (FAW;  $170\text{ }^{\circ}\text{C}$ ). Error bars shows the  $-30\text{ }^{\circ}\text{C}$  uncertainty of the spar formation model results. .... 67

## 1. INTRODUCTION

### 1.1. Research Motivation

Future warming, driven by increased greenhouse gas concentrations, will be accompanied by global changes in precipitation patterns and ecology. Increased heat storage and thermal expansion of oceans, coupled with meltwater input from mountain glaciers, small ice caps, and Arctic sea ice, will drive significant global sea-level rise into coastlines and displace people globally (Melillo, 2014; IPCC, 2013).

A comprehensive understanding of climate dynamics during warming events is necessary to inform predictive climate models and make future policy decisions (IPCC, 2007). While there are currently climate records for these analogue warm periods, these are often global averages from marine environments, which may experience a lag behind terrestrial environments (Mix & Ruddiman, 1984). Additionally, terrestrial regions change faster and more heterogeneously than marine environments, and thus terrestrial records are necessary to obtain a comprehensive understanding of ecological response to rapid climate shifts (e.g., Diffenbaugh, 2013).

During rapid warming events, polar regions respond dramatically and can further influence the global climate through carbon storage and surface albedo feedbacks (e.g., Zimov et al., 2006; Guemas et al., 2013; IPCC, 2007). Additionally, early Cenozoic climate models struggle to reconstruct warm polar conditions, even with significant increases to the preindustrial  $p\text{CO}_2$  concentrations (e.g., Shellito et al., 2003; Shellito & Sloan, 2006; Winguth et al., 2010). Differences in the marine and terrestrial response to increased  $p\text{CO}_2$  concentrations are poorly constrained due to a lack of proxy records from high latitude areas. Increasing the amount of high latitude data available will improve understanding of climate response during analogue warm periods and make possible the characterization of the early Eocene climate gradient. Our

proxy records will contribute to a large-scale effort to reconstruct latitudinal climate gradients from the tropics to poles during greenhouse periods, which could be applied within current models of our climate system and improve climate forecasting (Greenwood & Wing, 1995; Price & Passey, 2013).

Therefore, obtaining polar terrestrial proxy records for analogue warm periods is necessary to better constrain potential future consequences of anthropogenic warming, and will help clarify discrepancies between global climate models, marine climate records, and paleontological climate estimates in the Arctic (McInerney & Wing, 2011).

## **1.2. Thesis Purpose**

This thesis interprets stable and clumped isotopic data from complex and altered palustrine carbonate rocks from Axel Heiberg and Ellesmere Islands (Figure 1). Stable isotope data are applied to assess the paleoclimate during the late Paleocene and early Eocene. Clumped isotope data are applied in models to obtain subsurface temperatures to better understand the Sverdrup Basin diagenetic history. Evaluating isotopic compositions alongside these islands' complex geologic history and detailed paleontological records improves our understanding of terrestrial polar conditions.

### Overarching Research Questions:

1. Is it possible to use the isotope geochemistry of rocks that have undergone burial and partial deformation to obtain reliable paleoclimate proxy data?
2. What does the stable isotope data suggest about the climate on Ellesmere and Axel Heiberg Islands during the late Paleocene and early Eocene Epochs?
3. Is it possible to apply clumped isotope temperature data in models to derive burial temperatures and geologic information about the Sverdrup Basin?

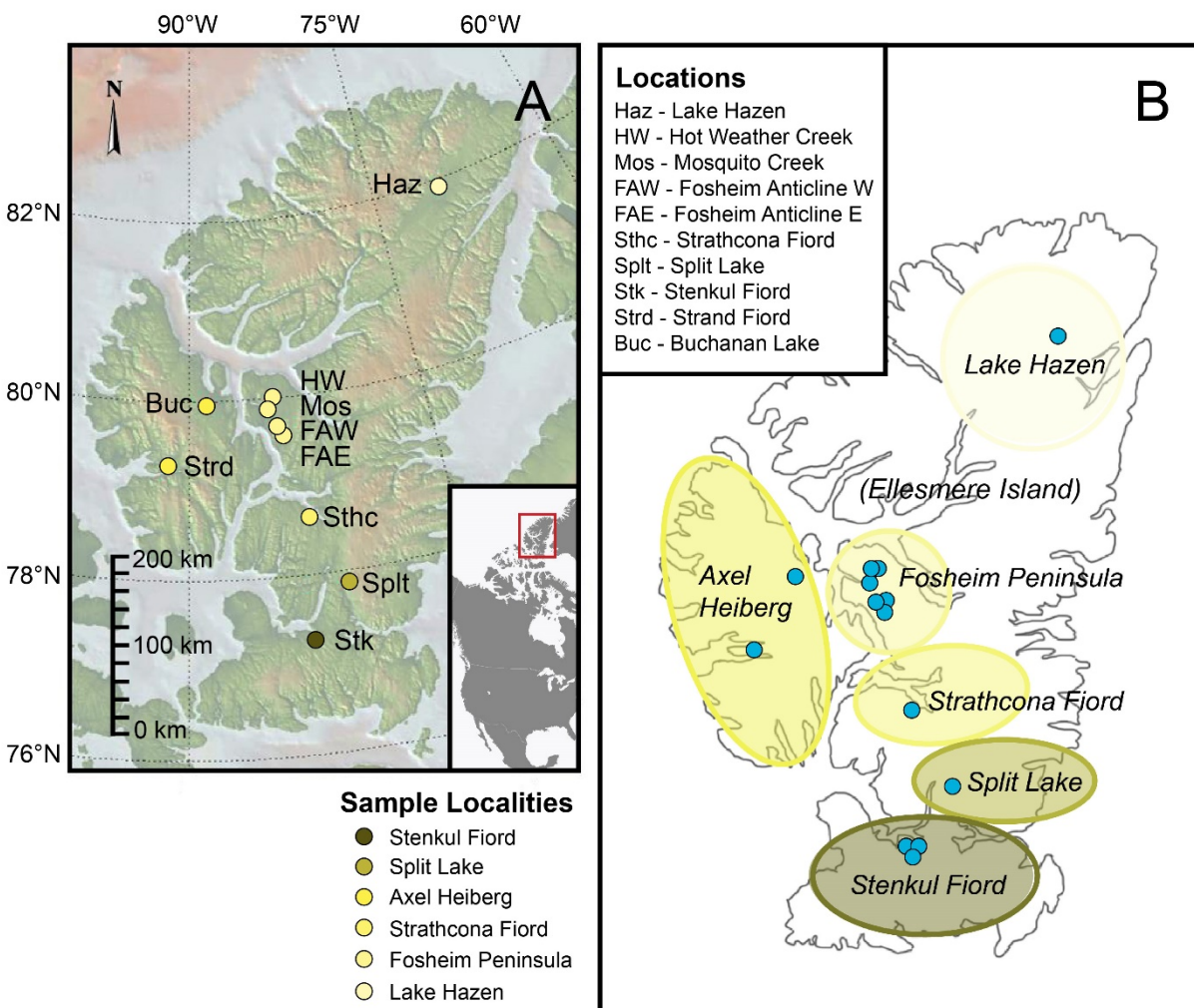


Figure 1. Maps of Axel Heiberg and Ellesmere Islands.

A) Topographic sample map for Axel Heiberg and Ellesmere Islands. Axel Heiberg Island contains the sample locations: Buc and Strd. Ellesmere Island contains the sample locations: Haz, HW, Mos, FAW, FAE, Sthc, Splt, and Stk. Sample locations are displayed on the topographic map in a yellow color gradient corresponding to the localities on the stratigraphic column: Stenkul Fiord, Split Lake, Axel Heiberg, Strathcona Fiord, Fosheim Peninsula, and Lake Hazen. Topographic data from GeoMapApp (Ryan et al., 2009). B) Map of sample placement at sample localities. Map on the right. Blue points show each sample, and circles in the yellow color gradient correspond to the sample localities used in Figure 3.

## 2. BACKGROUND

### 2.1. Late Paleocene and Early Eocene Climate

The Eocene Epoch (56 to 34 Ma) was marked by high atmospheric carbon dioxide concentrations, warm global temperatures, and reduced to absent polar ice. The late Paleocene (~59 to 56 Ma) to early Eocene (~56 to 48 Ma) was punctuated by short but dramatic warming events, including the Paleocene-Eocene Thermal Maximum (PETM or ETM1; ~56 Ma), Eocene Thermal Maximum 2 (ETM2; ~54 Ma), and Early Eocene Climatic Optimum (EECO; 53 to 51 Ma) (Zachos et al., 2008; Galeotti et al., 2010; Hyland & Sheldon, 2013). During early Eocene warming events, there were changes in precipitation intensity and distribution, a general pattern of wetter mid- to high-latitude climate, and high hydrologic sensitivity in response to changes in atmospheric carbon dioxide content and temperature (Zachos et al., 2001).

The PETM and ETM2 each lasted less than 200,000 years and were marked by a significant negative carbon isotope excursion (CIE) in marine and terrestrial sediment records (Eldrett et al., 2014). The PETM negative CIE was brought on by the significant release of  $^{13}\text{C}$ -depleted carbon (possibly from organic or methanogenic carbon, which discriminates strongly against  $^{13}\text{C}$ ) and caused the ocean reservoir to absorb a large amount of  $\text{CO}_2$ , shoaling the carbonate compensation depth (CCD) and causing dissolution of deep ocean carbonates (e.g. McInerney & Wing, 2011; Gutjahr et al., 2017). The extent of the CIE within bulk carbonate  $\delta^{13}\text{C}$  records show values around 2‰ before the PETM, -1‰ during the PETM, and 1‰ following the PETM. The CIE recovery phase involved processes like the burial of  $^{13}\text{C}$ -depleted carbon within peat and soil and negative feedbacks, which allowed temperatures to decrease into the late Paleocene (McInerney & Wing, 2011).

### 2.1.1. Existing Arctic Isotope and Climate Data

Studies on Arctic conditions during the late Paleocene have observed a greater than 2.5‰ negative carbon isotope excursion in marine and soil carbonate records corresponding to the PETM. Analysis of stable hydrogen and carbon isotopes in *n*-alkanes from Arctic Ocean sediments suggest the onset of the PETM brought greater moisture delivery to the Arctic, a larger (-4.5 to -6‰) carbon isotope excursion in terrestrial plants than in marine carbonates, and persistence of warming conditions from hydrologic feedbacks (Pagani et al., 2006). Late Paleocene Arctic flora leaf-size analysis yields high precipitation estimates for the western and eastern Arctic, with a mean annual precipitation (MAP) >140 cm/year in the central area of Ellesmere Island directly adjacent to Axel Heiberg Island (Greenwood et al., 2010).

A marginal marine sediment core from the Arctic Basin spanning the late Paleocene to early Eocene was evaluated with pollen and spore assemblages, palynofacies, lipid biomarker paleothermometry, and nearest living relative bioclimatic analyses to obtain terrestrial vegetation and climate information (Willard et al., 2019). This study found expansion of mesothermal forests (mean annual temperature [MAT] of 13 to 20 °C) during the PETM and ETM2, mean annual temperatures 2 to 3.5 °C greater during the PETM than the temperatures in the late Paleocene, and PETM cold-month mean temperatures  $\geq 5$  °C. This study also suggested the hyperthermal events corresponded with increased precipitation and runoff of nutrients into the ocean, with intermediate climate conditions during the late Paleocene and PETM recovery, and the dominance of swamp forests between the PETM and ETM2 (Willard et al., 2019).

Terrestrial hydrologic conditions of the middle Eocene are well studied on Axel Heiberg Island. Arctic leaf analyses indicate a MAT of 13-15 °C, cold-month mean temperature (CMMT)  $\sim 4$  °C, and MAP of >120 cm/year on Axel Heiberg Island during the middle Eocene (Greenwood

et al., 2010). Analysis of pollen and spores in lignites show differences of 1‰ ( $\delta^{13}\text{C}$ ) between terrestrial organic matter in lowland and upland environments, uniform environmental water oxygen isotope values, and unique precipitation patterns (Jahren et al., 2008). Carbon, oxygen, and hydrogen isotopic data from tree rings in the Axel Heiberg fossil forest showed increasing temperatures during the growing season, patterns of seasonal switch-over from storing to acquiring carbon during deciduous growth, and high humidity (Jahren & Sternberg, 2008). Analysis of fossil wood indicated that the middle Eocene Arctic experienced around three times greater summer precipitation than winter precipitation, and twice the present amount of atmospheric water vapor, maintaining greenhouse insulation even through dark winters (Schubert et al. 2012; Jahren & Sternberg, 2003).

### **2.1.2. Arctic Monsoonal Climate Debate**

One significant debate for this region is whether or not Arctic precipitation was monsoonal. There are multiple definitions of monsoonal climate - which often factor in circulation, summer precipitation rates, and warm month precipitation (Zhang & Wang, 2008), but in the context of paleoclimate interpretations this generally refers to a region with significant seasonal precipitation differences.

Global precipitation reconstructions for the Eocene have shown monsoonal precipitation patterns in lower and middle latitudes, but “ever-wet” (equable, non-monsoonal) conditions have been suggested for high latitude areas (Huber & Goldner, 2012). Contrasting to these global model results, intra-ring carbon isotope analysis of fossil wood within Eocene Arctic forests displayed significant seasonality of paleoprecipitation, with 3.1 times more precipitation in summer than winter (Schubert et al., 2012). These high-resolution isotopic results indicate that

Canadian Arctic ecosystems received around 76% of total annual precipitation during summer months, strongly suggesting Arctic monsoonal conditions (Schubert et al., 2012). At the other pole, Antarctic conditions during the early-middle Eocene were reconstructed by Jacques et al., (2014) using CLAMP Analysis (Climate Leaf Analysis Multivariate Program). This study indicated Antarctic summer monsoonal conditions and highlighted a gap in understanding of polar heat transfer, potentially explaining why many climate models fail to successfully reconstruct low latitudinal temperature gradients (Jacques et al., 2014).

Model weaknesses are not the only source of uncertainty in the monsoonal debate, as other bioclimatic proxy studies in the Arctic have found little to no precipitation seasonality (e.g., Eldrett et al., 2009, Elberle & Greenwood, 2012). Furthermore, recent LAA (Leaf Area Analysis), LMA (Leaf Margin Analysis), CLAMP (Climate Leaf Analysis Multivariate Program), and Bioclimatic Analysis (nearest living relative method) studies were conducted on late Paleocene to early Eocene megafloora and palynoflora in samples from three of our same localities (Strathcona Fiord, Split Lake, and Stenkul Fiord), see Figure 1. In this work, researchers found high (MAP >150 cm/year) precipitation values, but described conditions as “ever-wet” or equable, and did not observe a monsoonal climate signal (West et al., 2015).

### **2.1.3. Existing Arctic Paleontological Data**

During the Paleocene to early Eocene, most of the Canadian Arctic Archipelago was covered by deciduous vegetation, with forests in low-lying swamps. The early Eocene had widespread broadleaf taxa and very few evergreen conifers in fossil assemblages. Flora became more complex towards the middle Eocene, hosting evergreen conifers, elms, hickories, lindens, oaks, and plane trees (McIver & Basinger, 1999).

Early-middle Eocene climate and warming events resulted in unusual fauna, including alligators, boid snakes, primates, tapirs, and turtles living in high Arctic swamp forests (Estes & Hutchison, 1980; Eberle et al., 2014). Arctic macroflora analysis shows that during this time the Canadian Arctic was dominated by mixed conifer-broadleaf rainforests on land (similar to southeastern US swamp-cypress and broadleaf floodplain forests), and *Azolla* floating fern mats offshore. Arctic Ocean sea level fluctuated from tectonics, creating land bridges that facilitated dispersion of land plants and animals between the Canadian Arctic and North America, Europe, and Asia (Eberle & Greenwood, 2012).

## **2.2. Nunavut Geologic Background**

### **2.2.1. Current Setting**

Axel Heiberg and Ellesmere are two islands located in the Canadian Arctic Archipelago in the Nunavut territory of Canada (Figure 2). These islands are currently positioned from 77°N to 82°N, and paleolatitudes from 66-40 Ma were roughly 2 degrees south of their current latitudes, at 75°N to 80°N (Irving & Wynne, 1991; West, 2019; Jahren, 2007). During this time, as now, the islands experienced continuous darkness during winter and continuous light during summer, with shorter spring and fall seasons (Jahren, 2007). Most of the central and southern portion of both islands are covered by Circumpolar Arctic bioclimatic subzone C, with bioclimatic subzone B around the perimeters, and bioclimatic subzone A around the northwestern coastal areas (CAVM Team, 2003). Summer warmth indices for the zones are approximately 9-12 °C, 6-9 °C, and <6 °C, respectively (CAVM Team, 2003; Young, 1971). Dominant plant types include hemi-prostrate dwarf shrubs and prostrate dwarf shrubs (Gould, 2003).

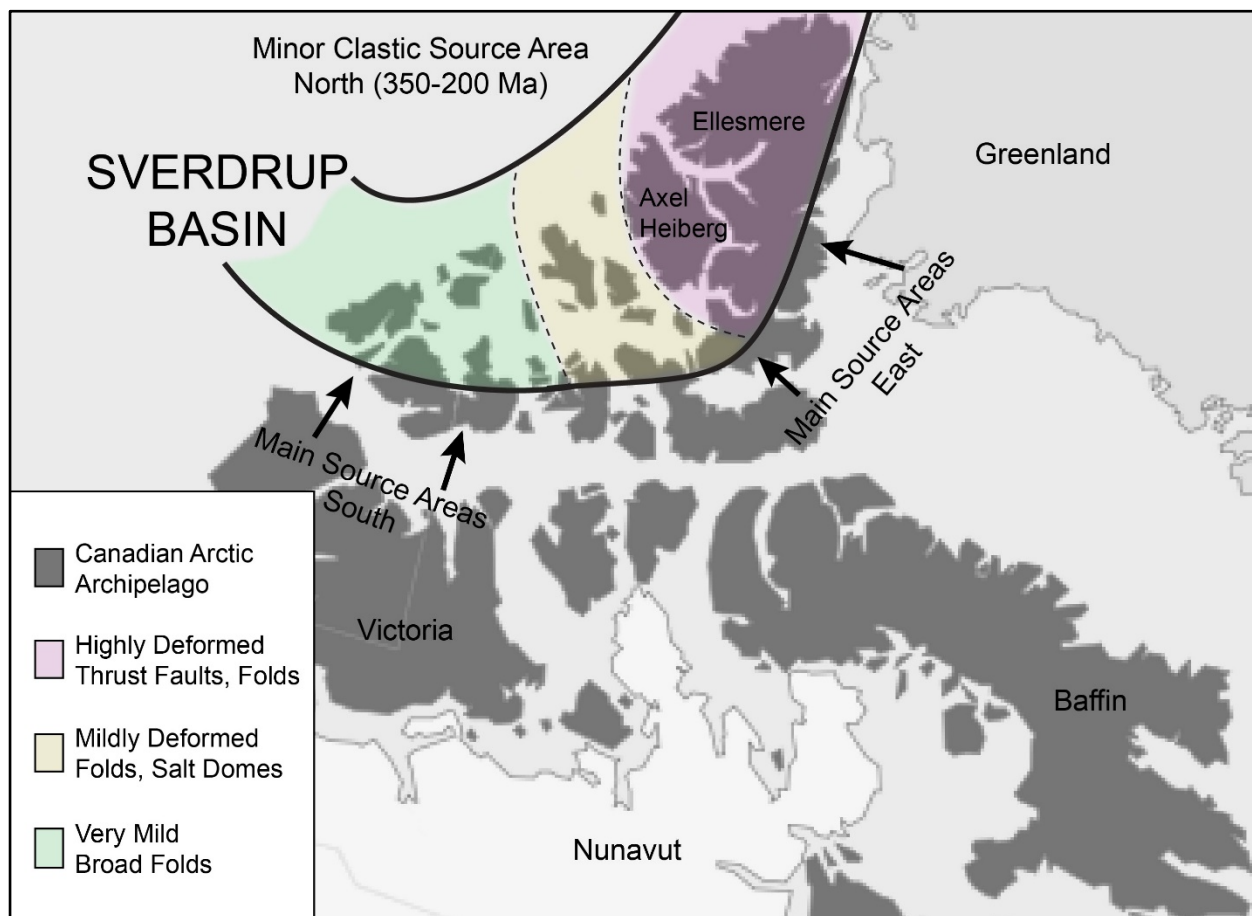


Figure 2. Placement of Sverdrup Basin over the Canadian Arctic Archipelago. Shaded islands are the Canadian Arctic Archipelago in the Nunavut territory. The black lines show approximate outline of the Sverdrup Basin. Deformation is shown by pink (highly deformed), yellow (mildly deformed), and green (very mild deformation). Clastic sediment source areas are shown by arrows and labels. Information from Embry & Beuchamp (2008).

### 2.2.2. Sverdrup Basin Geologic History

The Sverdrup Basin covers the northern islands of the Canadian Arctic Archipelago, including Axel Heiberg and most of Ellesmere Island, see Figure 2. The Sverdrup Basin spans nearly 1,000 km by 350 km, with a depocenter that holds approximately 13,000 meters of strata, beginning with Carboniferous deposits (Nunez-Betelu et al., 1994). In the Carboniferous, the Sverdrup Basin formed as a rift basin, with rifting brought on by global plate tectonic reorganization. Following this, the Sverdrup Basin experienced longer cycles of uniform subsidence and shorter cycles of differential subsidence and uplift. Carbonates were deposited

between brief faulting, folding, and volcanic events through the early Permian. Following the rifting, deltas prograded from the south and east with deposition of submarine fans into the center of the basin. From the middle Permian to Jurassic, the basin experienced periods of reduced sediment supply and accumulated mud and silt. A second stage of rifting began in the middle Jurassic, resulting in uplift and heating along the Sverdrup Rim, and a rift shoulder along the northwest basin margin (Dewing & Obermajer, 2011).

Seafloor spreading in an adjacent basin coincides with an early Cretaceous unconformity in the Sverdrup. Rates of subsidence and sediment deposition increased following formation of the unconformity, and the Isachsen Formation (fluvial sandstones) and Christopher Formation (mud, transgressive) were deposited. During the early Cretaceous, regional stress and loading, low amplitude folding, and thinning of sections of the Christopher Formation occurred. In the middle Cretaceous, dikes and sills intruded most of the northeast Sverdrup basin, initiating from Axel Heiberg and intruding into deeper stratigraphic levels further away. The late Cretaceous saw slow basin subsidence and accumulation of the Kanguk Formation (organic-rich mud, volcanic ash) (Dewing & Obermajer, 2011).

Phase 1 of Eurekan Orogeny began in the early Paleocene following changes in seafloor spreading in the Labrador Sea and Baffin Bay, and resulted in formation of an approximately 30 km rift zone between western Ellesmere Island and eastern Axel Heiberg Island (Gion et al., 2017). Once northern Greenland converged with Ellesmere Island, rapid subsidence occurred in the eastern part of the Sverdrup basin, creating accommodation space. From the Paleocene to middle Eocene, clastic sediments of the Eureka Sound Group were deposited into the northeastern Sverdrup basin (Dewing & Obermajer, 2011).

The basin experienced strike-slip movement and compressive deformation during the early and middle Eocene, culminating in Phase 2 of the Eurekan Orogeny, which resulted in fragmentation, inversion, and uplift of the basin (Stephenson & Ricketts, 1990; Gion et al., 2017). Thrust faulting and folding occurred in the northern portion of the basin, with high-amplitude folds in the northeast and low-amplitude folds in the west (Dewing & Obermajer, 2011). Eurekan Orogeny compressive deformation was accompanied by uplift and erosion, which was then followed by sedimentation of new units above unconformities (Von Gosen et al., 2019).

The end of Phase 2 of the Eurekan Orogeny is defined in different ways, including the end of deformation before the middle Eocene (Von Gosen et al., 2019), the ~33 Ma end of seafloor spreading in Baffin Bay and the Labrador Sea, and the early Miocene-aged conglomerates that unconformably overlie Eocene deposits (Gion et al., 2017). The Axel Heiberg conglomerates are alluvial fan deposits that coarsen to the west and were previously identified as early Miocene (Trettin & Balkwill, 1979), but when compared against other stratigraphic unit descriptions appear to match middle Eocene Buchanan Lake conglomerates, corroborating Von Gosen's approximation of an end to the Eurekan Orogeny before or during the middle Eocene.

### **2.2.3. Eureka Sound Group Stratigraphy**

The clastic sediments deposited into the Sverdrup Basin during the Paleocene and Eocene make up the Eureka Sound Group. The Eureka Sound Group strata, which experienced deformation as a result of the burial and uplift phases of the Eurekan Orogeny, have inconsistent naming conventions and recently updated stratigraphy.

Initial work conducted on the Eureka Sound classified it as a formation and divided it into members I-IV for western and central Ellesmere Island (West et al., 1981). Miall (1986) redefined it as the Eureka Sound Group, composed of nine formations extending across Ellesmere to other southward islands in the Canadian Arctic Archipelago. Miall divided the Eureka Sound Group into the Mount Bell, Vesle Fiord, Mount Lawson, Mount Moore, Margaret, Mokka Fiord, Cape Back, Cape Lawrence, and Boulder Hills Formations. In this work, the Margaret Formation was correlated to West's member IV (Miall, 1986). For the same general areas in the eastern Canadian Arctic Archipelago, Ricketts divided the Eureka Sound Group into four formations and correlated them to West's III and IV members. Ricketts named his formations the Expedition, Strand Bay, Iceberg Bay, and Buchanan Lake Formations (Ricketts, 1986). Reidiger & Bustin (1987) studied a shorter section of the Eureka Sound Group in southern Ellesmere Island, and identified two Paleocene and Paleocene-Eocene aged transgressive-regressive cycles in the Eureka Sound Group and correlated their units (including a Stenkul Fiord non-marine Eocene unit containing vertebrate fossils) with Miall's Margaret Formation and part of West's member IV (Reidiger & Bustin, 1987; Eberle & Eberth, 2014). Due to the different naming conventions for the late Paleocene to early Eocene aged formations composing the Eureka Sound Group (e.g., Miall, 1986; Ricketts, 1986), the present study uses the updated naming convention published in West (2019) which combines the nomenclature conventions and provides a comprehensive overview of the naming schemes and refined stratigraphy.

The analyzed samples are within the late Paleocene to early Eocene depositional period of the Mount Lawson, Mount Moore, Margaret, Mokka, and Buchanan Lake Formations. Outcrops of these formations are present in different locations across Axel Heiberg and Ellesmere Islands and have been assigned approximate ages through lithostratigraphy,

biostratigraphy, magnetostratigraphy, and U-Pb zircon dating. Because units are diachronous based on the location and degree of tectonic denudation experienced, a more precise age control beyond a range of late Paleocene to early Eocene cannot be assigned. In the stratigraphic column (see Figure 3), samples were placed at the 56 Ma boundary between the late Paleocene and the early Eocene, although there is no strong evidence that this is the exact placement and samples may have different ages within the 59 to 48 Ma timeframe.

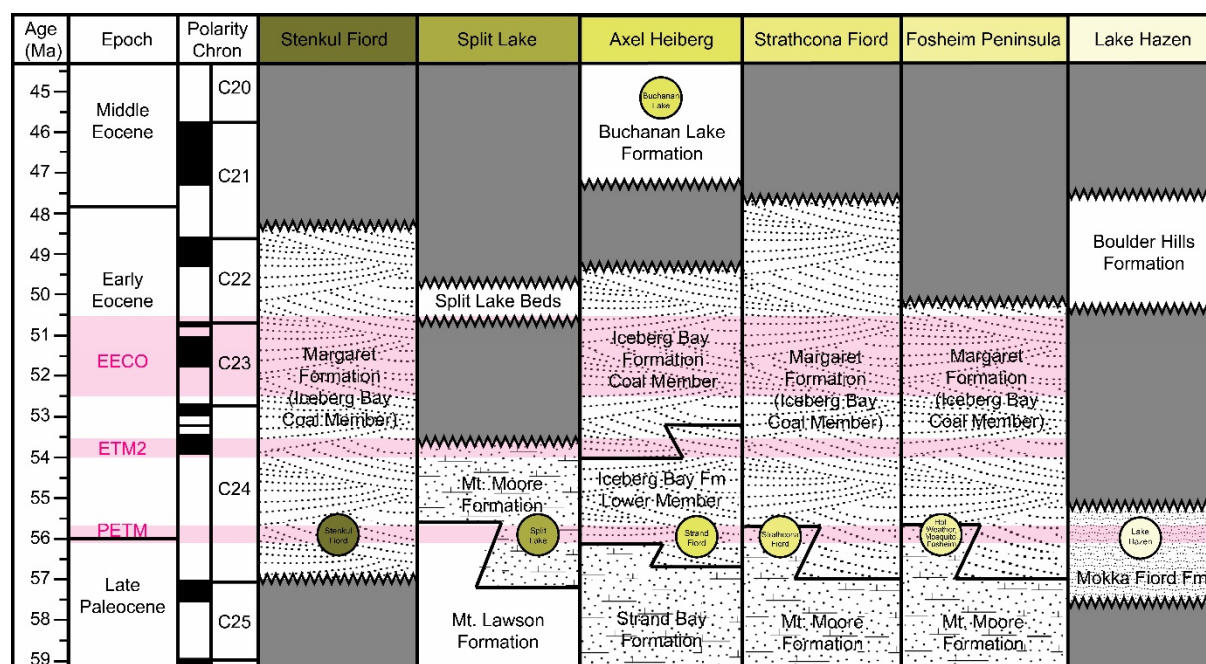


Figure 3. Simplified stratigraphic column with sample placement. Stratigraphic column displaying relevant formations (Mt. Lawson, Mt. Moore, Margaret, Mokka Fiord, and Buchanan Lake Formations) within the Eureka Sound Group and the approximate sample ages. Yellow color gradient corresponds to map localities. Base column created by West (2019) and adapted to the samples. Pink shaded regions indicate major climatic events.

The **Mount Lawson Formation**, referred to as the Strand Bay Formation on Axel Heiberg, is mostly composed of dark brown and grey brown sandstones and mudstones from high-sinuosity fluvial deposits and low energy distal delta front facies (Miall, 1986; Ricketts, 1986). Zircons from this formation at the Split Lake location were analyzed via U-Pb SHRIMP, and returned dates of  $53.9 \pm 3$  Ma (Reinhardt et al., 2013), and paleomagnetic correlations

assigned the formation to Chrons 25 and 26 (Tauxe & Clark, 1987). Based on the location (present at Split Lake and Strathcona Fiord exposures), the Mount Lawson Formation spans the late Paleocene to early Eocene, and lies conformably below the younger Mount Moore Formation (Miall, 1986).

The **Mount Moore Formation** is mostly composed of cream and tan shallow marine sandstone interlayered with discontinuous siderite-cemented sandstone (Miall, 1986). This formation contains shark, teleost fish, and bivalve fossils, with foraminifera and palynomorphs correlated to paleomagnetic Chrons 24r to 25n (West et al., 1977; Harrison et al., 1999). Mount Moore samples from the Split Lake and Strathcona Fiord locations are from calcareous muddy tidal flat and delta plain facies, while Fosheim Peninsula samples are from delta plain facies that accumulated during the late Paleocene to early Eocene depositional timeframe, see Figure 4 B and C (Ricketts & Stephenson, 1994).

The lower **Margaret Formation**, referred to as the Coal Member of the Iceberg Bay Formation on Axel Heiberg, is mostly composed of cross-bedded sandstone, siltstone, mudstone, and coals, stacked in coarsening upward cycles including delta front, delta plain, distributary channel, and swamp facies (Miall, 1986; Ricketts, 1986). Zircons from ash layers in the lower Margaret Formation at the Stenkul Fiord location were analyzed via U-Pb SHRIMP and produced dates of  $53.7 \pm 0.6$  Ma (Reinhardt et al., 2013; Von Gosen et al., 2019), and biostratigraphy approximated the formation spanning the late Paleocene to early Eocene (West et al., 1981; Eberle & Greenwood, 2012; Von Gosen et al., 2019). Margaret Formation samples from the Stenkul Fiord location are predominately calcareous muddy tidal flat and delta plain facies deposited during the late Paleocene to early Eocene (Figure 4B, C) (Ricketts & Stephenson, 1994).

The **Mokka Fiord Formation**, which has exposures across Ellesmere and Axel Heiberg Islands, is composed of cross-bedded sandstone with sideritic lenses, very fine-grained sandstones with ripples, silty mudstone, carbonaceous mudstone, and thin coal layers, arranged in fining upward cycles deposited in fluvial and flood plain environments (Miall, 1986; Ricketts, 1986). Mokka Fiord deposits at the Lake Hazen location are primarily from floodplain and alluvial fan facies during the late Paleocene to early Eocene, and the formation has an equivalent age to the Mount Moore and Margaret Formations (Miall, 1991). Following deposition, tectonic denudation during the middle Eocene eroded the late Paleozoic units into a syntectonic basin at the Lake Hazen fault, and buried the Mokka Fiord deposits at Lake Hazen (Figure 4C, D) (Ricketts & Stephenson, 1994).

The **Buchanan Lake Formation** on Axel Heiberg is the youngest unit of the Eureka Sound Group and is composed of diabase pebble conglomerates and lithic sandstones interpreted as alluvial fan facies. These deposits formed following uplift and thrusting, as an eastward directed paleocurrent brought in Mesozoic rock detritus from the west and deposited it into a syntectonic basin during the middle Eocene (Figure 4D) (Ricketts & Stephenson, 1994). Palynomorph assemblages within the Buchanan Lake Formation suggest that the type locality deposits are around 45 Ma (Ricketts & McIntyre, 1986; West, 2019).

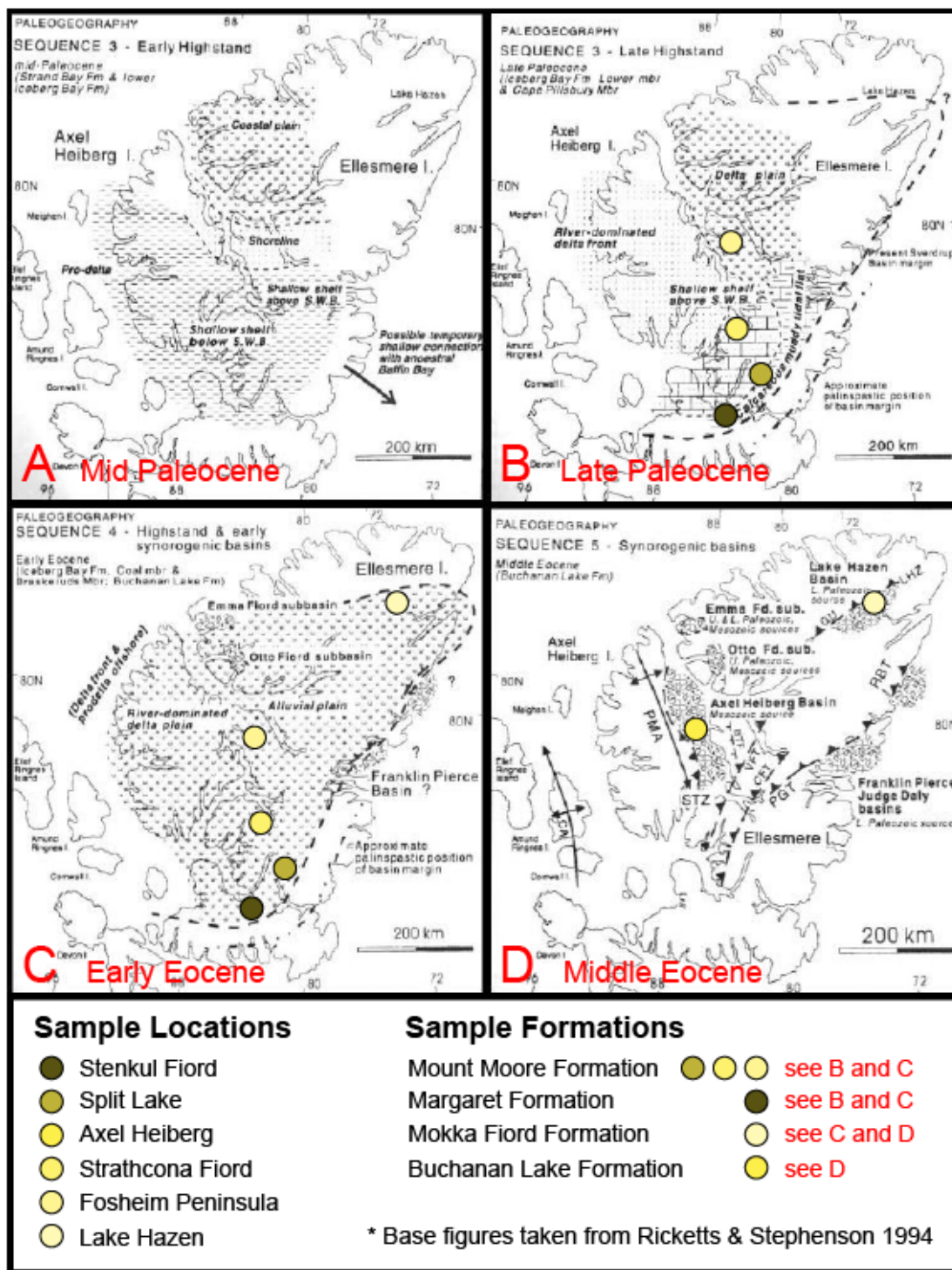


Figure 4. Sverdrup Basin sequence stratigraphy and environmental reconstructions. Displayed through the mid-Paleocene, late Paleocene, early Eocene, and middle Eocene. Base illustrations taken directly from Ricketts & Stephenson (1994) and superimposed with some sample locations highlighted during the times they were deposited or altered. The yellow color gradient corresponds to the map (Figure 1) and stratigraphic column (Figure 3).

#### **2.2.4. Eureka Sound Group Samples**

Carbonate rock samples from formations within the Eureka Sound Group were collected from the following general localities: Stenkul Fiord, Split Lake, Axel Heiberg, Strathcona Fiord, Fosheim Peninsula, and Lake Hazen (color-coded and labeled in Figures 1 and 3). From left to right on the stratigraphic column (Figure 3), Stenkul Fiord is located in southern Ellesmere Island, and samples US435, US436, and US438 are late Paleocene to early Eocene. Split Lake is in central to southern Ellesmere Island, and sample US444 is late Paleocene to early Eocene. Axel Heiberg includes the middle Eocene Buchanan Lake sample US119 and late Paleocene to early Eocene Strand Fiord sample US176. Strathcona Fiord is in central to southern Ellesmere Island, and sample US422 is late Paleocene to early Eocene. Fosheim Peninsula is located in central Ellesmere Island and includes the late Paleocene to early Eocene samples at Mosquito Creek (US196), Hot Weather Creek (US107, US108), and Fosheim Anticline (US111, US191, US251). Lake Hazen is located in northern Ellesmere Island, and sample US261 is late Paleocene to early Eocene.

### **2.3. Stable and Clumped Isotope Geochemistry**

#### **2.3.1. Palustrine Carbonate Formation**

Palustrine carbonates form in locations with carbonate-rich rivers and groundwater and are associated with lake margin, fluvial, floodplain, and swamp facies. The formation of palustrine carbonates is favored in highly vegetated non-tidal wetlands or low salinity tidal wetlands, and deposits are a combination of inorganic carbonate (greater deposition at warmer temperatures) and biogenic carbonate (algae and microbes). Palustrine carbonates form readily in sub-humid conditions, preserve more organic material during humid conditions, and only require

a season-long period of sub-aerial exposure to precipitate out layers of lime mud. Palustrine carbonate deposition can occur in all types of lacustrine basins (balanced-fill, underfilled, and overfilled), but are most common in overfilled basins, highstand balanced-fill basins, and highstand underfilled basins (Alonso-Zarza, 2003).

A key feature of palustrine carbonates is that they display characteristics of their primary deposition as well as secondary transformations from exposure, pedogenesis, and water saturation (Freytet, 1984). Some evidence of diagenesis includes mineral stabilization and aggrading neomorphism causing palustrine samples to be well indurated, and the presence of acicular and coarse spar cementation from vadose and phreatic meteoric diagenesis, respectively (Wright et al., 1997). In thin-section, these terrestrial carbonates often have a primary micrite mud matrix (0.3-1.3  $\mu\text{m}$  calcite crystals) with coarse patches of micro-spar and spar throughout. “More developed” palustrine limestones typically have evidence of biogenic alteration (e.g., due to roots or vegetation structures), while “less developed” samples tend to be associated with physical or chemical alteration (Alonso-Zarza, 2003).

### **2.3.2. Stable Isotopes in Palustrine Carbonates**

Overall, palustrine carbonates tend to have more negative  $\delta^{13}\text{C}$  and  $\delta^{18}\text{O}$  values than unaltered lake counterparts, and more positive  $\delta^{13}\text{C}$  and  $\delta^{18}\text{O}$  values than nearby pedogenic carbonates (e.g., Platt, 1989; Alonso-Zarza, 2003). A range of  $-2$  to  $-11\text{‰}$  ( $\delta^{13}\text{C}$ ) and  $-4$  to  $-10\text{‰}$  ( $\delta^{18}\text{O}$ ) is typical for many palustrine carbonates, with late diagenetic calcite samples having significantly more negative  $\delta^{18}\text{O}$  values closer to  $-15$  to  $-17\text{‰}$ , reflecting heated meteoric waters (Tandon & Andrews, 2001).

### 2.3.2.a. Primary Features

Palustrine carbonate isotope signatures are typically similar to that of a lacustrine carbonate. The original lake source water composition is controlled by rainwater, evaporation, and river and stream surface water flows (Tandon & Andrews, 2001; Bernasconi & McKenzie, 2007). The primary carbonate  $\delta^{18}\text{O}$  value reflects the biogenic and temperature-dependent fractionation occurring between the calcite and original lake source water (Kim & O'Neil, 1997; Cerling & Quade 1993; Alonso-Zarza, 2003). Biogenic fractionation can significantly impact primary oxygen isotope values, with higher primary productivity levels increasing lake pH and resulting in negative shifts in  $\delta^{18}\text{O}$  (Bernasconi & McKenzie, 2007). Generally, the oxygen isotope record in lacustrine sediments more strongly reflects the  $\delta^{18}\text{O}$  of the lake water rather than water temperature, and assuming temperatures are consistent between similar lake environments, results in estimates with only minor errors (Bernasconi & McKenzie, 2007).

Rainfall  $\delta^{18}\text{O}$  depends on the air temperature, moisture source, and seasonal distribution of precipitation (Rozanski et al., 1993; Kohn & Welker, 2005). Greater average air temperature increases the  $\delta^{18}\text{O}$  of the rainfall and therefore increases the lake  $\delta^{18}\text{O}$  when deposited into the source water (Kohn & Welker, 2005). Evaluating the changes in  $\delta^{18}\text{O}$  of lake carbonates through time can provide an indirect record of local rainfall input and help filter out uncertainty about lake dynamics, such as mixing variations or smaller seasonal changes (Bernasconi & McKenzie, 2007).

The  $\delta^{13}\text{C}$  of palustrine carbonates describes initial environmental conditions, in the form of decomposing land vegetation in sediments and organic productivity within the lake. Carbon isotope ( $\delta^{13}\text{C}$ ) compositions of lacustrine carbonates approximate inorganic carbon composition in lake source water, which reflects the input of dissolved inorganic carbon through surface

water flows and groundwater sources, and CO<sub>2</sub> composition during atmospheric exchange (Hollander & McKenzie, 1991; Leng & Marshall, 2004; Nelson et al., 2005). The fractionation of carbon isotopes between dissolved inorganic carbon and calcite are not significantly influenced by temperature, but are sensitive to lake productivity (Bernasconi & McKenzie, 2007).

In highly vegetated lake margins, isotopically negative  $\delta^{13}\text{C}$  values suggest high carbon input into the soil and groundwater. Increased decay of C<sub>3</sub> organic matter in surrounding sediments on lake margins can cause higher soil-zone carbon, due to the high concentration of C<sub>3</sub> plant debris, and thus more negative  $\delta^{13}\text{C}$  values (Tandon & Andrews, 2001). Changes in relative amounts of C<sub>3</sub> and C<sub>4</sub> vegetation can be excluded as a variable that would influence the  $\delta^{13}\text{C}$  values in this case, because C<sub>4</sub> plants (which are characterized by more positive  $\delta^{13}\text{C}$  values) evolved after the middle Eocene and after the deposition of the samples (Schaeztl & Anderson, 2005; Urban et al. 2010). In the absence of significant land plant influence, the primary palustrine carbon isotope values are influenced by fractionation by microbes and algae within lakes (Andrews et al., 1997). High microbial and algal lake productivity reduces  $^{12}\text{C}$  in the source water, causing precipitated carbonates to display more negative  $\delta^{13}\text{C}$  relative to less productive lake carbonates (Alonso-Zarza, 2003). In previous studies measuring carbon isotope values of palustrine carbonates within similar facies,  $\delta^{13}\text{C}$  varied significantly between sites due to variations in primary biological productivity (Alonso-Zarza et al, 2006).

### **2.3.2.b. Secondary Features**

Beyond the conditions of first-generation micrite formation, palustrine stable isotopes record conditions of subsequent secondary alteration. Secondary alteration can occur at Earth's

surface conditions (for pedogenic and some types of diagenetic alteration), and deeper subsurface conditions. Variations in the stable isotope values for palustrine carbonates from lake settings may reflect (1) degree of exposure and pedogenic alteration, (2) surface diagenesis by meteoric waters, and (3) burial diagenesis by heated burial fluids (Tandon & Andrews, 2001).

#### (1) Exposure and pedogenic alteration

Palustrine carbonates are often modified by processes related to exposure and pedogenic alteration (Tandon & Andrews, 2001). Stable isotope values can change based on the specific processes and levels of pedogenic modification experienced. Pedogenic modifications (desiccation, modifications associated with roots and soil organisms, and the remobilization of carbonate and iron) occur early to the micrite deposits and leave behind distinguishing features (Alonso-Zarza, 2003). Desiccation features include nodular, brecciated, and mottled limestones with cracks (Freytet, 1973). Pedogenic alteration from roots and soil organisms form mottled limestones with roots and vegetation structures, vertical root cavities, pseudo-microkarst, and peloidal and intraclastic limestones (Freytet & Plaziat, 1982; Alonso-Zarza et al., 1992a). Key features of remobilization of iron include mottling, iron crusts, and concretions (Freytet, 1973)

Variations of carbonate fabrics reflect subaerial exposure, brecciation, pedoturbation, and pedogenesis of samples (Marty & Meyer, 2006). Palustrine carbonates can generally be approximated on a scale between less to more pedogenic modification, which helps to clarify the level of physio-chemical and biogenic processes that could potentially impact the isotopic composition of the micrite. “Less developed” palustrine limestones are impacted by physio-chemical processes (desiccation and iron mobilization features), while more-developed samples are altered by biogenic processes. The isotopic signature of more developed palustrine

limestones is complicated by roots moving water through the micrite during changes in lake levels and biochemically precipitating new carbonate. Palustrine carbonates that have undergone greater pedogenesis frequently have more negative  $\delta^{13}\text{C}$  and  $\delta^{18}\text{O}$  values relative to less altered counterparts and lacustrine carbonates (Alonso-Zarza, 2003). A lack of calcrete characteristics and physical shrinkage features suggest that samples experienced limited subaerial exposure and developed in environments with a stable ground water level (Tandon & Andrews 2001).

Limestones with effective fossil preservation and lack of crucial pedogenic alteration features indicate minimal pedogenesis, and minimal modification of primary isotopic values via these processes (Marty & Meyer, 2006).

## (2) Surface diagenesis by meteoric waters

Palustrine isotopic values are specific to whether the carbonate formed in a lake or wetland setting, which is differentiated by the relative contribution of surface water versus groundwater. For lakes, the primary input is from river and stream surface waters (secondary: groundwater), while for wetlands the primary input is from the groundwater table (secondary: surface water sheet flows) (Dunagan & Turner, 2004). The amount of change to the primary  $\delta^{18}\text{O}$  signal varies based on its original source water and subsequent diagenetic alteration fluid (Tandon & Andrews 2001).

Surface diagenesis refers to groundwater flowing through the soil profile and modifying the first generation carbonates, with processes including meteoric cementation, mineralogical stabilization, karstification, dolomitization, and siderite formation (Alonso-Zarza, 2003; Ludvigson et al., 2013). Isotopic inheritance for the secondary calcite formed in these processes depends on whether alteration occurs from the same water of its original depositional

environment. For samples formed in most wetland settings, the alteration does not significantly change  $\delta^{18}\text{O}$  or  $\delta^{13}\text{C}$ , because the groundwater source and soil carbon input are the same as its original depositional conditions. However, in some cases samples from lake settings that undergo alteration by meteoric-fed groundwater at near-surface temperatures will result in more negative  $\delta^{18}\text{O}$  and  $\delta^{13}\text{C}$ , particularly in settings with high biological activity (Tandon & Andrews, 2001).

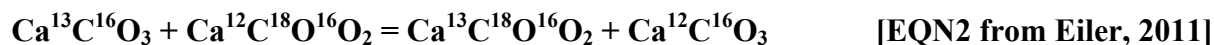
### (3) Burial diagenesis by heated burial fluid

Unlike the previous two processes, burial alteration refers to diagenetic alteration occurring in the subsurface, as first-generation carbonate rocks are buried over longer (million year) timescales. As calcium carbonate deposits are compressed and lithified beneath younger overburden, the increased temperatures and pressure solution can dissolve and reprecipitate carbonate minerals. Deeper burial isolates rock units from surface waters, and instead, hydrothermal and burial fluids move through pore space within the subsurface (Flügel, 2010).

Burial diagenesis occurs when heated burial fluid modifies first-generation carbonates through mineralogical recrystallization, or crystallizes new coarse calcite spar in pore spaces (Alonzo-Zarza, 2003). Other diagenetic processes that occur in the deep burial zone include physical and chemical compaction, minor solution porosity, and burial dolomitization (Flügel, 2010). Elevated temperatures associated with burial diagenesis may affect the clumped isotope ( $\Delta_{47}$ ) and  $\delta^{18}\text{O}$  composition of samples. In general, the diagenetic alteration will lower sample  $\delta^{18}\text{O}$  due to the increases in temperatures due to burial (Tandon & Andrews 2001).

### 2.3.3. Carbonate Clumped Isotopes

Carbonate clumped isotope thermometry is based on preferential bonding of heavier isotopes of carbon ( $^{13}\text{C}$ ) and oxygen ( $^{18}\text{O}$ ) together within minerals (Eiler, 2007). The clumped isotope thermometer uses the homogenous isotope exchange reaction:



This reaction involves clumping of  $^{13}\text{C}$  and  $^{18}\text{O}$  together to produce ion group:  $^{13}\text{C}^{18}\text{O}^{16}\text{O}_2^{-2}$ . The homogeneous isotope exchange reaction involves a temperature-dependent equilibrium constant that behaves closer to a heterogeneous isotope exchange reaction at high temperatures (Eiler, 2011). The heavier isotopes approach a stochastic abundance at 1000 °C, while at cooler temperatures heavier isotopes preferentially clump together (Eiler, 2007). The  $\Delta_{47}$  value of the resultant  $\text{CO}_2$  from acid-digested carbonate samples is the ratio of a sample's heavier isotope bond enrichment relative to its expected probability (Peters et al., 2013). Overall, clumped isotope thermometry involves measuring the amount of  $^{13}\text{C}$  and  $^{18}\text{O}$  bonds within the same carbonate ion group as a proxy method to obtain carbonate mineral growth temperatures (Eiler, 2011).

Clumped isotope ( $\Delta_{47}$ )-derived temperatures provide a record of environmental and atmospheric temperature that is independent of source water and evaporative effects (Ghosh et al., 2006). The  $\Delta_{47}$  of a sample is only affected by temperature, and can be applied to a  $\delta^{18}\text{O}$  record to correct for the temperature effects and isolate hydrologic changes (Kim & O'Neil, 1997). Beyond paleoclimate applications, clumped isotopes are used to reconstruct higher temperature processes including burial diagenesis, dolomitization, and hydrothermal fluid flow (e.g., Ferry et al., 2011; Huntington et al., 2011; Bristow et al., 2011).

### **2.3.3.a. Clumped Isotope Complications**

Clumped isotope values ( $\Delta_{47}$ ) can be affected by thermal reordering and recrystallization.  $\Delta_{47}$  is more sensitive to burial diagenesis than stable carbon and oxygen isotope values (Winkelstern & Lohmann, 2016). The reheating of samples to greater than 100 °C during burial may result in the reordering of C-O bonds, changing the  $\Delta_{47}$  without affecting stable isotope values or mineral texture (Passey & Henkes, 2012; Henkes et al., 2014). Clumped isotope compositions of micrite samples that maintain their fine-grain carbonate texture can also be altered through fluid-mediated diagenesis and recrystallization (e.g., Quade et al., 2013). The lack of a relationship between carbonate crystal structure and degree of resetting make it difficult to constrain the impact of diagenesis on  $\Delta_{47}$  (e.g., Eiler, 2011; Passey & Henkes, 2012; Henkes et al., 2014; Huntington & Lechler, 2015). Differences in resetting conditions for  $\Delta_{47}$ ,  $\delta^{18}\text{O}$ , and  $\delta^{13}\text{C}$  primary carbonate are not well constrained and there is limited information related to geothermal heat gradients (Huntington et al., 2011).

Overall, thermal reordering and recrystallization are complications that can cause altered carbonate samples to no longer record original surface temperatures. Instead, reordering and recrystallization can serve as methods to obtain subsurface burial temperatures.

### **2.3.3.b. Reordering for Burial History**

Solid-state reordering, which occurs at temperatures greater than ~100 °C, resets clumped isotope bonds through the diffusion of C and O through the mineral lattice (Henkes et al., 2014; Winkelstern & Lohmann, 2016). Although bond reordering affects the primary paleoclimate values, the information can still be used to reconstruct shallow crustal temperatures and cooling rates, by approximating solid-state reordering of C-O bonds in calcite due to its predictable

pattern of initial heating and alteration followed by a first-order rate law for subsequent reordering (Passey & Henkes, 2012). Previous work on the Navajo Sandstone used clumped isotope temperatures that were elevated due to solid-state reordering to reconstruct formation burial history (Parrish et al., 2018). This study used the characteristic clumped isotope reordering behavior to calculate clumped isotope temperature offsets and reconstruct burial temperatures (Parrish et al., 2018; Stolper & Eiler, 2015; Passey & Henkes, 2012). The predictable clumped isotope reordering behavior makes it possible to work backward and reconstruct sample burial depths across a basin based on their degree of post-depositional heating.

### **2.3.3.c. Secondary Carbonate $\Delta_{47}$ for Diagenetic History**

Huntington et al. (2011) proposed the use of clumped isotope thermometry as an alternative method to reconstruct the diagenetic history of shallowly buried rocks. Unlike reordering, which occurs in original carbonate minerals, this diagenetic burial history method is used explicitly on new mineral growth, carbonate or otherwise, within the structure of a previous deposit. Huntington et al. (2011) demonstrated that clumped isotope temperatures in early Eocene sediments could be used to estimate the temperature of diagenetic crystal growth and recrystallization below 250 °C. Obtaining recrystallized  $\Delta_{47}$  temperatures that are independent of source water composition permits one to approximate the  $\delta^{18}\text{O}$  of diagenetic fluids (Huntington et al., 2011).  $\delta^{18}\text{O}$  of water in equilibrium with secondary calcite can be calculated using the calcite-water isotope fractionation relationship:

$$\delta^{18}\text{O}_{\text{calcite}} \approx \delta^{18}\text{O}_{\text{water}} + 18.03 * (10^3 / T) + 32.42 \quad \text{[EQN from Kim \& O'Neil, 1997]}$$

Huntington et al. (2011) proposed using clumped isotopes to complement temperature and time-specific vitrinite reflectance data; and suggested that future studies evaluate smaller-sized and

texturally homogenous samples (<4 mg, that do not combine multiple generations of carbonate) to obtain more explicit diagenetic information (Huntington et al., 2011).

### 3. METHODOLOGY

#### 3.1. Physical Collection

Samples were collected from surface quarries by J. Basinger and D. Greenwood during multiple field seasons from 1990-2000, and all carbonates were associated with described fossil leaf assemblages which were used to assign stratigraphic positions within the Eureka Sound Group (ESG). Samples were returned to the University of Saskatchewan and cleaned and cataloged for collections purposes within the University of Saskatchewan's Paleobotanical Collection (USPC). A suite of 14 palustrine carbonate rocks was later selected from the collection by C. West and E. Hyland based on the presence of primary carbonate textures, and on both temporal and geographic distribution within the ESG.

These specific samples were collected from seven locations on Ellesmere Island (Lake Hazen, Mosquito Creek, Hot Weather Creek, Fosheim Anticline, Strathcona Fiord, Split Lake, and Stenkul Fiord) and two sites on Axel Heiberg Island (Buchanan Lake and Strand Fiord), (Figure 1). Palustrine carbonate samples were extracted from the collected bulk samples within the Eureka Sound Group in the Mount Moore Formation (US444 at Split Lake; US422 at Strathcona Fiord; US196 at Mosquito Creek; US107 and US108 at Hot Weather Creek; and US251, US111, and US191 at Fosheim Anticline), Iceberg Bay Formation Lower Member (US176 at Strand Fiord), Margaret Formation (US435, US436, US438 at Stenkul Fd), Mokka Fiord Formation (US261 at Lake Hazen), and Buchanan Lake Formation (US119 at Buchanan Lake) (Figure 3).

### 3.2. Sample Evaluation

The preparation of hand samples for analysis began with the cutting of the carbonate rocks with a rock saw to produce standard billets, which were sent to Wagner Petrographic for thin section preparation. Thin sections were examined under plain and polarized light on a petrographic microscope to evaluate carbonate fabric and estimate ratios of spar and micrite. Fabric categories included Micritic (Mic = green), Micritic to Microspar (Mic/MSp = yellow), Microspar (MSp = orange), and Sparry (Spar = red), Table 1.

To more precisely classify samples into textural categories, thin sections were quantified by a scaled percentage of spar coverage. A random walk of 60 spar crystals within each slide was used to approximate an average spar length and width. Spar dimensions were applied into an ellipse formula to calculate average spar size, which was multiplied by a general approximation of percent spar coverage for each slide. That product was then divided by a baseline of maximum crystallinity ( $3141.6 \mu\text{m}^2$ , the largest average spar size at 100% coverage on the slide) to produce a scaled percentage of spar coverage. Samples were classified into Micritic, Micritic to Microspar, Microspar, and Sparry based on the spar coverage order of magnitude (0.000X, 0.00X, 0.0X, 0.X) respectively.

Figure 5 shows microscope images of sample thin sections photographed under plain light and Table 1 shows the average spar size (Avg LxW, length and width units are  $\mu\text{m}$ ), spar-to-micrite ratio (Spar% to Mic%), scaled percentage of spar coverage (Vis Alt Coeff), and fabric category (Fabric). Within each rock, areas containing higher micritic content were targeted for sampling, as they likely experienced less recrystallization or secondary calcite formation and more closely reflected isotopic values of first-generation palustrine carbonate deposition (Driese & Mora, 1993). Microspar and Sparry samples had consistent spar distribution throughout the

entire sample, and therefore the classification into fabric categories allowed us to evaluate the isotopic composition of the spar separately. Figure 6 shows the sample fabrics at each location.

Table 1. Table of alteration approximations and sample fabrics

Sample	Age	Location	Formation	Avg LxW	Spar%	Mic%	Vis Alt Coeff	Fabric
US422	LP - EE	Strathcona	Mt Moore	40x40	0.7	0.3	0.28	Spar
US444	LP - EE	Split	Mt Moore	80x50	0.5	0.5	0.5	Spar
US436	LP - EE	Stenkul	Margaret	40x60	0.9	0.1	0.54	Spar
US176	LP - EE	Strand	Iceberg	80x50	0.8	0.2	0.8	Spar
US111	LP - EE	Fosh Ant W	Mt Moore	10x10	0.5	0.5	0.0125	MSp
US251	LP - EE	Fosh Ant E	Mt Moore	10x8	0.7	0.3	0.014	MSp
US108	LP - EE	Hot Weather	Mt Moore	10x10	0.7	0.3	0.018	MSp
US107	LP - EE	Hot Weather	Mt Moore	10x20	0.6	0.4	0.03	MSp
US196	LP - EE	Mosquito	Mt Moore	20x20	0.5	0.5	0.05	MSp
US435	LP - EE	Stenkul	Margaret	20x20	0.6	0.4	0.06	MSp
US119	MID E	Buchanan	Buchanan	10x6	0.3	0.7	0.0045	Mic/MSp
US438	LP - EE	Stenkul	Margaret	8x6	0.4	0.6	0.0048	Mic/MSp
US261	LP - EE	Lake Hazen	Mokka	8x4	0.1	0.9	0.0008	Mic
US191	LP - EE	Fosh Ant W	Mt Moore	10x6	0.05	0.95	0.0008	Mic

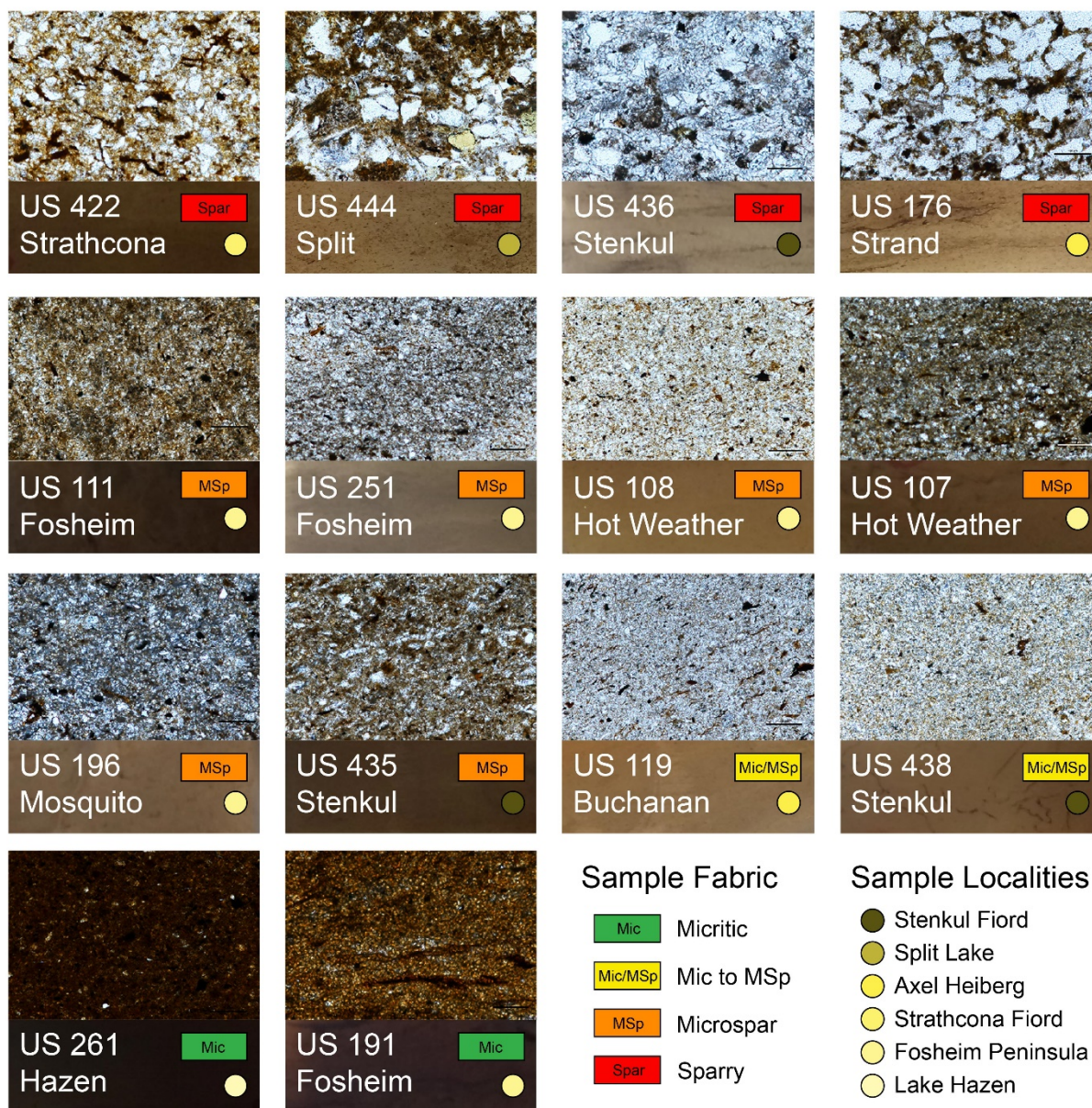


Figure 5. Plain light images of thin sections. Microscope image size is 700  $\mu\text{m}$  by 400  $\mu\text{m}$ , and images are of a random location in the middle of each slide with no specific features highlighted. Pictures beneath each microscope image is a zoomed out thin section photograph, approximately 22 mm by 8 mm. Sample localities are marked by a dot in the yellow color gradient corresponding to Figures 1 and 3, and sample fabric is labeled by a green, yellow, orange, or red box.

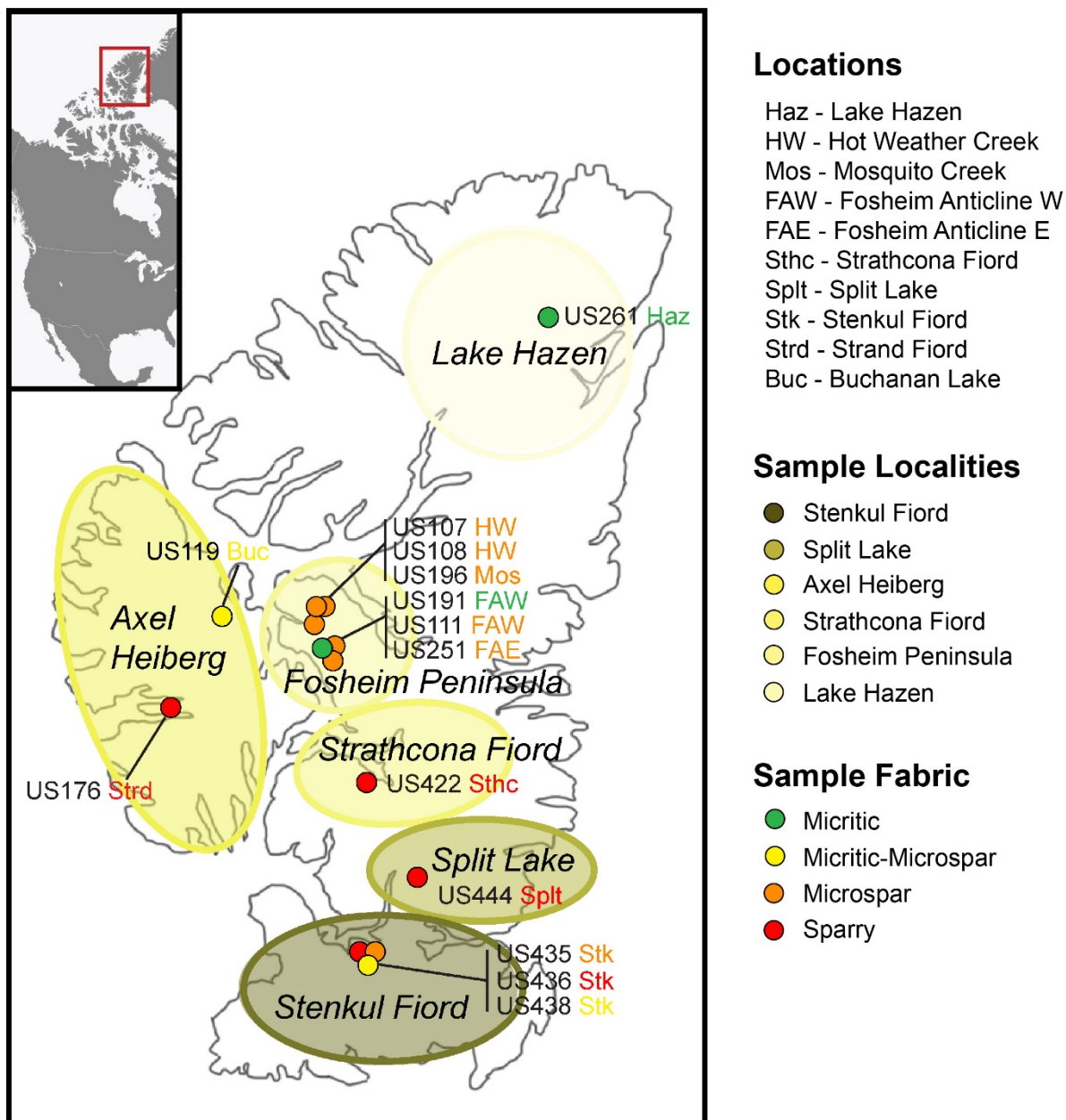


Figure 6. Sample placement map displaying carbonate fabrics. Circles in the yellow color gradient correspond to the sample localities used in Figure 3. Sample names and locations are labeled at each point. (Mic = green, Mic/MSp = yellow, MSp = orange, Spar = red).

### 3.3. Analytical Methods

Rocks were microsampled (at two separate locations I and II within each billet, Appendix B) using a carbide steel burr drill bit on a Stoelting micro drill, and subsampled from a different location on the hand sample (subsample III, Appendix B). Powdered samples were analyzed for stable ( $\delta^{18}\text{O}$ ,  $\delta^{13}\text{C}$ ) and clumped ( $\Delta_{47}$ ) isotopes at the Paleo<sup>3</sup> Laboratory at North Carolina State University. Samples were processed in a Nu Carb Automated Carbonate on-line preparation system at 70°C. Powdered samples (stable 500-700 $\mu\text{g}$ , clumped average 2200 $\mu\text{g}$ ) were digested with phosphoric acid (specific gravity 1.94-1.96), and resultant  $\text{CO}_2$  was cryogenically separated and passed through a Porapak Q trap held at -20°C. Sample  $\text{CO}_2$  was stored in the dual inlet alongside a  $\text{CO}_2$  reference gas (compositions:  $\delta^{13}\text{C}= 4.485$ ,  $\delta^{18}\text{O}= -2.450$ ).

$\delta^{18}\text{O}$ ,  $\delta^{13}\text{C}$ , and  $\Delta_{47}$  values were produced by a Nu Perspective Isotope Ratio Mass Spectrometer configured to measure m/z ratios for masses 44–49, and are reported relative to the standard VPDB (Vienna-Pee Dee Belemnite) and the absolute reference frame (Dennis et al., 2011; Defliese, 2015). Two solid standards were run before and after each set of eight unknown carbonate samples.  $\delta^{18}\text{O}$  and  $\delta^{13}\text{C}$  output was referenced to standards C64 and NBS-18;  $\Delta_{47}$  output was referenced to ETH solid standards (ETH-1, ETH-2, ETH-3, ETH-4) (Bernasconi et al., 2018; Methner et al., 2016). Data were processed using Easotope software, corrected with the 70°C calcite acid fractionation of 0.066 (Petersen et al., 2019) and the Brand et al. (2010)  $^{17}\text{O}$  correction parameters (Schauer et al., 2016; Daëron et al., 2016). Replicates with  $\Delta_{48}$  measurements exceeding  $\pm 2\text{‰}$  were rejected due to potential contamination by organics or hydrocarbons (Huntington et al., 2009; Guo & Eiler, 2007). Pierce Outlier test was used to remove statistical outliers from the stable and clumped output (Burgener et al., 2016; Huntington

et al., 2009), the standard error was measured based on a 95% confidence interval, and  $T(\Delta_{47})$  were calculated using the Petersen et al. (2019) calibration.

## 4. RESULTS

### 4.1. Sample Descriptions

Hand samples are tan to dark brown, fine-grained, and well-indurated carbonate rocks. Many hand samples have significant disseminated fine organic debris and abundant leaf fossils throughout, and do not have any visible physical shrinkage features. In thin section, samples appear to have experienced two main generations of carbonate formation (first generation micrite and spar recrystallization) but vary in the degree of secondary diagenetic alteration (Figure 5, Table 1). Sparry samples US422, US444, US436, and US176 have occasional organics and coarse spar crystals (average spar length  $\sim 55 \mu\text{m}$ , large spar crystal length  $>100 \mu\text{m}$ ) distributed throughout the thin section. Microspar samples US111, US107, US196, and US435 have moderate to high organic content with a close to an equal ratio of microspar (average spar length  $\sim 15 \mu\text{m}$ ) to micrite and organics. Microspar samples US251 and US108 have low organic content and significant spar (average spar length  $\sim 10 \mu\text{m}$ ) distribution throughout the samples. Micritic to Microspar samples US119 and US438 have low organic content and fine spar (average spar length  $\sim 7 \mu\text{m}$ ) mixed in with micrite. Micritic samples US261 and US191 have very high organic content and very low spar presence (average spar length  $<7 \mu\text{m}$ ).

### 4.2. Stable Isotopes

$\delta^{13}\text{C}$  isotope values range from  $-4.6$  to  $+12.3\%$  (VPDB) and  $\delta^{18}\text{O}$  isotope values range from  $-23.1$  to  $-15.2\%$  (VPDB), see Figure 7. Samples within each fabric type (Micritic, Micritic

to Microspar, Microspar, and Sparry) have carbon isotope ( $\delta^{13}\text{C}$ ) averages of 9.8‰, 4.5‰, 3.4‰, 2.0‰. Samples within each fabric type have oxygen isotope ( $\delta^{18}\text{O}$ ) averages of -17.2‰, -17.8‰, -18.0‰, -18.9‰ respectively, see Table 2 and Figure 8.

Table 2. Stable Isotope Data

Sample	Age	Location	Fabric	Avg $\delta^{13}\text{C}$	SE ( $\delta^{13}\text{C}$ )	Avg $\delta^{18}\text{O}$	SE ( $\delta^{18}\text{O}$ )
US119	MID E	Buchanan	Mic/MSp	2.73	0.099	-18.61	0.271
US444	LP - EE	Split	Spar	4.86	0.070	-23.12	0.140
US107	LP - EE	Hot Weather	MSp	2.60	0.097	-16.86	0.139
US108	LP - EE	Hot Weather	MSp	3.10	0.047	-17.31	0.035
US435	LP - EE	Stenkul	MSp	7.95	0.114	-18.07	0.088
US436	LP - EE	Stenkul	Spar	5.42	0.574	-17.14	0.398
US438	LP - EE	Stenkul	Mic/MSp	6.31	0.046	-17.06	0.161
US261	LP - EE	Hazen	Mic	12.32	0.094	-15.67	0.052
US191	LP - EE	Fosh Ant W	Mic	7.23	0.130	-18.74	0.053
US111	LP - EE	Fosh Ant W	MSp	2.68	0.121	-17.17	0.227
US251	LP - EE	Fosh Ant E	MSp	1.47	0.078	-19.36	0.196
US422	LP - EE	Strathcona	Spar	2.09	0.024	-15.21	0.260
US196	LP - EE	Mosquito	MSp	2.45	0.029	-19.33	0.187
US176	LP - EE	Strand	Spar	-4.56	0.166	-20.32	0.803

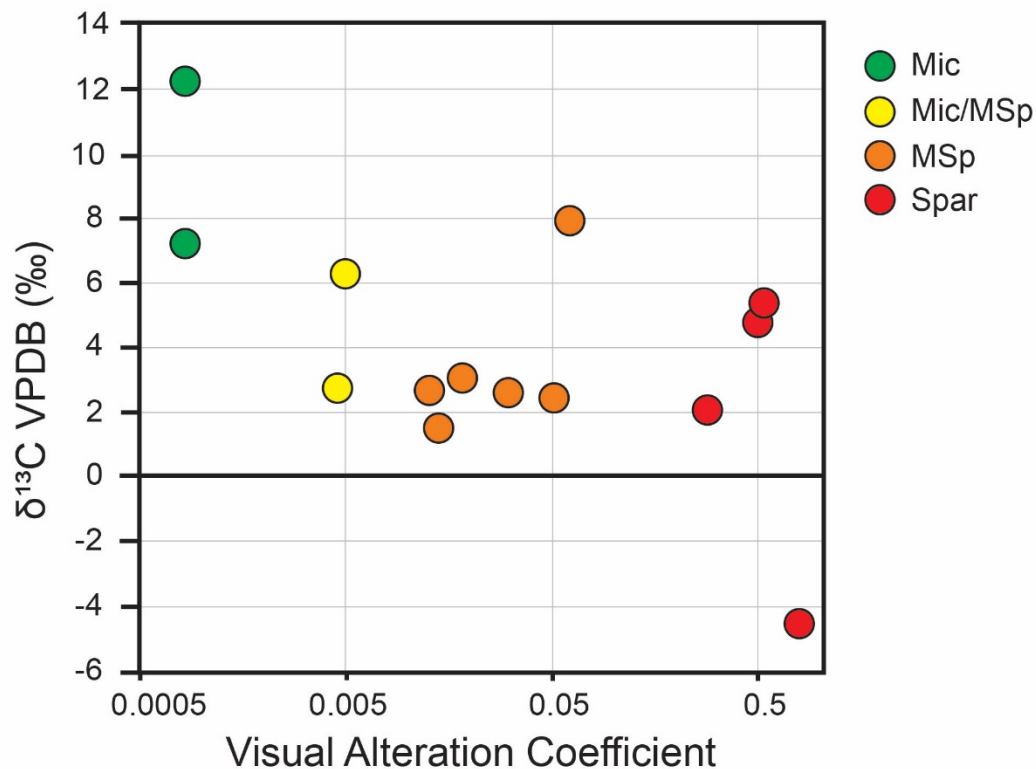


Figure 7a. Visual Alteration Coefficient vs. carbon isotope compositions.

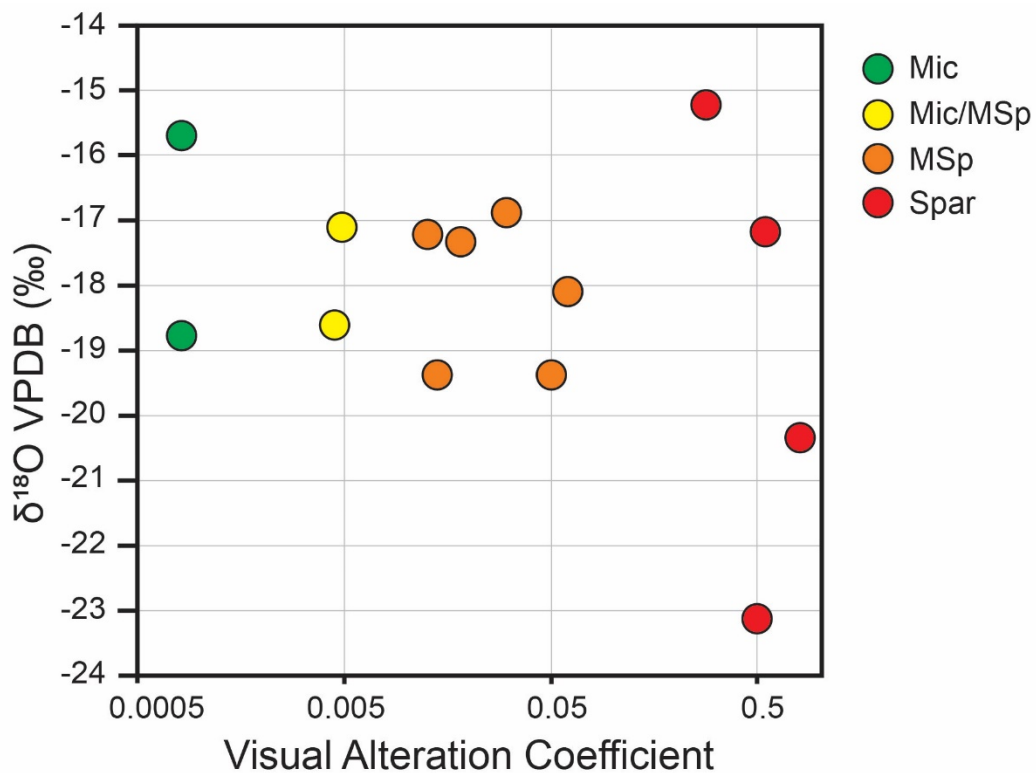


Figure 7b. Visual Alteration Coefficient vs. oxygen isotope compositions.

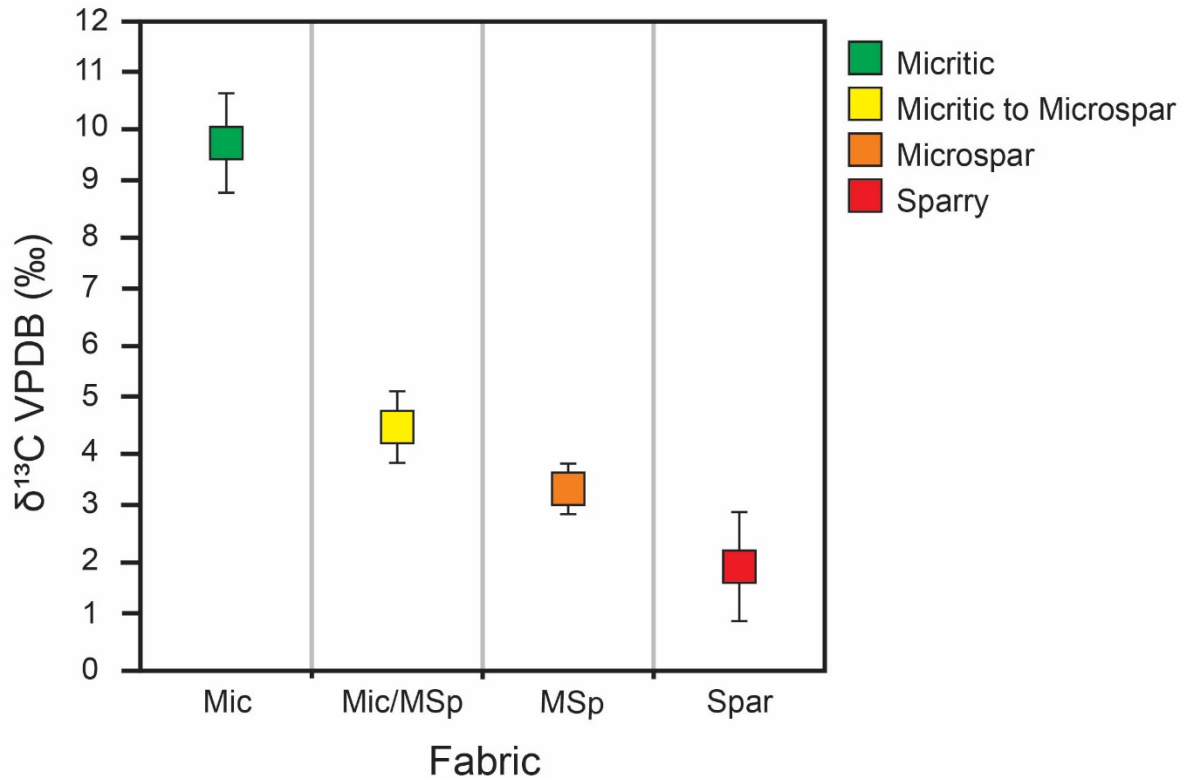


Figure 8a. Stable carbon isotope data plotted against fabric classification. Isotope data averaged within each fabric type, vertical lines show standard deviation.

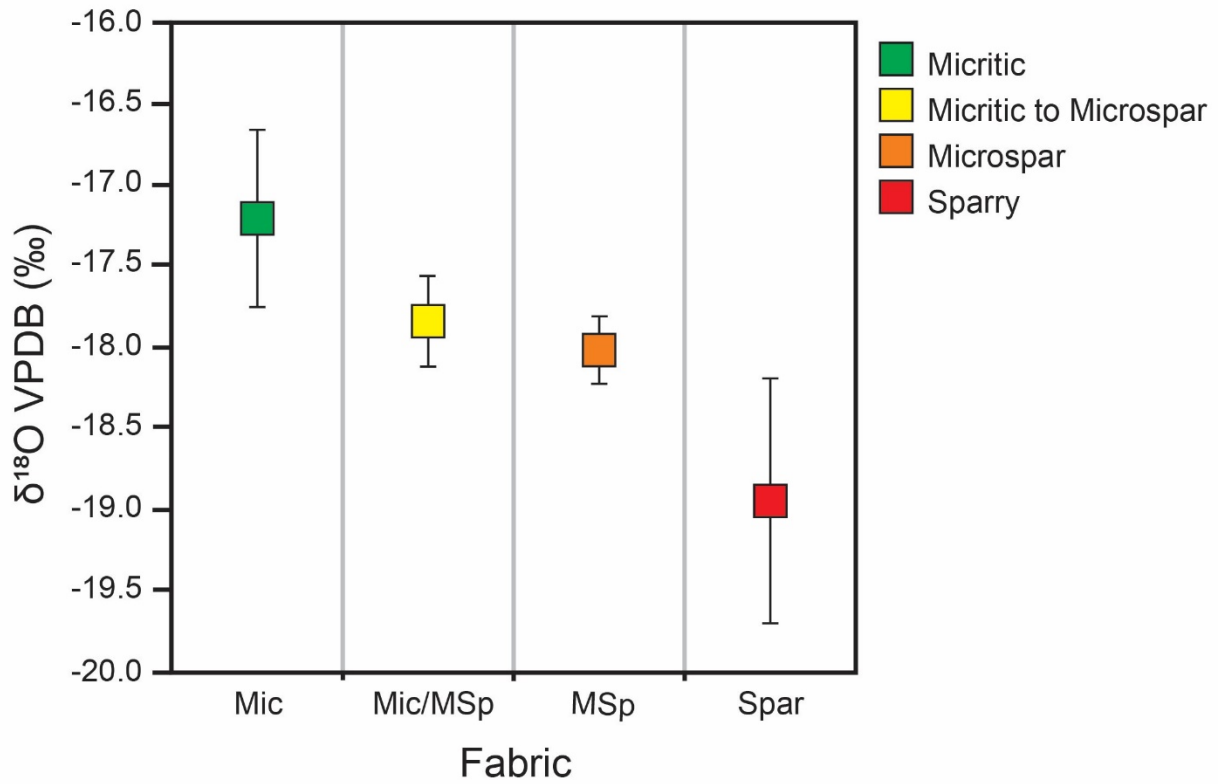


Figure 8b. Stable oxygen isotope data plotted against fabric classification. Isotope data averaged within each fabric type, vertical lines show standard deviation.

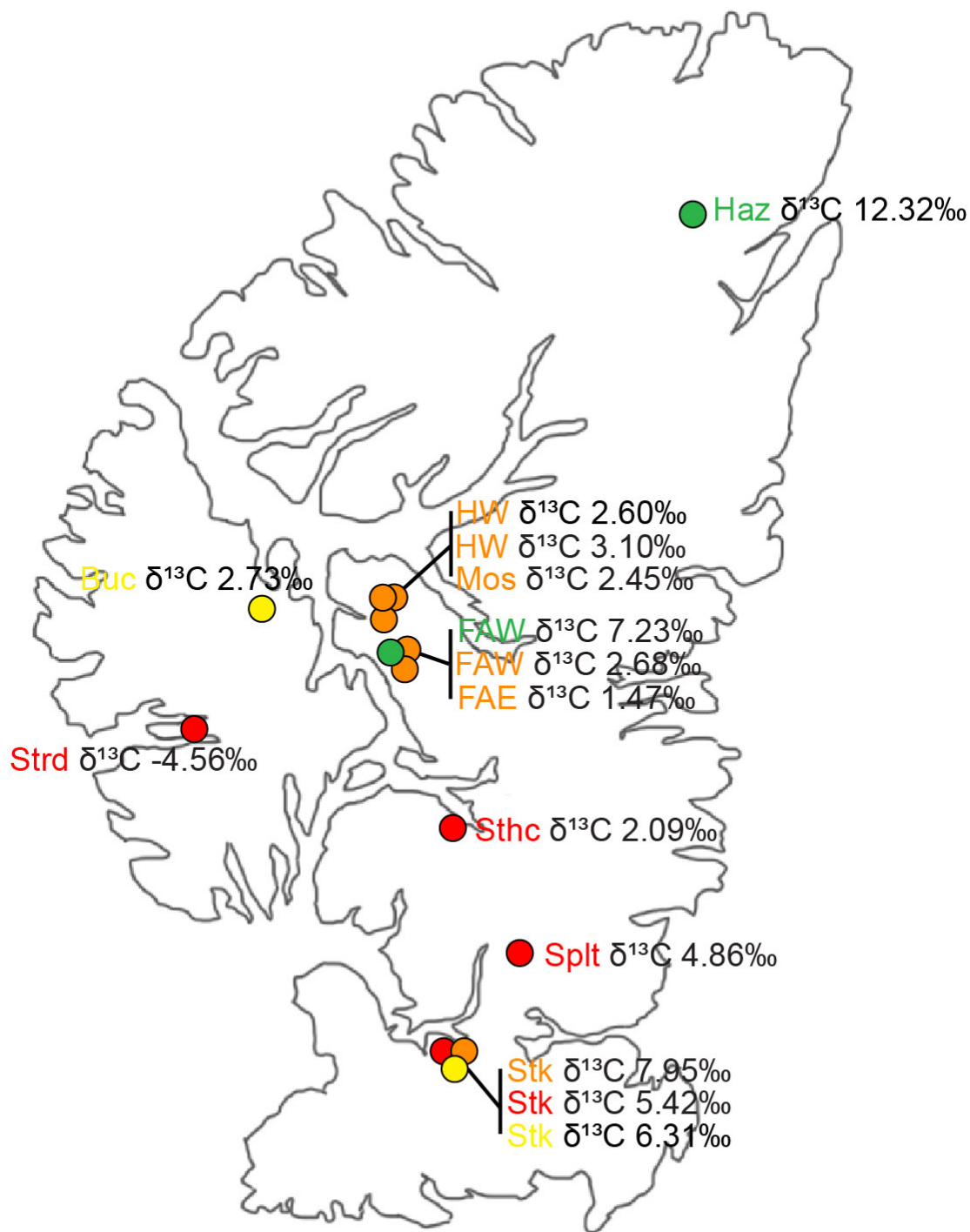


Figure 9a. Stable carbon isotope data plotted spatially on Ellesmere and Axel Heiberg Islands. Stable isotope data plotted spatially alongside location code and visual alteration class (Mic = green, Mic/MSp = yellow, MSp = orange, Spar = red).

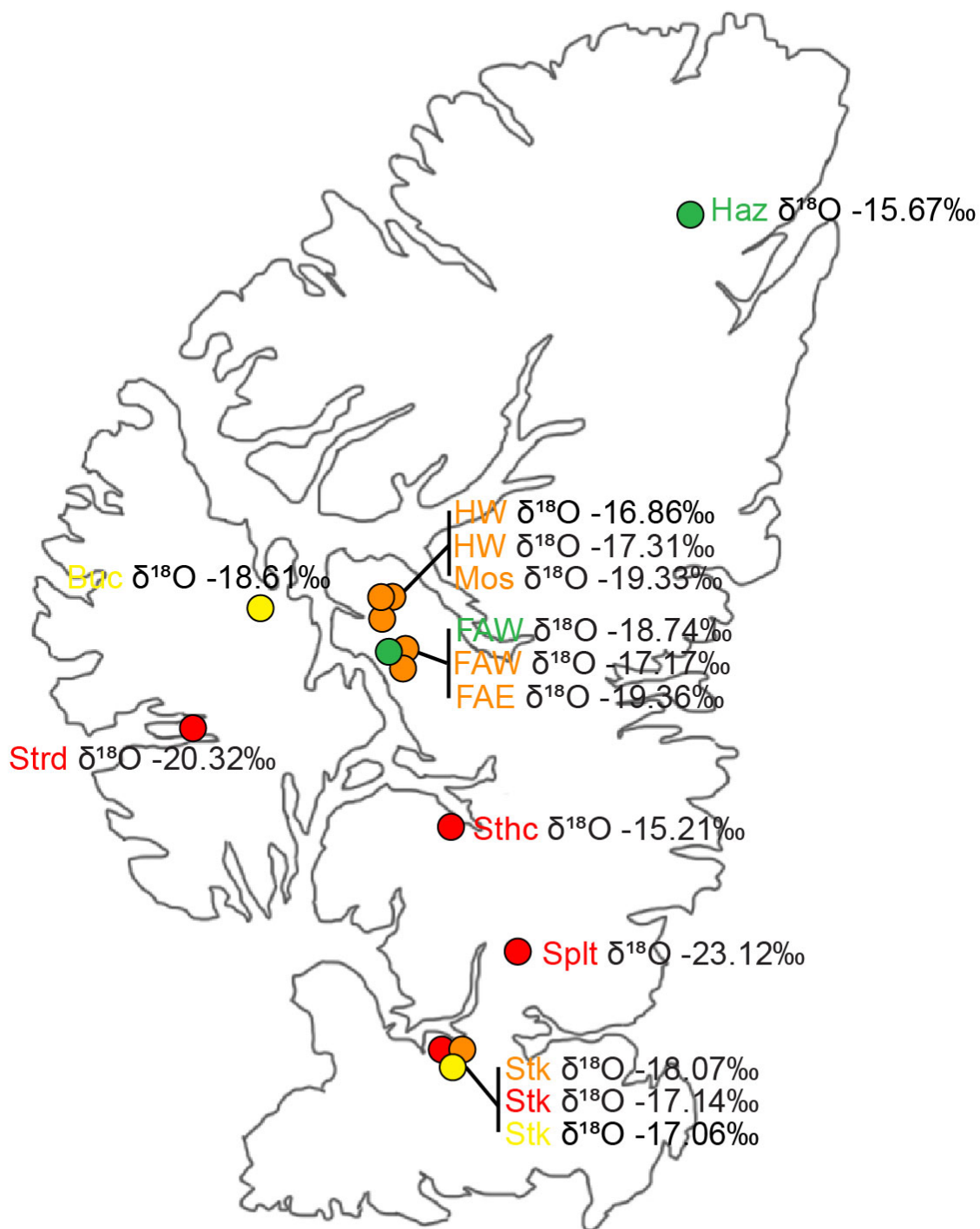


Figure 9b. Stable oxygen isotope data plotted spatially on Ellesmere and Axel Heiberg Islands. Stable isotope data plotted spatially alongside location code and visual alteration class (Mic = green, Mic/MSp = yellow, MSp = orange, Spar = red).

### 4.3. Clumped Isotopes

Clumped isotope ( $\Delta_{47}$ ) values range from 0.505 to 0.621‰ (CDES) with resulting temperature estimates from 52 to 121 °C. Temperatures were on average hotter for samples that have experienced more significant alteration (Spar and Microspar, 86 °C; Micritic and Micritic-to-Microspar, 60 °C; Figure 10). Table 3 shows the number of replicates for each sample, average  $\Delta_{47}$  of replicates, standard error, and calibrated temperatures.

Table 3. Clumped isotope data.

Sample	Age	Location	Vis Alt	Fabric	Reps	Avg $\Delta_{47}$	SE ( $\Delta_{47}$ )	Temp °C
US119	MID E	Buchanan	0.0045	Mic/MSp	6	0.604	0.018	59.6
US444	LP - EE	Split	0.5	Spar	5	0.599	0.026	62.2
US107	LP - EE	Hot Weather	0.03	MSp	6	0.529	0.018	102.5
US108	LP - EE	Hot Weather	0.018	MSp	6	0.558	0.033	84.2
US435	LP - EE	Stenkul	0.06	MSp	7	0.567	0.016	79.0
US436	LP - EE	Stenkul	0.54	Spar	5	0.542	0.012	94.2
US438	LP - EE	Stenkul	0.0048	Mic/MSp	8	0.596	0.021	63.2
US261	LP - EE	Hazen	0.0008	Mic	6	0.621	0.032	51.6
US191	LP - EE	Fosh Ant W	0.0008	Mic	8	0.589	0.025	66.8
US111	LP - EE	Fosh Ant W	0.0125	MSp	6	0.555	0.021	86.0
US251	LP - EE	Fosh Ant E	0.014	MSp	6	0.505	0.03	120.6
US422	LP - EE	Strathcona	0.28	Spar	7	0.570	0.02	77.4
US196	LP - EE	Mosquito	0.05	MSp	6	0.618	0.023	52.9
US176	LP - EE	Strand	0.8	Spar	5	0.525	0.000	105.6

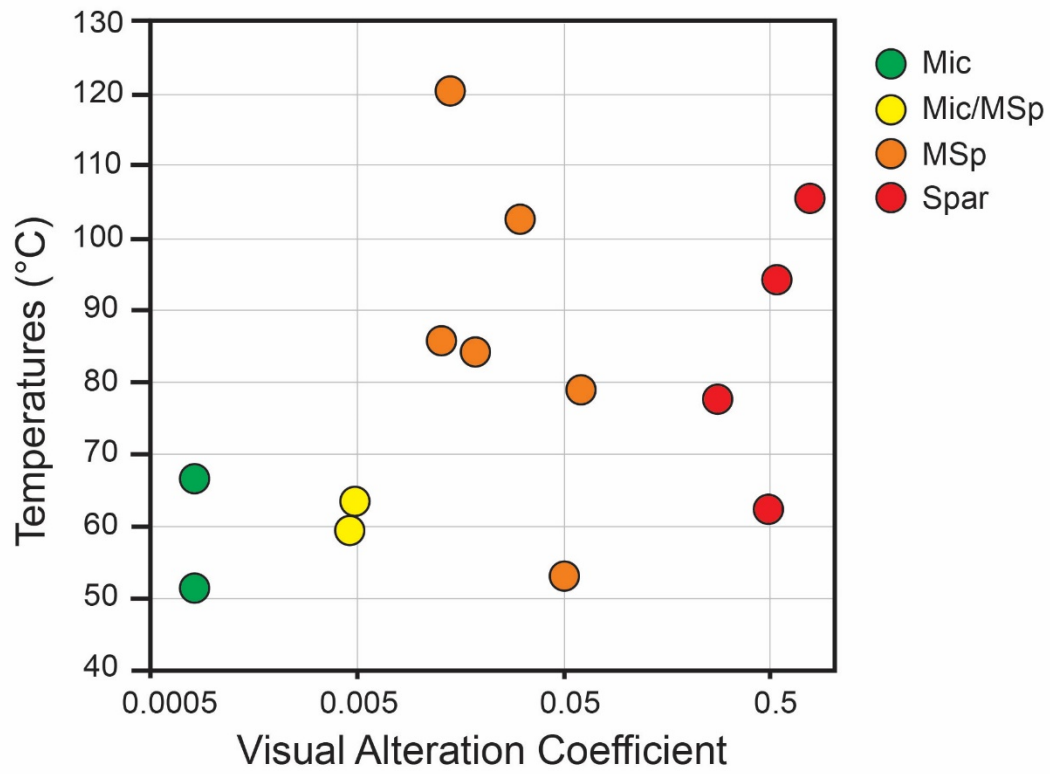


Figure 10. Plot of  $T(\Delta_{47})$  versus Visual Alteration Coefficient.

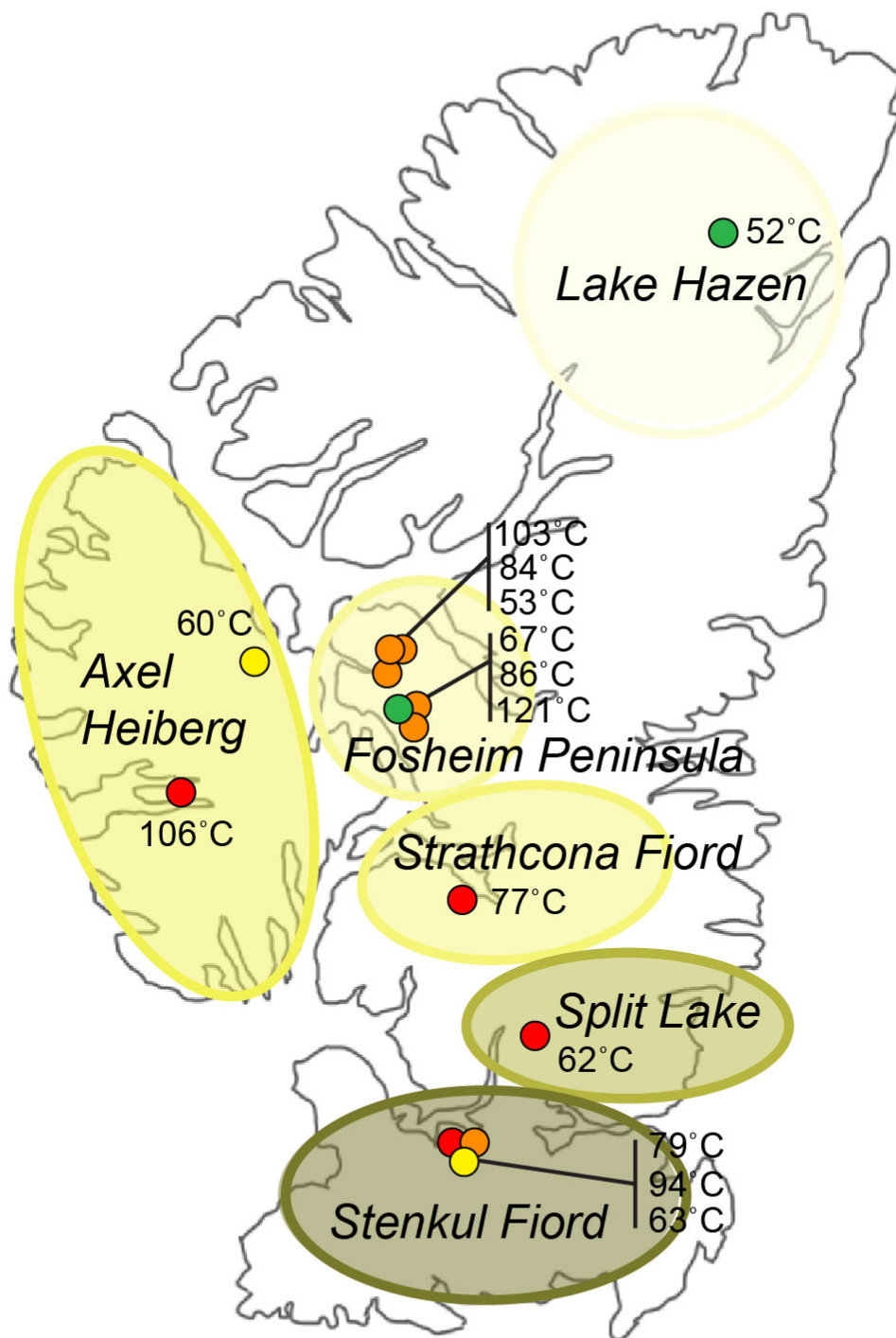


Figure 11. Clumped isotope-derived temperatures plotted spatially. Temperatures plotted alongside visual alteration class (Mic = green, Mic/MSp = yellow, MSp = orange, Spar = red) and locality zone (yellow color gradient ellipses correspond to Figures 1 and 3).

## 5. DISCUSSION

### 5.1. Sample Interpretations

Evaluation of the hand-samples and thin-sections provides a baseline to examine the conditions impacting the corresponding isotope values. High leaf fossil preservation in hand-samples suggests a consistently wet depositional environment with a high water table, most similar to an initial lake setting. Additionally, lack of calcrete characteristics and physical shrinkage features indicates that the deposits did not develop in environments with fluctuating ground water tables or water level (Tandon & Andrews, 2001). The absence of other critical pedogenic alteration features suggests that the samples experienced minimal subaerial exposure and pedogenesis (Marty & Meyer, 2006). Due to lack of surface alteration features, all subsequent interpretations assume the samples are lake setting palustrine carbonates and are considered “less developed” palustrine carbonates (Alonso-Zarza, 2003). Well-indurated hand samples indicate primary micrite is mixed with recrystallized phases, and samples may have undergone varying degrees of aggrading neomorphism from pore fluid (Alonso-Zarza et al, 2006).

In thin section, consistent coarse spar distribution within Microspar and Sparry samples suggest they experienced burial diagenesis. The scaled percentage of spar coverage, see Section 3.2, was used to evaluate the isotope data within respective fabric categories (Mic, Mic/MSp, MSp, Spar). By using a numerical classification scheme, changes in primary carbonate fabrics can be more accurately quantified to indicate how much alteration occurred due to burial and reheating. This numerical value, referred throughout the text and figures as a Visual Alteration Coefficient, quantifies visual evidence of increasing amounts of reheating and diagenetic alteration experienced by a sample. It is important to note that this Visual Alteration Coefficient

works on the uncertain assumption that spar size and the ratio of spar-to-micrite have an equal effect on the scaled percentage.

## **5.2. Primary Carbonate Stable Isotope Interpretations**

### **5.2.1. Primary Carbon Isotopes**

Primary  $\delta^{13}\text{C}$  values reflect the varying influences of the biogenic  $\delta^{13}\text{C}$  composition ( $\text{C}_3$  or  $\text{C}_4$  biomass or lake productivity) and atmospheric  $\text{CO}_2$  composition (Bernasconi & McKenzie, 2007). High microbial and algal lake productivity cause primary carbonates to have more negative  $\delta^{13}\text{C}$  values (Alonso-Zarza, 2003); however, the positive 2.7 to 12.3‰ Micritic and Micritic to Microspar carbon isotopic values do not suggest an initially productive lake setting and are unusually high when compared against the typical palustrine carbonate range of  $-2$  to  $-11$ ‰ ( $\delta^{13}\text{C}$ ) (Tandon & Andrews, 2001). Unusually positive carbon isotope values for micritic samples (7.2 to 12.3‰) would require a mechanism that causes significant  $\delta^{13}\text{C}$  enrichment in the initial settings. The two most likely enrichment mechanisms, based on the location and depositional environments, are cryogenic kinetic isotope effects and repeated dissolution-precipitation enrichment.

Cryogenic kinetic isotope effects are associated with bicarbonate dehydration in freezing conditions (below  $0^\circ\text{C}$  conditions), which results in  $\text{CaCO}_3$  supersaturation (Burgener et al., 2018). Cryogenic kinetic isotope effects typically increase both  $\delta^{18}\text{O}$  and  $\delta^{13}\text{C}$  values and additionally cause negative  $\Delta_{47}$  anomalies (Tripathi et al., 2015; Burgener et al., 2018). Negative  $\Delta_{47}$  anomalies are not present in the clumped isotope data, and the site locations did not experience below zero temperatures for extended periods (e.g. Basinger et al., 1994; Jahren & Sternberg, 2003). Furthermore, the  $\delta^{18}\text{O}$  values are not enriched relative to the expected

environmental water  $\delta^{18}\text{O}$  composition (see Section 5.2.2; Jahren & Sternberg, 2008), and therefore it is unlikely that cryogenic kinetic isotope effects are responsible for enriching the primary carbonate  $\delta^{13}\text{C}$  values.

The other potential enrichment mechanism affecting the carbon values is repeated dissolution-precipitation enrichment, which would increase the carbon isotope values without changing primary oxygen isotope values. Repeated cycles of carbonate dissolution and reprecipitation behaves in an asymptotic function, approaching a maximum  $\delta^{13}\text{C}$  enrichment value (Nakai et al., 1975; Clark & Lauriol, 1992; Burgener et al., 2018). Repeated dissolution-precipitation cycles occurring to micrite deposits along lake margins (similar to the sample depositional environments) would result in high carbon enrichment within carbonates.

Enrichment due to dissolution-precipitation cycles were modeled using the equations, fractionation factor, and methods described in Burgener et al. (2018; see also: Nakai et al., 1975; Clark & Lauriol, 1992; Bottinga, 1968). By accounting for enrichment, one can approximate the varying influence of biomass and atmospheric compositions on the carbon isotope values. End member compositions were approximated as -25‰ for  $\text{C}_3$  vegetation, the primary vegetation type during the Eocene, and -5.9‰ for late Paleocene to early Eocene and -6.9‰ for the middle Eocene atmospheric  $\text{CO}_2$  (Schaetzl & Anderson, 2005; Urban et al. 2010; Jahren & Sternberg, 2008; Tipple et al., 2010). Cold month mean temperature (CMMT) was approximated at 2 °C, mean annual temperature (MAT) was approximated at 12 °C, and warm month mean temperature (WMMT) was approximated at 22 °C (Schubert et al., 2012; Eberle et al., 2010; Jahren & Sternberg, 2003; Greenwood & Wing, 1995; Basinger et al., 1994; Wolfe, 1994). Comparing maximum enrichment from the different variable combinations indicates that the most significant influence on  $\delta^{13}\text{C}$  for the samples is the temperature of carbonate precipitation (cold month mean

temperature) and atmospheric CO<sub>2</sub> composition. This combination of variables with repeating dissolution-precipitation cycles would result in around 10.4‰ enrichment of sample δ<sup>13</sup>C for late Paleocene to early Eocene carbonates and 9.4‰ enrichment of sample δ<sup>13</sup>C for middle Eocene carbonates. Using a modified CMMT range of -3 °C to 13 °C (West et al., 2015), the possible range for δ<sup>13</sup>C enrichment due to dissolution in heavy summer rain and multiple cycles of reprecipitation during drier winter conditions is approximately 8 to 11‰, agreeing with the range of enrichment seen in the less-altered carbonate samples. This level of enrichment in the samples would suggest that the majority of the influence on the carbonate δ<sup>13</sup>C values would be from the composition of atmospheric CO<sub>2</sub>, with very little (or no) influence of vegetation or biological productivity.

Using approximations from the two-component end-member mixing model makes it possible to work backward and approximate the environmental conditions during carbonate formation necessary to produce this level of primary δ<sup>13</sup>C enrichment (e.g., Burgener et al., 2018). Examples of dissolution-precipitation cycles resulting in δ<sup>13</sup>C enrichment in the modern are all located in high latitude sites, such as Svalbard (e.g., Courty et al., 1994). Modern carbonates formed in high latitude areas may experience this enrichment mechanism due to the pattern of continuous darkness, resulting in low productivity and dry conditions, followed by continuous sunlight, associated with an influx of summer snowmelt flooding soils (Burgener et al., 2018). Our Eocene setting had similar continuous darkness and sunlight patterns, but likely did not have snowmelt (Jahren, 2007). Therefore, for this enrichment to occur, a large flux of water would need to be present in the summer. Seasonal precipitation variability can affect the timing of carbonate precipitation (e.g. Breecker et al., 2009; Gallagher & Sheldon, 2016), which

would provide an explanation for carbonate formation during the winter and additionally supports the highly seasonal summer-wet Arctic precipitation hypothesis (see Section 2.1.2).

Isotopic studies suggesting monsoonal summer-wet precipitation conditions in the Arctic during early Eocene hyperthermals (e.g., Schubert et al., 2012) conflict with other Arctic studies and models that indicate Eocene polar conditions with low precipitation seasonality and “ever-wet” or equable conditions (e.g., Eberle & Greenwood, 2012; Huber & Goldner, 2012). A recent examination of leaf physiognomy in similar formations and localities agree with approximations for high summer precipitation during this time, but do not explicitly support monsoonal conditions, and additionally suggest consistent precipitation even though summers and winters would have driven regional warmth (e.g., West et al., 2015).

Overall, having both dissolution-precipitation enrichment and an exclusively atmospheric enrichment for the samples requires a specific pattern of summer carbonate dissolution and winter carbonate precipitation. This pattern most aligns with a monsoonal summer-wet climate, with enhanced summer rainfall. The carbon isotope record from this study supports the high summer rainfall approximations in other studies (e.g., Eberle & Greenwood, 2012; Huber & Goldner, 2012; West et al., 2015), but also strongly suggests possible monsoonal conditions (e.g., Schubert et al., 2012), or at least a very significant difference in saturation conditions between summer and winter in these environments. This would agree with the highly seasonal precipitation results of the fossil wood isotope record in Schubert et al. (2012), one of their sites being Stenkul Fiord (in the Margaret Formation), which also matches one of our sample locations.

While this study suggests potential monsoonal conditions, there is insufficient data to rule out the ever-wet conditions detailed in other studies conclusively (e.g., West et al., 2015). It may

be possible for similar enrichment to occur in the ever-wet conditions; however, if so, winters would have needed to be significantly drier than summers to result in enough episodic drying for exclusive winter carbonate formation.

### 5.2.2. Primary Oxygen Isotopes

When interpreting primary oxygen isotope values, changes reflect a relationship between local temperature, evaporation, and precipitation. Absence of ice from the late Paleocene to middle Eocene would cause ocean water to begin with an overall lower initial  $\delta^{18}\text{O}$  value than during times of extensive ice cover (e.g., Zachos et al., 2008). Additionally,  $^{18}\text{O}$  concentration decreases with increasing latitude and elevation, which would further reduce the initial  $\delta^{18}\text{O}$  ratio in this region (Dansgaard, 1964; Bowen, 2010). With a typical terrestrial system, decreased  $\delta^{18}\text{O}$  indicates further distance from the ocean, as clouds carrying evaporated ocean water rain out heavier  $^{18}\text{O}$  first and become more negative further inland. In the present case, all of the sample locations are close to ocean water due to the small size of the islands, and therefore it is unlikely that significant Rayleigh distillation would affect the  $\delta^{18}\text{O}$  values as clouds bring rainwater from the ocean onto the land.

$\delta^{18}\text{O}$  is affected by ocean water composition and temperature-dependent fractionation occurring between the calcite and original lake source water (Kim & O'Neil, 1997; Cerling & Quade 1993; Alonso-Zarza, 2003). The previous carbon interpretations suggest the bulk of primary carbonates precipitated during winter with continuous darkness conditions resulting in minimal photosynthetic influence. Assuming the interpretations made from the carbon isotope system are reasonable,  $\delta^{18}\text{O}$  would not be significantly impacted by biogenic fractionation. Additionally, the dissolution/reprecipitation mechanism does not inherently affect  $\delta^{18}\text{O}$  values

(Burgener et al., 2018), so it is assumed that the  $\delta^{18}\text{O}$  values are not affected by this mechanism if the source water composition is assumed to have not changed significantly during this timeframe.

As a result, the dominant influence on the sample  $\delta^{18}\text{O}$  composition is the temperature and the environmental water  $\delta^{18}\text{O}_{\text{SMOW}}$  composition, previously approximated to be around -15 to -19‰ on Axel Heiberg Island during the middle Eocene (Jahren & Sternberg, 2008). In order to compare Jahren & Sternberg's environmental water values to this study's results, VPDB values were converted to soil/source water values on the VSMOW scale using the Kim & O'Neil (1997) calcite-water isotope fractionation equation:

$$\delta^{18}\text{O}_{\text{calcite}} \approx \delta^{18}\text{O}_{\text{water}} + 18.03 * (10^3 / T) + 32.42 \quad \text{[EQN from Kim \& O'Neil, 1997]}$$

Using a 2 °C estimate for CMMT (e.g., West et al., 2015; Schubert et al., 2012; Eberle et al., 2010; Jahren & Sternberg, 2003; Greenwood & Wing, 1995; Basinger et al., 1994; Wolfe, 1994), based on the assumption that the studied carbonates formed primarily during winter, the converted environmental water  $\delta^{18}\text{O}_{\text{SMOW}}$  values for micritic samples range from -17.8 to -20.5‰. Within each fabric type,  $\delta^{18}\text{O}_{\text{SMOW}}$  averages are -19.8‰ (Mic), -20.5‰ (Mic/MSp), -20.6‰ (MSp), and -21.6‰ (Spar) respectively. The previous fossil wood isotopic study of Jahren and Sternberg (2008) also inferred that increased temperatures caused the environmental water reservoir, used for plant uptake, to become enriched in  $^{18}\text{O}$  during the growing season. As a result, it is reasonable that winter-precipitated primary micrite samples (environmental water  $\delta^{18}\text{O}_{\text{SMOW}}$  average for Mic and Mic/MSp samples are approximately -20‰), would have slightly lower  $\delta^{18}\text{O}_{\text{SMOW}}$  values than values recorded during a presumable growing season (e.g., -19‰; Jahren & Sternberg, 2008). Additionally, these slightly lower  $\delta^{18}\text{O}_{\text{SMOW}}$  values may further

support the previous carbon isotope findings that the studied samples are unique winter-precipitated carbonates.

### 5.3. Secondary Carbonate Stable Isotope Interpretations

The palustrine stable isotope values are further controlled by diagenetic burial alteration. This general pattern is visible by the averages within each fabric class, with carbon ( $\delta^{13}\text{C}$ ) averages decreasing from 9.8‰ for Mic, 4.5‰ for Mic/MSp, 3.4‰ for MSp, and 2.0‰ for Spar, and oxygen ( $\delta^{18}\text{O}$ ) averages decreasing from -17.2‰ for Mic, -17.8‰ for Mic/MSp, -18.0‰ for MSp, and -18.9‰ for Spar. Both  $\delta^{13}\text{C}$  and  $\delta^{18}\text{O}$  averages display a slight overall decrease with increased alteration, showing a transition from Mic and Mic/MSp describing the primary micrite (original surface water composition) to MSp and Spar samples describing the secondary calcite spar (burial fluid composition) (Dunagan and Turner, 2004; Tandon & Andrews, 2001).

Due to the lack of pedogenic and diagenetic surface alteration features (see Section 4.1 and Section 5.1), and classification of samples as “less developed” lake setting palustrine carbonates, this study neglects the small differences associated with the possible surface alteration. Instead, it is assumed that the most significant influence on  $\delta^{13}\text{C}$  and  $\delta^{18}\text{O}$  decreases between primary and secondary calcite are due to burial-related diagenetic alteration.

Variations in  $\delta^{13}\text{C}$  within each respective alteration class likely reflects different ratios of the original amount of carbon within the system (dominated by the atmospheric  $\text{CO}_2$  composition) relative to a subsequent source of inorganic carbon (from the burial fluids that diagenetically altered the deposits). This secondary influx of depleted carbon is likely sourced from hydrothermal fluids that dissolved more deeply buried carbonates – for example, deeper Permian-Triassic aged carbonates from these locations have  $\delta^{13}\text{C}_{\text{org}}$  around -25 to -30‰ (Grasby

& Beuchamp, 2008) which would be roughly approximated by  $\delta^{13}\text{C}$  carbonate values around -10 to -15‰ (Oehlert & Swart, 2014).

Gradual decreases in  $\delta^{18}\text{O}$  from micritic to secondary calcite samples likely reflect the temperature-dependent fractionation of  $\delta^{18}\text{O}$  as the spar crystallized out of hot diagenetic fluids (Kim & O'Neil, 1997; Tandon & Andrews, 2001). Burial alteration occurs at hotter subsurface temperatures, which results in a lower  $\delta^{18}\text{O}_{\text{calcite}}$  value – this relationship is shown in the Kim & O'Neil (1997) calcite-water isotope fractionation equation (see Section 2.3.3.c or Section 5.2.2 for the full equation).

#### **5.4. Clumped Isotope Interpretations**

Clumped isotope ratios of 0.505 to 0.621‰ (CDES), which correspond to 52 to 121 °C, do not reflect surface temperatures. Even micritic primary samples, which did not undergo significant diagenetic alteration, return an average temperature of 60 °C, likely due to solid-state reordering during burial. For micritic samples, the clumped isotope values were affected by burial-related heating, but the primary stable isotope values were not affected. This is because clumped isotope values are more sensitive to burial diagenesis than stable isotope values (Winkelstern & Lohmann, 2016).

Samples with microspar and spar present have clumped isotope values indicating formation at an average temperature of 86 °C, suggesting that clumped isotope output reflects a combination of the original micritic formation temperature mixed with the secondary diagenetic spar formation temperature. The clumped isotope temperature output generally increases when plotted by Visual Alteration Coefficient, see Figure 10, which theoretically represents a scale of least to most visual evidence of heating and diagenetic alteration.

### 5.4.1. Reordering Burial Temperatures

Rapid subsidence of the eastern Sverdrup basin resulted in increased sediment accumulation rates from the Late Cretaceous to the middle Eocene (e.g., Embry & Beuchamp, 2008; Dewing & Obermajer, 2011; Von Gosen et al., 2019). This regional burial event was followed by widespread regional uplift during the middle Eocene and onward (e.g., Dewing & Sanei, 2009; Von Gosen et al., 2019), see Figure 12 (which contains tectonic setting and thermal information adapted from Figure 2 in Dewing & Sanei, 2009). The suite of samples was deposited during this burial event, and appear to record these regional signals. Micritic samples indicating 52 to 67 °C temperatures likely reflect solid-state reordering of clumped isotope bonds due to burial-heating (Passey & Henkes, 2012; Henkes et al., 2014).

Due to uncertainty about the exact ages of the samples and specific timing of the Eurekan Orogeny (see Section 2.2.2), the general regional burial and uplift event time estimates from Dewing and Sanei (2009) were used to approximate the parameters for the Clumped Isotope Reordering Model. Depending on the sample ages and depositional setting, million-year timesteps were allocated for each of the four “events” that occurred following winter carbonate formation: 1. consistent burial (5-10 million years), 2. stationary at max burial depth (10-15 million years), 3) consistent uplift (15-25 million years), and 4. stationary at the surface (~10 million years). This scenario sets up a realistic burial and uplift path based on the events of the Eurekan Orogeny (see Section 2.2.2 and Figure 12).

The model simulates each carbonate rock sample transitioning through these four “events” following its formation to the present, and calculates how much the initial clumped isotope value decreases, from a hypothetical 0.765‰ (corresponding to a 2 °C CMMT) to the measured 0.621-0.589‰, due to burial related reordering. By using a cold 2 °C initial

temperature, the model calculates the greatest amount of heating required to reorder the clumped isotope bonds, and obtains the maximum burial temperature estimates for the micritic samples.

Obtaining maximum burial temperatures and modeling changes in clumped isotope values through time is possible due to predictable reordering behavior (see Section 2.3.3.b for context on clumped isotope reordering; Passey & Henkes, 2012; Stolper & Eiler, 2015). The present mathematical model uses equations and calculated values from Passey & Henkes (2012):

$$\Delta_{47}^i = (\Delta_{47}^{i-1} - \Delta_{47}^{eq,i}) \exp\{-\Delta t k_{ref} \exp[(E_a/R) * ((1/T_{ref}) - (1/T))]\} + \Delta_{47}^{eq,i} \quad [\text{EQN13}]$$

Equation 13 was applied in the Clumped Isotope Reordering Model, alongside the subsequently described parameters, and additional values listed out in the code in Appendix A.

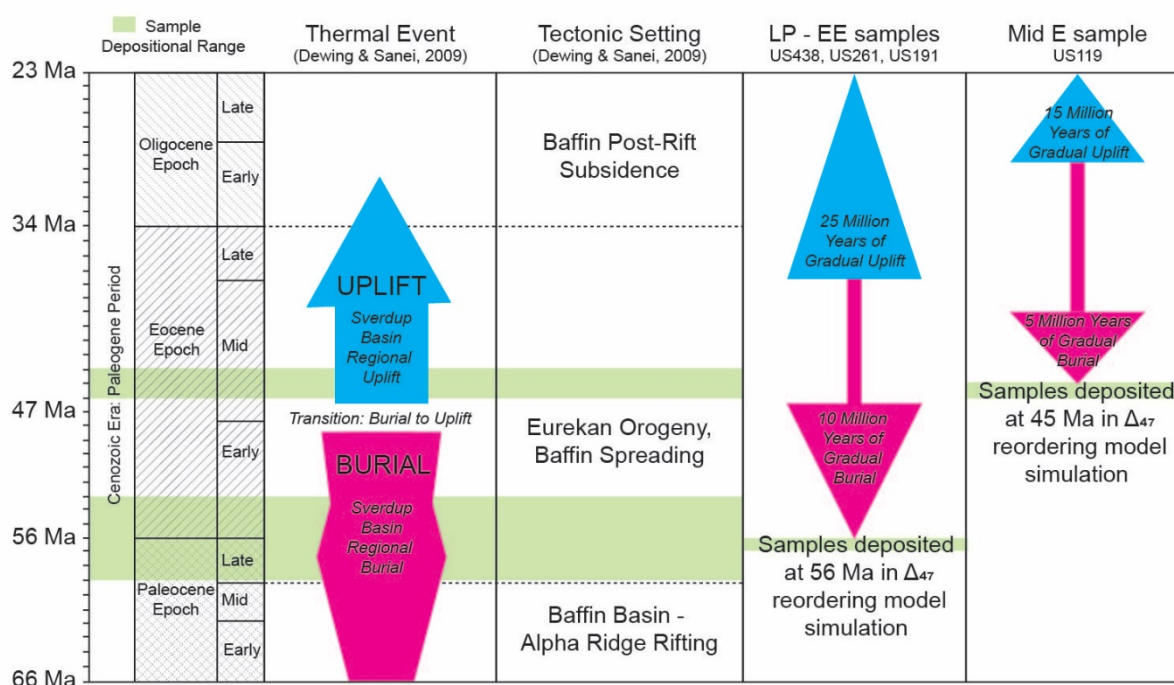


Figure 12. Regional burial and uplift signal modeled within the micritic samples. The general time approximations of burial and uplift for the region were used to assign each event duration. LP-EE samples shows the timing of late Paleocene to early Eocene samples, while Mid E sample shows the timing of the middle Eocene sample. Thermal events and tectonic settings information directly taken from Figure 2 in Dewing & Sanei (2009).

#### 5.4.1.a. Reordering Model Parameters

Previous studies comparing heating due to burial depth against heating from differential heat flow found a consistent thermal response to burial depth and relatively similar geothermal heat gradients across the Canadian Arctic Islands (Dewing & Sanei, 2009). This finding disagrees with older approximations of the regional geothermal gradient, which ranged between 20 to 55 °C/km depending on the geographic location (Bustin, 1986). For the assumptions and model parameters, this study uses a consistent 50 °C/km geothermal gradient estimate. This geothermal gradient was used for similar locations in the Bustin (1986) paper, but more closely agrees with the more recent Dewing & Sanei (2009) interpretation of relatively consistent geothermal gradients across both islands, based on their study that evaluated thermal maturity dataset quality. Assuming a relatively consistent geothermal gradient across both Axel Heiberg and Ellesmere Islands (e.g., Dewing & Sanei, 2009), changes in micritic sample clumped isotope values due to regional burial and uplift events were modeled to calculate maximum burial temperatures.

The sample ages used in the model were 56 Ma for US438, US261, and US191 and 45 Ma for US119. An original micrite formation temperature of 2 °C was used, based on the assumption that the carbonates precipitated in the winter season, which had a CMMT of approximately 2 °C (e.g., Basinger et al., 1994; Greenwood & Wing, 1995; Jahren & Sternberg, 2003).

The model was iterated using two sets of parameters for optical calcite (ideal and homogenous) and labile spar (unstable and heterogeneous). Differences between the optical calcite and labile spar parameters are defined within the model code in Appendix A. Optical calcite is more applicable to these four micritic samples, and Figure 13 shows the optical calcite

results. Additional plots comparing the optical calcite against labile spar output are presented in Appendix A.

#### Late Paleocene and Early Eocene Samples: US438, US261, US191

The regional burial and regional uplift events that the late Paleocene to early Eocene samples (Stenkul Fiord: US438, Lake Hazen: US261, Fosheim Anticline: US191) were subjected to are shown in Figure 12. The model simulates that following formation of carbonate samples at 2 °C during winter (at 56 Ma), they were steadily buried through time to a depth of approximately 3 km. This depth corresponds to a burial temperature of around 150 °C assuming a relatively consistent 50 °C/km geothermal gradient across both islands. In the model, it was assumed these samples experienced 10 million years of steady burial, 10 million years held at the maximum burial depth, 25 million years of gradual uplift, and then remained at the surface until the present. See Appendix A for the Late Paleocene and Early Eocene Sample Temperature Path that was used in the model calculations.

#### Middle Eocene Sample: US119

The middle Eocene carbonate sample (Buchanan Lake: US119) was not affected by the same regional burial history experienced by the late Paleocene to early Eocene samples, and formed during an interval of regional thrust faulting and uplift that brought on significant landform erosion and tectonic denudation (see Section 2.2.3 for information regarding depositional settings). Additionally, this sample formed in a syntectonic basin rapidly filling with rock detritus, and thus it would have experienced local burial beneath alluvium (Rickets & Stephenson, 1994). For the model, this sample was assumed to have experienced burial for 5

million years, held at maximum burial depth for 15 million years, followed by gradual uplift for 15 million years, and then remained in the near surface until the present. See Appendix A for the Middle Eocene Sample Temperature Path used for the model calculations.

#### **5.4.1.b. Reordering Model Output**

The model results indicate that Stenkul Fiord (US438)  $\Delta_{47}$  of 0.596‰ (63 °C) corresponds to a 157.5 °C maximum burial temperature, Lake Hazen (US261)  $\Delta_{47}$  of 0.621‰ (52 °C) corresponds to a 156 °C maximum burial temperature, and Fosheim Anticline W (US191)  $\Delta_{47}$  of 0.589‰ (67 °C) corresponds to a 158 °C maximum burial temperature. The change in clumped isotope value from formation to present are shown in Figure 13. Buchanan Lake (US119)  $\Delta_{47}$  of 0.604‰ (60 °C) corresponds to a 155 °C maximum burial temperature, see Figure 13. Micritic sample maximum burial temperatures are recorded in Table 4 under Reordering Temp °C. Uncertainty in the sample ages and the exact timing of regional burial and uplift events creates moderate burial temperature uncertainty. Adjustments to the burial timing (adjusting event 1 and event 2 by 5-30 million years) result in a  $\pm 4$  °C change in maximum burial temperature, while adjustments to the uplift timing (adjusting the length of event 3 and event 4 following the burial interval) results in a  $\pm 1$  °C change in maximum burial temperature. Using this model for other types of calcite material (e.g. Labile Spar) can also add uncertainty to burial temperature results, see Appendix A for additional plots.

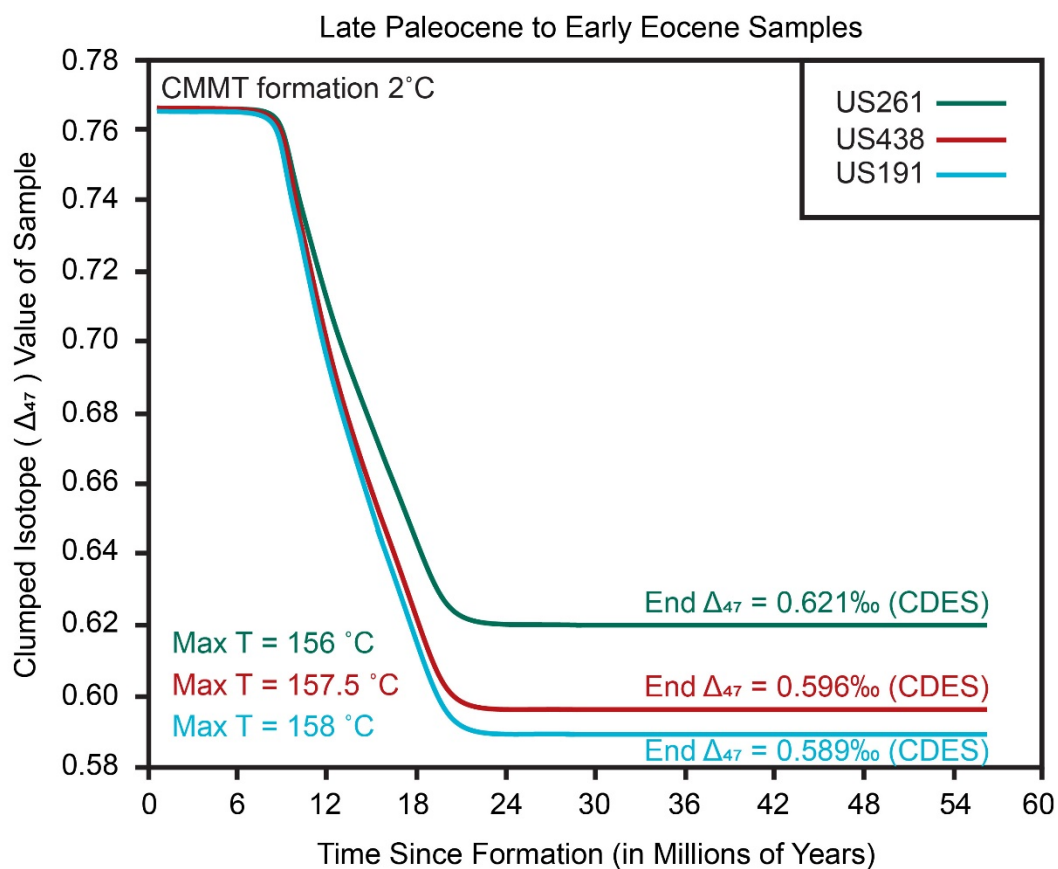


Figure 13a. Clumped Isotope Reordering Model for late Paleocene to early Eocene. US261: 0.589‰ in green, US438: 0.596‰ in red, US191: 0.589‰ in cyan. Heating a carbonate (formed at 2 °C = 0.7651‰) to a maximum burial temperature of 156°C results in a reordered  $\Delta_{47}$  value of 0.621‰, 157.5°C results in a reordered  $\Delta_{47}$  value of 0.596‰, and 158°C results in a reordered  $\Delta_{47}$  value of 0.589‰.

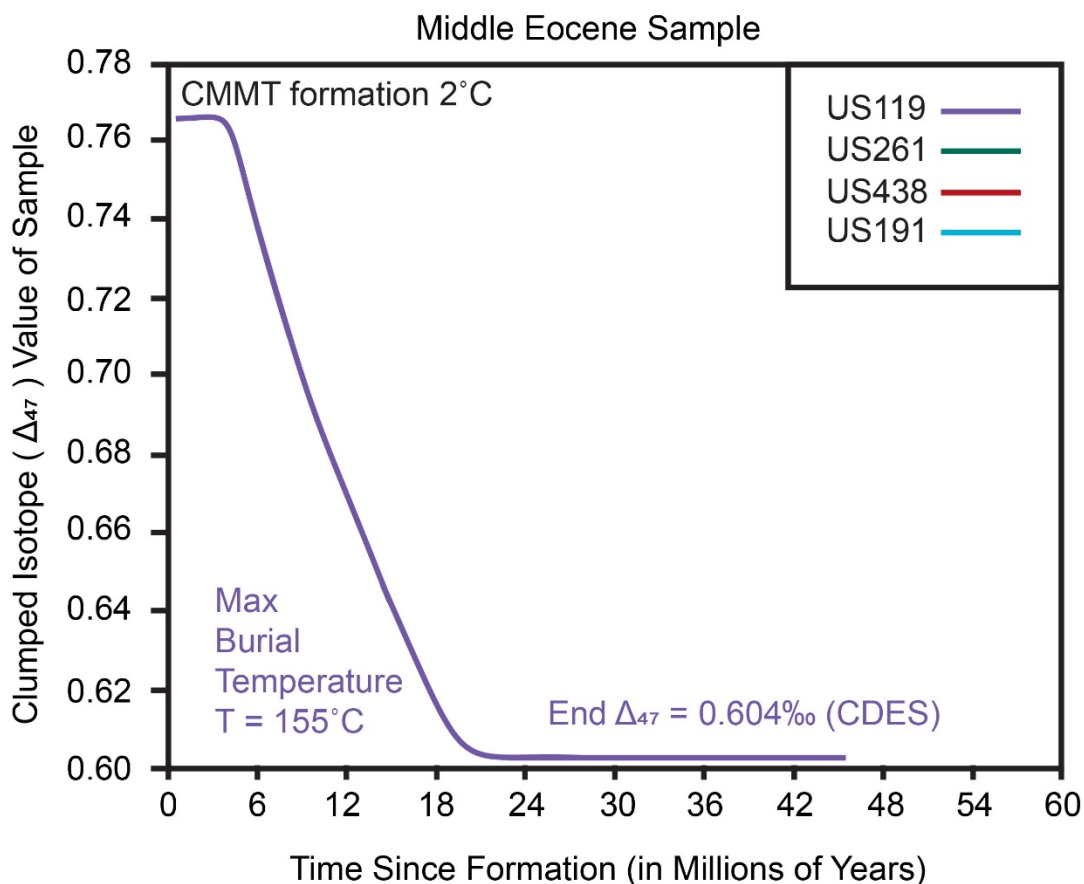


Figure 13b. Clumped Isotope Reordering Model for Middle Eocene. US119 in purple. Heating a carbonate (formed at 2 °C = 0.7651‰) to a maximum burial temperature of 155°C results in a reordered  $\Delta_{47}$  value of 0.604‰.

#### 5.4.2. Spar Formation Burial Temperatures

The Microspar and Sparry fabric types contain a mix of primary micrite (average micrite content: 35%, Table 1) and highly recrystallized spar. As a result, measured MSp and Spar clumped isotope temperatures are a mix of two end-members: the original micrite formation temperature (~2 °C) and the diagenetic spar formation temperatures (hot and unknown). The micrite may have also experienced varying degrees of reordering (as discussed in the previous section with samples US119, US261, US438, and US191); however, the degree of reordering in micrite is challenging to isolate due to the ubiquitous spar content within MSp and Spar samples.

Instead, by neglecting reordering influence and using the micrite formation temperature as the end member, a maximum estimate for the spar formation temperature can be obtained. Using the lower (2 °C) temperature provides the maximum burial temperatures for the Eureka Sound Group deposits, which can then be more realistically compared against the maximum temperatures calculated with the reordering model and the maximum temperature values from apatite fission track thermochronometry and vitrinite reflectance data (c.f., Huntington et al., 2011).

Using a two-component end-member mixing model, the weighted relative contributions of micrite and spar temperatures were weighted based on thin-section micrite and spar percentages. This model allowed for calculation of the unknown diagenetic spar formation temperatures for the MSp and Spar samples and obtain the remaining maximum burial temperatures, listed under Spar Formation °C in Table 4. Uncertainty in these model results is primarily due to potential reordering that may have occurred in the remaining micritic portion of the samples. Partial reordering (greater than half of remaining micrite) would cause 3-30 °C decreases in spar formation temperature based on the sample (18 °C average decrease). Running the mixing model with complete reordering of all remaining micrite (assuming the fully reordered micritic end-member has a 52 °C temperature) results in a 5-50 °C decrease in spar formation temperature based on the sample (30 °C average decrease in burial temperatures derived from the spar formation temperature end-member mixing model).

Calculated spar formation temperatures range from 104 to 171 °C. Five spar formation temperatures were calculated for the Fosheim Peninsula locality. At Fosheim Peninsula there are three sample locations with values of 170-171 °C and two locations with lower temperature values of 104 °C and 119 °C. The reordering temperature of 158 °C from the Fosheim Peninsula

agrees with the higher values. At the Stenkul Fiord locality, spar formation temperatures are 104 °C and 130 °C. Both spar formation estimates at Stenkul Fiord were lower temperatures than the reordering temperature approximation of 157.5 °C. At the Strathcona Fiord locality, there was one sparry sample and no reordering temperature for comparison. Strathcona Fiord had a spar formation temperature of 109 °C. Like Strathcona Fiord, Split Lake also only had one sparry sample present at the location. Split Lake had a spar formation temperature of 122 °C, a value that reasonably agrees with the temperatures at the geographically nearest locations, Strathcona Fiord and Stenkul Fiord. At the Axel Heiberg Island locality, there is a reordering temperature on the eastern side of the island at Buchanan Lake and one sparry sample on the western side of the island at Strand Fiord. Strand Fiord has a spar formation temperature of 132 °C, which is relatively consistent with the Axel Heiberg reordering temperature of 155 °C. Figure 14 compares maximum burial temperatures (from spar formation and reordering calculations) alongside relevant fault locations.

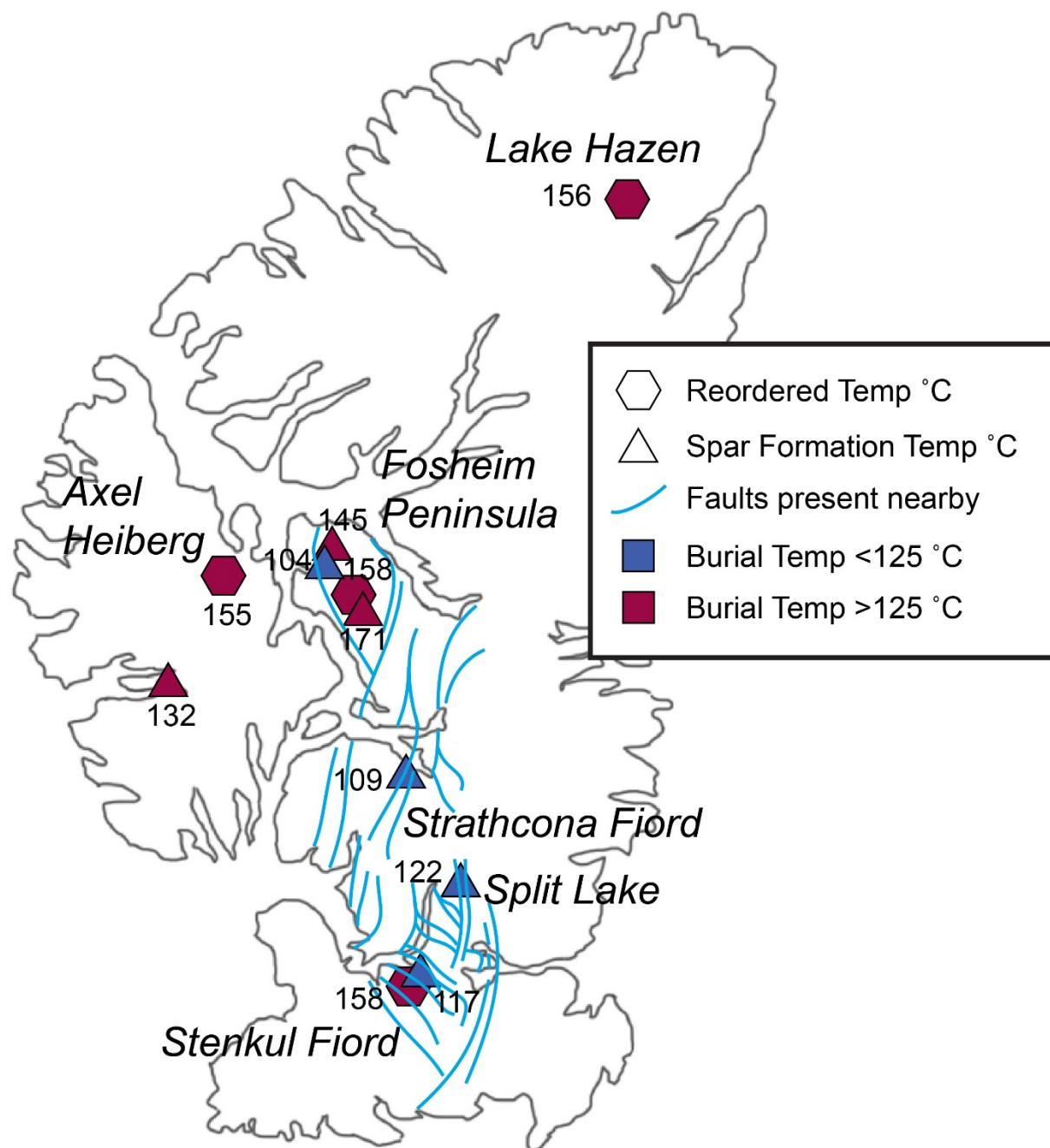


Figure 14. A spatial plot of calculated maximum burial temperatures. Sample locations with two spar formation temperatures were averaged for clarity. Faults nearby sample locations are shown on the map in light blue, and crosses over the hexagons and triangles if it cuts through the sample locations. Temperatures less than 125 °C are shown in dark blue, temperatures greater than 125 °C are shown in dark red. Fault locations are taken from Figure 40.1 in Harrison et al. (2011), and only relevant faults nearby sample locations are shown here.

Variations in spar replacement temperatures may reflect variations in fluid chemistry or sediment permeability (Huntington et al., 2011), or proximity to faults. Proximity to faults appears to be a dominant influence on variations in spar formation temperatures, with lower temperatures (104 – 122 °C) corresponding to locations with faults present (Figure 14). Previous work on Paleocene cooling (initiation around ~66 Ma) found the most significant cooling in samples from anticlines or hangingwalls of thrust faults, including the Fosheim Anticline and Lake Hazen fault system, and the Vesle Fiord thrust fault (Arne et al., 2002). Explanations for differential cooling across faults include differences in thermal conductivity and geothermal gradient of the rock units on each side of faults, local variations in heat flow from groundwater, and varying amounts of structural erosion (Arne et al., 2002). Faulting creates new fluid migration pathways along the fault zone, and stresses from faulting create joint networks and increase permeability, allowing meteoric waters to move further down into the subsurface. Rather than the calcite crystallizing out of solely hot diagenetic fluids, faults allow cooler surface waters to mix with those fluids, which results in lower  $\Delta_{47}$  temperatures for samples formed in fault locations (e.g., Hodson et al., 2016). Variations in spar  $\Delta_{47}$  temperatures correspond with fault locations and can be explained by faulting, reducing the temperature gradient, and allowing cooler fluids to migrate into deeper rock units, causing crystallized spar to have cooler  $\Delta_{47}$  temperatures relative to other samples from the same general location (e.g., Fosheim Peninsula).

Table 4. Table of calculated burial temperatures.

Spar formation temperatures (Spar Formation °C) were derived by using a micrite and diagenetic spar two-component end-member mixing model. Reordering temperatures (Reordering Temp °C) were derived by using a model of the predictable clumped isotope reordering rate associated with prolonged burial heating. Both “Spar Formation” and “Reordering Temp” provide a burial temperature for heated Eureka Sound Group deposits.

Sample	Age	Location	Fabric	T( $\Delta_{47}$ ) °C	Spar Formation °C	Reordering Temp °C
US422	LP - EE	Strathcona	Spar	77.4	109	--
US444	LP - EE	Split	Spar	62.2	122	--
US436	LP - EE	Stenkul	Spar	94.2	104	--
US176	LP - EE	Strand	Spar	105.6	132	--
US111	LP - EE	Fosh Ant W	MSp	86.0	170	--
US251	LP - EE	Fosh Ant E	MSp	120.6	171	--
US108	LP - EE	Hot Weather	MSp	84.2	119	--
US107	LP - EE	Hot Weather	MSp	102.5	170	--
US196	LP - EE	Mosquito	MSp	52.9	104	--
US435	LP - EE	Stenkul	MSp	79.0	130	--
US119	MID E	Buchanan	Mic/MSp	59.6	--	155
US438	LP - EE	Stenkul	Mic/MSp	63.2	--	157.5
US261	LP - EE	Hazen	Mic	51.6	--	156
US191	LP - EE	Fosh Ant W	Mic	66.8	--	158

### 5.4.3. Comparing $\Delta_{47}$ Burial Temperatures to Past Thermal Reconstructions

Previous burial temperature studies have been conducted in the Sverdrup Basin to approximate the paleogeothermal gradients and reconstruct thermal maturity for hydrocarbon assessment. Dewing & Sanei (2009) evaluated vitrinite reflectance and Rock-Eval Tmax data from the Canadian Arctic in order to provide estimates of maximum temperature experienced by these rock layers. As organic-rich rocks are buried, they are exposed to higher temperatures, and their vitrinite reflectance values increase (Dewing & Sanei, 2009). Arne et al. (2002) reconstructed the thermal history of Axel Heiberg and Ellesmere Islands using vitrinite reflectance data ( $R_0$ ) and apatite fission track thermochronometry. The total fission-track annealing depth (corresponds to  $R_0 \sim 0.8\%$  and  $\sim 125$  °C) was reconstructed across different locations on the two islands. At some locations, such as northwestern Ellesmere Island and the

lower part of Fosheim Peninsula, units were annealed near or at the surface, while in other central areas, units were annealed at depths of around 2 km (Arne et al., 2002). This pattern suggests significant heating of units, even younger stratigraphy near the surface, and spatial variability of heating. Additionally, the northeastern Arctic Islands have multiple igneous intrusions as a result of Cretaceous volcanism, which has caused anomalously high thermal maturity values in other studies (Dewing & Sanei, 2009). This is especially noticeable in the Jurassic strata and layers currently at depths greater than 2km; however, the Eureka Sound layers likely were deposited late enough to avoid the influence of igneous intrusions on regional geothermal flux.

Clumped isotope analysis of diagenetic and reordered calcite is an additional method to reconstruct sedimentary basin diagenetic temperatures and can be paired with vitrinite reflectance or apatite fission track thermochronometry (Huntington et al., 2011). Data from previous vitrinite reflectance studies generally show high thermal maturity at the base of the Eureka Sound Group in SW Axel Heiberg and central Ellesmere Island. These studies also show significant variability in thermal maturity (with a combination of high and moderate temperatures) across the Fosheim Peninsula (e.g., Bustin, 1986; Stewart et al., 1992). This data agrees well with the clumped isotope results, particularly at Fosheim Peninsula, where the hottest and coldest temperatures coexist. Vitrinite-derived maximum temperatures for well samples (before Tertiary cooling, approximate timeframe of late Cretaceous to early Eocene) also agree reasonably with clumped isotope burial temperatures, see Figure 15 (c.f., Arne et al., 2002). A spatial evaluation of burial temperatures indicates that the hottest vitrinite-derived and clumped isotope-derived temperatures are inferred for Axel Heiberg and central Ellesmere Island, and the lower burial temperatures are in the southern part of Ellesmere Island. Stenkul Fiord temperature

variation may be due to smaller faults present at the locality as well as differential amounts of burial and alteration based on the different specific sample ages.

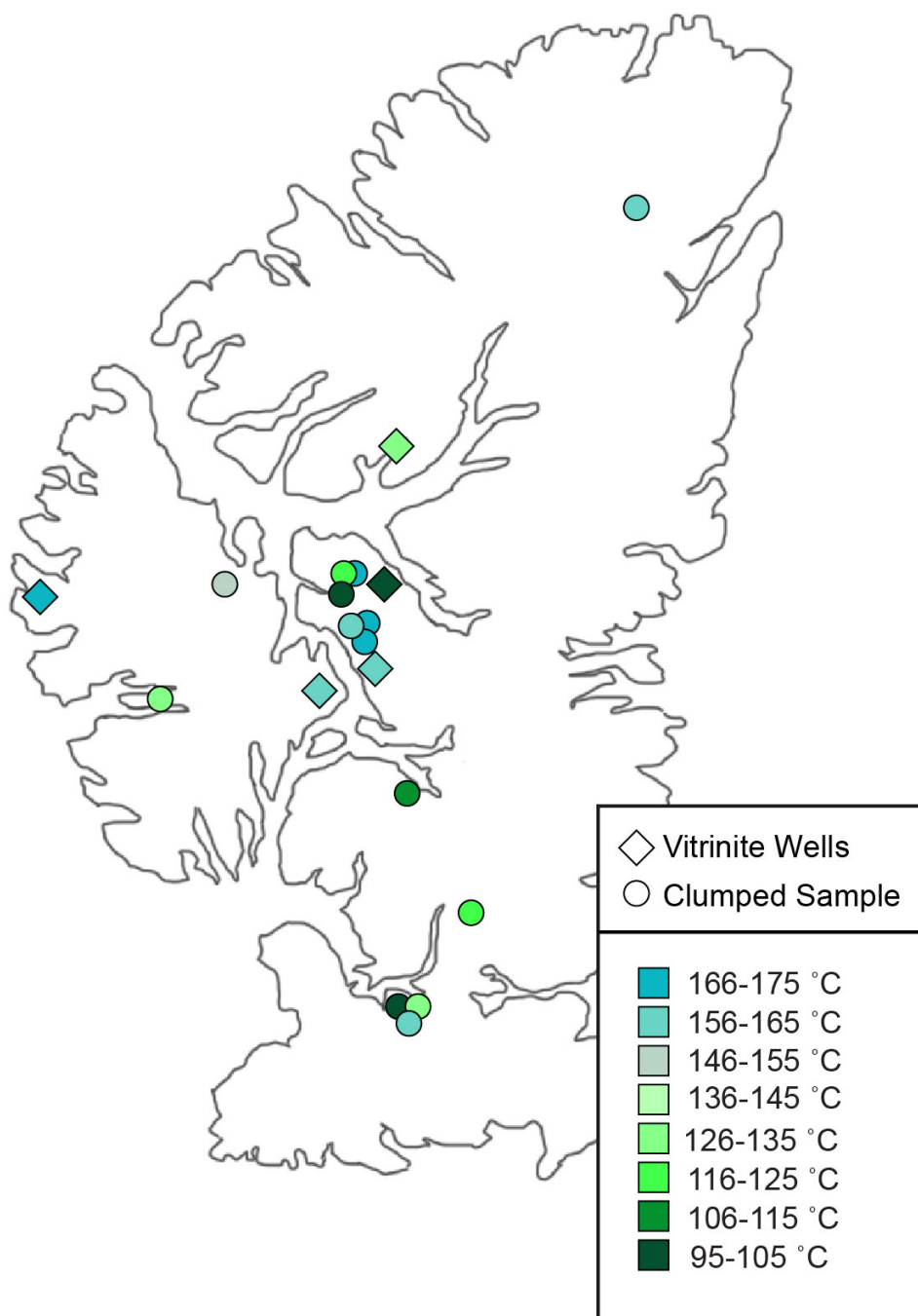


Figure 15. Maximum burial temperatures plotted with vitrinite reflectance temperatures. Clumped isotope burial temperature approximations (in °C) for the Eureka Sound Group (approximated from reordering and diagenetic spar formation temperatures) plotted alongside Arne et al. (2002) vitrinite maximum temperature approximations prior to cooling.

On Fosheim Peninsula, the clumped isotope burial temperature ranges (HW = 145 °C, Mos = 104 °C, FAE = 171 °C, FAW = 170 °C; -30 °C uncertainty) are within the vitrinite temperature ranges described in Arne et al. (2002) for wells Neil O-15 (greater than 120 °C), Taleman J-34 (80-105 °C); Fosheim N-27 (130-185 °C); and Depot Point L-24 (140-175 °C), see Figure 16. Clumped isotope burial temperatures across Fosheim Peninsula are 10 to 25 °C greater than the average value for the vitrinite-derived maximum temperature ranges for similar Fosheim Peninsula locations, see Figure 17. This is likely due to the spar formation model ignoring potential reordering influence within micrite (if micrite is completely reordered, spar formation temperatures decrease by an average of 30 °C). Clumped isotope estimates from surface outcrops yielded temperature approximations that aligned reasonably well with vitrinite studies that required subsurface drilling. Clumped isotope and vitrinite temperature estimates for the Eureka Sound Group deposits agree within their respective uncertainty ranges. Both methods are likely effective techniques to estimate both burial temperatures and depths within the context of sedimentary basin analysis.

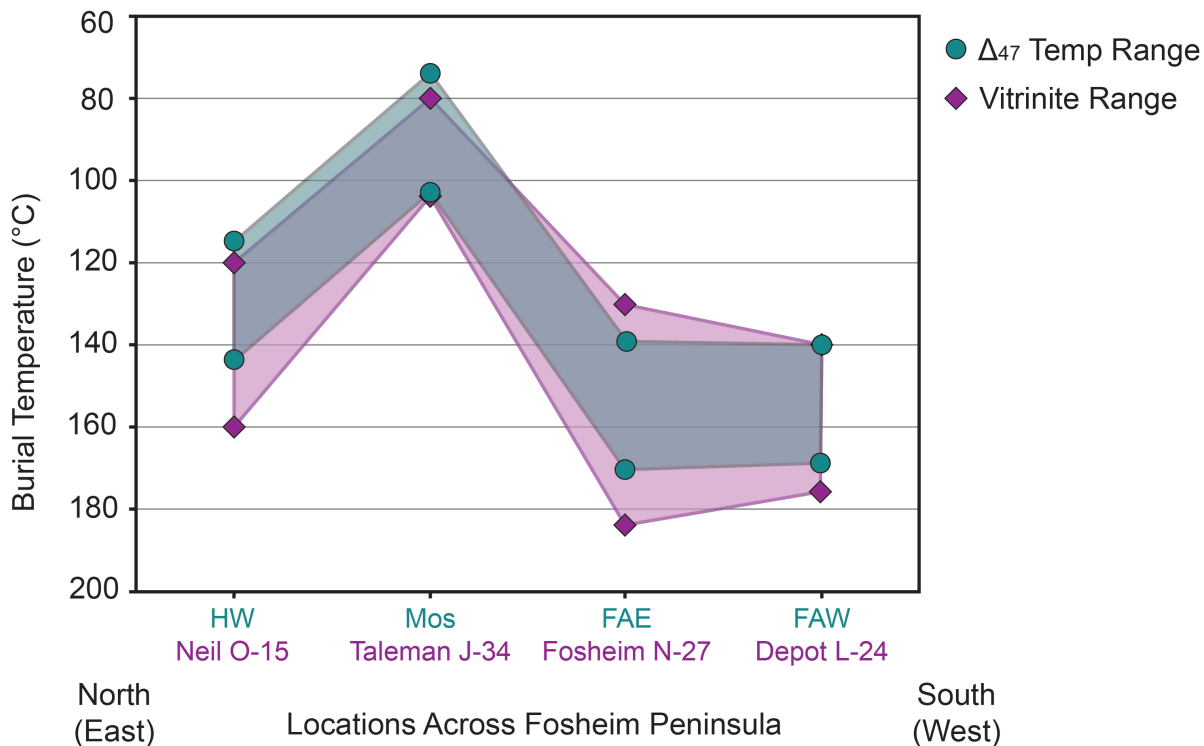


Figure 16.  $\Delta_{47}$  burial temperature ranges and vitrinite-derived maximum burial temperature ranges across Fosheim Peninsula. On a north to south transect across Fosheim Peninsula, the vitrinite wells (purple diamonds) are Neil O-15 (immediately North of Fosheim Peninsula), Taleman J-34 (upper middle Fosheim Peninsula); Fosheim N-27 (lower middle Fosheim Peninsula); and Depot Point L-24 (immediately South of Fosheim Peninsula), vitrinite data from Arne et al. (2002). From north to south, the clumped isotope samples (teal circles) compared were Hot Weather Creek (HW; 145 °C), Mosquito Creek (Mos; 104 °C), Fosheim Anticline East (FAE; 171 °C), and Fosheim Anticline West (FAW; 170 °C). Clumped range includes model uncertainty.

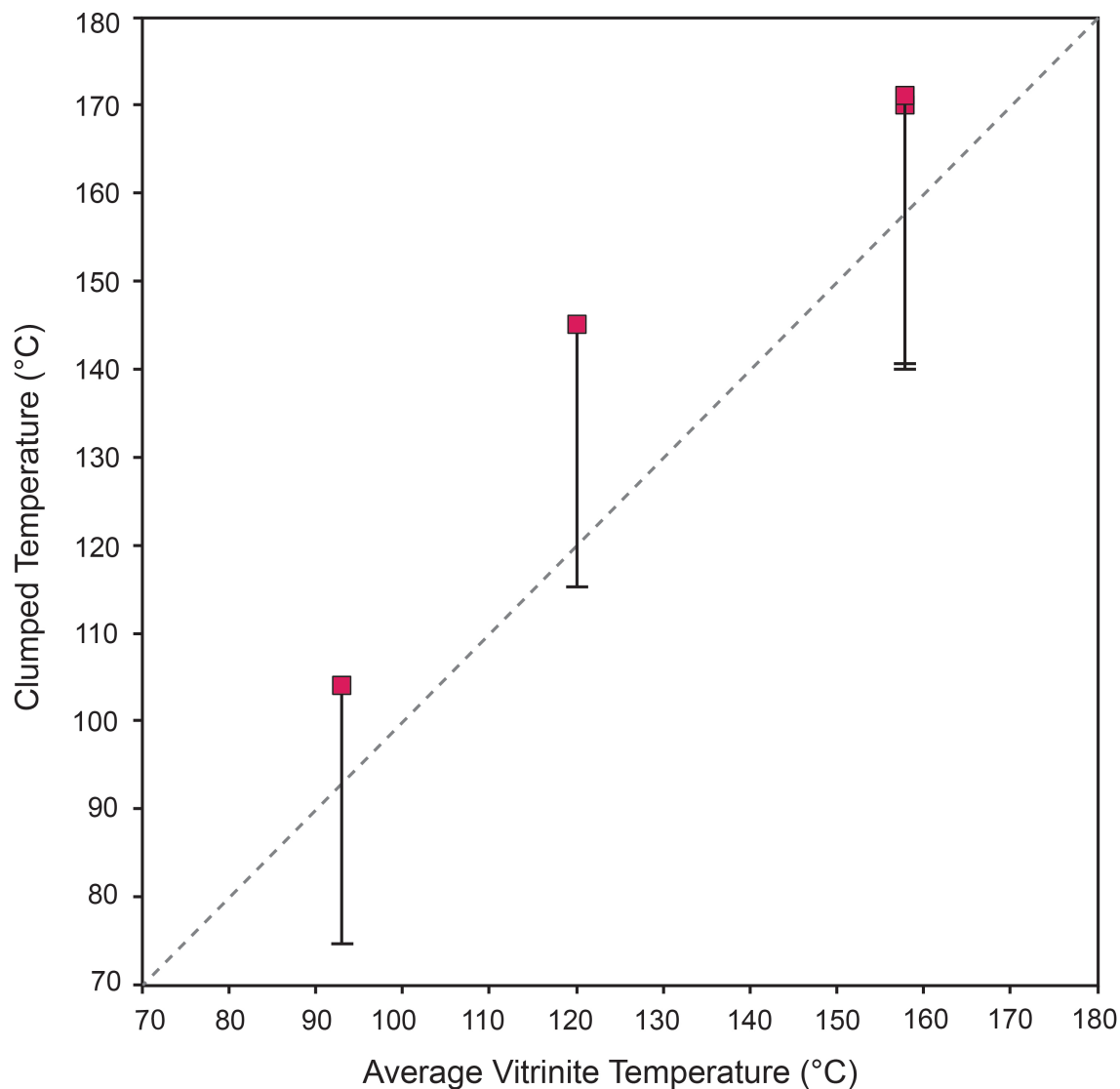


Figure 17. Crossplot of vitrinite burial temperature averages by  $\Delta_{47}$  burial temperatures for Fosheim Peninsula. Vitrinite wells are Neil O-15 (~120 °C), Taleman J-34 (~93 °C); Fosheim N-27 (~158 °C); and Depot Point L-24 (~158 °C), vitrinite data from Arne et al. (2002). Compared clumped isotope samples were Hot Weather Creek (HW; 145 °C), Mosquito Creek (Mos; 104 °C), Fosheim Anticline East (FAE; 171 °C), and Fosheim Anticline West (FAW; 170 °C). Error bars shows the -30 °C uncertainty of the spar formation model results.

#### 5.4.4. Basin Dynamics and Cooling History

The deposition of the ESG samples was followed by burial and substantial deformation from thrusting and folding in the eastern portion of the Sverdrup Basin through the Paleocene and Eocene (Embry & Beauchamp, 2008). Regional cooling patterns suggest that deposits located near major structures experienced more significant cooling during deformation, particularly in thrust fault hangingwalls and at locations like Fosheim Anticline (e.g., Arne et al., 2002). The  $\Delta_{47}$  temperature data suggests that following formation and burial of the carbonate samples, thrusting events and the tectonic inversion of the basin promoted greater denudation to overlying stratigraphy, which encouraged cooling of the deposits (e.g., Arne et al., 2002). The lowest temperatures for Microspar and Sparry samples correspond to near-fault locations (US444: Split Lake, US108: Hot Weather Creek, US435: Stenkul Fiord, US111: Fosheim Anticline W, US422: Strathcona Fiord, US196: Mosquito Creek). Fault-induced fracture networks likely allowed for enhanced surface fluid migration into the subsurface, further promoting cooling and resulting in crystallized spar with lower  $\Delta_{47}$  temperatures (e.g., Hodson et al., 2016). Following the climax of deformation in the late Eocene, the Sverdrup Basin experienced additional uplift, returning the rocks containing the studied samples to the surface and halting deposition for the entire basin (Embry & Beauchamp, 2008).

## 6. CONCLUSIONS

### 6.1. Data Summary

The isotopic ( $\delta^{13}\text{C}$ ,  $\delta^{18}\text{O}$ ,  $\Delta_{47}$ ) analyses of palustrine carbonates from Axel Heiberg and Ellesmere Islands expand on existing stratigraphic, paleontological, and thermal investigations of the Sverdrup Basin.  $\delta^{13}\text{C}$  isotope values range from -4.6 to +12.3‰ (VPDB), with carbon averages of 9.8‰ (Mic), 4.5‰ (Mic/MSp), 3.4‰ (MSp), 2.0‰ (Spar).  $\delta^{18}\text{O}$  isotope values range from -23.1 to -15.2‰ (VPDB), with oxygen averages of -17.2‰ (Mic), -17.8‰ (Mic/MSp), -18.0‰ (MSp), -18.9‰ (Spar). Carbon and oxygen stable isotope averages decrease with greater visual evidence of diagenetic alteration. Clumped ( $\Delta_{47}$ ) values were 0.505 to 0.621‰ (CDES), corresponding to temperatures of 52 to 121 °C, and modeled Eureka Sound Group burial temperatures spanned 104 to 171 °C. Isotopic values and carbonate fabrics indicate solid-state reordering during burial heating and diagenetic recrystallization of multiple samples.

### 6.2. Concluding Overarching Research Questions

Question 1: *Is it possible to use the isotope geochemistry of rocks that have undergone burial and partial deformation to obtain reliable paleoclimate proxy data?*

It is possible to obtain useful paleoclimate information using isotope geochemistry on altered rocks. Stable isotopes, which are less sensitive to burial diagenesis than clumped isotopes, can still provide useful information about late Paleocene to middle Eocene precipitation in less-altered primary samples (Mic and Mic/MSp). Additionally, stable isotope composition of MSp and Spar samples can provide information about the composition of diagenetic fluids, as both stable isotope values decrease with increased diagenetic burial alteration. Decreases in  $\delta^{13}\text{C}$  composition display the switch from atmospheric  $\text{CO}_2$  composition influencing the  $\delta^{13}\text{C}$  in

primary micrite, to an influx of inorganic carbon sourced from burial fluids in the secondary spar.  $\delta^{18}\text{O}$  in primary micrite is consistent with other regional approximations of environmental water, and decreases are due to the temperature-dependent fractionation between calcite spar and hot burial fluids. Unlike the stable isotope record, sensitive clumped isotopes do not record surface temperature information, even in primary samples (Mic and Mic/MSp). Instead,  $\Delta_{47}$  values can be applied in models to obtain Eureka Sound Group burial temperatures that expand our understanding of the region's diagenetic history.

*Question 2: What does the stable isotope data suggest about the climate on Ellesmere and Axel Heiberg Islands during the late Paleocene and early Eocene Epochs?*

This study provides insight into precipitation conditions from the late Paleocene to middle Eocene (approximately 59 to 45 Ma), adds to the currently limited data on polar terrestrial regions, and contributes to studies attempting to reconstruct latitudinal climate gradients from greenhouse periods. The oxygen isotope values obtained in this study are consistent with regional environmental water  $\delta^{18}\text{O}$  estimates, and carbon isotope values for micritic samples are significantly enriched. This isotopic data indicates that the samples were enriched through the dissolution-precipitation enrichment mechanism, with significant water influx from summer rain and exclusively winter carbonate precipitation. Repeated dissolution-precipitation cycles along lake margins adequately explain the high carbon enrichment within the primary samples. Micrite in the analyzed samples built up along lake margins with seasonal sub-aerial exposure, and thus having dissolution-precipitation enrichment aligns with knowledge of the samples' depositional environments. This exposure history makes atmospheric  $\text{CO}_2$  the primary influence on the  $\delta^{13}\text{C}$  composition, and it strongly suggests Arctic monsoonal conditions

sometime during the late Paleocene to middle Eocene. The findings of this study support paleontological estimates of high summer rainfall, but also support the controversial Arctic monsoonal climate hypothesis by suggesting dry winters. As a result, it is necessary for future work to analyze a well-dated and precisely mapped section of Arctic samples at multiple intervals through the stratigraphic section, to obtain a high-resolution record of precipitation changes through time.

*Question 3: Is it possible to apply clumped isotope temperature data in models to derive burial temperatures and geologic information about the Sverdrup Basin?*

The studied samples preserve the diagenetic history of events associated with the Eureka Orogeny. Eocene regional burial and uplift events are observed within the Sverdrup Basin samples across both Axel Heiberg Island and Ellesmere Island. The burial signal is preserved by hot and reordereed temperatures (visible in primary samples), and burial and uplift events were modeled to obtain reordering maximum burial temperatures. Spar formation temperatures reflect similarly high burial temperatures, but also display variations in cooling between locations. Rock fracture and joint networks facilitated the migration of cooler surface fluids into the subsurface, resulting in lower  $\Delta_{47}$  temperature for Microspar and Sparry samples near faults. Lower burial temperatures are associated with faults and large-scale structural denudation following tectonic inversion of the Sverdrup Basin, which agrees with other regional thermal studies.

Previous thermal history investigations of the Sverdrup Basin have been conducted for oil and gas prospecting, as thermal maturity is used to approximate the hydrocarbon potential of source rock. In this study, clumped isotope values were used to obtain burial temperatures for Eureka Sound Group deposits and increase understanding of tectonic events occurring in the

Sverdrup Basin.  $\Delta_{47}$  -derived maximum burial temperatures reasonably agree with vitrinite derived maximum temperatures for Tertiary-aged well samples and patterns of high and low thermal maturity in other investigations (e.g., Arne et al., 2002; Bustin, 1986; Stewart et al 1992; Dewing & Sanei, 2009). Therefore, clumped isotope temperature examinations may provide an effective thermal maturity method for remote and unexplored locations that could potentially complement apatite fission track thermochronometry and vitrinite reflectance studies.

## REFERENCES

1. Alonso-Zarza, A. M., Dorado-Valiño, M., Valdeolmillos-Rodríguez, A., & Ruiz-Zapata, M. B. (2006). A recent analogue for palustrine carbonate environments: The Quaternary deposits of las Tablas de Daimiel wetlands, Ciudad Real, Spain. *Geological Society of America Special Papers*, 416, 153.
2. Alonso Zarza, A. M., Calvo, J. P., & García del Cura, M. A. (1992). Palustrine sedimentation and associated features---grainification and pseudo-microkarst---in the Middle Miocene (intermediate unit) of the Madrid Basin, Spain. *Sedimentary Geology*, 76, 43-61.
3. Alonso-Zarza, A. M. (2003). Palaeoenvironmental significance of palustrine carbonates and calcretes in the geological record. *Earth Science Reviews*, 60(3), 261-298.
4. Andrews, J. E., Riding, R., & Dennis, P. F. (1997). The stable isotope record of environmental and climatic signals in modern terrestrial microbial carbonates from Europe. *Palaeogeography, Palaeoclimatology, Palaeoecology*, 129(1-2), 171-189.
5. Arne, D. C., Grist, A. M., Zentilli, M., Collins, M., Embry, A., & Gentzis, T. (2002). Cooling of the Sverdrup Basin during Tertiary basin inversion: implications for hydrocarbon exploration. *Basin Research*, 14(2), 183-205.
6. Basinger, J. F., Greenwood, D. R., & Sweda, T. (1994). Early Tertiary vegetation of Arctic Canada and its relevance to paleoclimatic interpretation. *Cenozoic plants and climates of the Arctic* (pp. 175-198). Springer, Berlin, Heidelberg.
7. Bernasconi, S. M., & McKenzie, J. A. (2007). Lake sediments. *Encyclopedia of quaternary science*, 351-359.
8. Bernasconi, S. M., Müller, I. A., Bergmann, K. D., Breitenbach, S. F., Fernandez, A., Hodell, D. A., ... & Ziegler, M. (2018). Reducing uncertainties in carbonate clumped isotope analysis through consistent carbonate  $\delta^{13}\text{C}$ -based standardization. *Geochemistry, Geophysics, Geosystems*, 19(9), 2895-2914.
9. Bottinga, Y. (1968). Calculation of fractionation factors for carbon and oxygen isotopic exchange in the system calcite-carbon dioxide-water. *The Journal of Physical Chemistry*, 72(3), 800-808.
10. Bowen, G. J. (2010). Isoscapes: spatial pattern in isotopic biogeochemistry. *Annual Review of Earth and Planetary Sciences*, 38, 161-187.
11. Brand, W. A., Assonov, S. S., & Coplen, T. B. (2010). Correction for the  $^{17}\text{O}$  interference in  $\delta(^{13}\text{C})$  measurements when analyzing  $\text{CO}_2$  with stable isotope mass spectrometry (IUPAC Technical Report). *Pure and Applied Chemistry*, 82(8), 1719-1733.

12. Breecker, D. O., Sharp, Z. D., & McFadden, L. D. (2009). Seasonal bias in the formation and stable isotopic composition of pedogenic carbonate in modern soils from central New Mexico, USA. *Geological Society of America Bulletin*, 121(3-4), 630-640.
13. Bristow, T. F., Bonifacie, M., Derkowski, A., Eiler, J. M., & Grotzinger, J. P. (2011). A hydrothermal origin for isotopically anomalous cap dolostone cements from south China. *Nature*, 474(7349), 68-71.
14. Burgener, L., Huntington, K. W., Hoke, G. D., Schauer, A., Ringham, M. C., Latorre, C., & Díaz, F. P. (2016). Variations in soil carbonate formation and seasonal bias over > 4 km of relief in the western Andes (30 S) revealed by clumped isotope thermometry. *Earth and Planetary Science Letters*, 441, 188-199.
15. Burgener, L. K., Huntington, K. W., Sletten, R., Watkins, J. M., Quade, J., & Hallet, B. (2018). Clumped isotope constraints on equilibrium carbonate formation and kinetic isotope effects in freezing soils. *Geochimica et Cosmochimica Acta*, 235, 402-430.
16. Bustin, R. M., Ross, J. V., & Moffat, I. (1986). Vitrinite anisotropy under differential stress and high confining pressure and temperature: preliminary observations. *International Journal of Coal Geology*, 6(4), 343-351.
17. CAVM Team. 2003. Circumpolar Arctic Vegetation Map. (1:7,500,000 scale), Conservation of Arctic Flora and Fauna (CAFF) Map No. 1. U.S. Fish and Wildlife Service, Anchorage, Alaska.
18. Cerling, T. E., & Quade, J. (1993). Climate change in continental isotopic records. *Geophysical Monograph*, 78, 217-231.
19. Clark, I. D., & Lauriol, B. (1992). Kinetic enrichment of stable isotopes in cryogenic calcites. *Chemical Geology*, 102(1-4), 217-228.
20. Courty, M. A., Marlin, C., Dever, L., Tremblay, P., & Vachier, P. (1994). The properties, genesis and environmental significance of calcitic pendants from the High Arctic (Spitsbergen). *Geoderma*, 61(1-2), 71-102.
21. Daëron, M., Blamart, D., Peral, M., & Affek, H. P. (2016). Absolute isotopic abundance ratios and the accuracy of  $\Delta 47$  measurements. *Chemical Geology*, 442, 83-96.
22. Dansgaard, W. (1964). Stable isotopes in precipitation. *Tellus*, 16(4), 436-468.
23. Defliese, W. F., Hren, M. T., & Lohmann, K. C. (2015). Compositional and temperature effects of phosphoric acid fractionation on  $\Delta 47$  analysis and implications for discrepant calibrations. *Chemical Geology*, 396, 51-60.
24. Dennis, K. J., Affek, H. P., Passey, B. H., Schrag, D. P., & Eiler, J. M. (2011). Defining an absolute reference frame for 'clumped' isotope studies of CO<sub>2</sub>. *Geochimica et Cosmochimica Acta*, 75(22), 7117-7131.

25. Dewing, K., & Obermajer, M. (2011). Thermal maturity of the Sverdrup Basin, Arctic Canada and its bearing on hydrocarbon potential. *Geological Society, London, Memoirs*, 35(1), 567-580.
26. Dewing, K., & Sanei, H. (2009). Analysis of large thermal maturity datasets: Examples from the Canadian Arctic Islands. *International Journal of Coal Geology*, 77(3-4), 436-448.
27. Diffenbaugh, N. S., & Field, C. B. (2013). Changes in ecologically critical terrestrial climate conditions. *Science*, 341(6145), 486-492.
28. Driese, S. G., & Mora, C. I. (1993). Physico-chemical environment of pedogenic carbonate formation in Devonian vertic palaeosols, central Appalachians, USA. *Sedimentology*, 40(2), 199-216.
29. Dunagan, S. P., & Turner, C. E. (2004). Regional paleohydrologic and paleoclimatic settings of wetland/lacustrine depositional systems in the Morrison Formation (Upper Jurassic), Western Interior, USA. *Sedimentary Geology*, 167(3-4), 269-296.
30. Eberle, J. J., & Eberth, D. A. (2015). Additions to the Eocene Perissodactyla of the Margaret Formation, Eureka Sound Group, Ellesmere Island, Arctic Canada. *Canadian Journal of Earth Sciences*, 52(2), 123-133.
31. Eberle, J. J., & Greenwood, D. R. (2012). Life at the top of the greenhouse Eocene world—A review of the Eocene flora and vertebrate fauna from Canada's High Arctic. *Bulletin*, 124(1-2), 3-23.
32. Eberle, J. J., Fricke, H. C., Humphrey, J. D., Hackett, L., Newbrey, M. G., & Hutchison, J. H. (2010). Seasonal variability in Arctic temperatures during early Eocene time. *Earth and Planetary Science Letters*, 296(3-4), 481-486.
33. Eberle, J. J., Gottfried, M. D., Hutchison, J. H., & Brochu, C. A. (2014). First record of Eocene bony fishes and crocodyliforms from Canada's Western Arctic. *PloS one*, 9(5).
34. Eiler, J. M. (2007). "Clumped-isotope" geochemistry—The study of naturally-occurring, multiply-substituted isotopologues. *Earth and planetary science letters*, 262(3-4), 309-327.
35. Eiler, J. M. (2011). Paleoclimate reconstruction using carbonate clumped isotope thermometry. *Quaternary Science Reviews*, 30(25-26), 3575-3588.
36. Eldrett, J. S., Greenwood, D. R., Harding, I. C., & Huber, M. (2009). Increased seasonality through the Eocene to Oligocene transition in northern high latitudes. *Nature*, 459(7249), 969-973.
37. Eldrett, J. S., Greenwood, D. R., Polling, M., Brinkhuis, H., & Sluijs, A. (2014). A seasonality trigger for carbon injection at the Paleocene–Eocene Thermal Maximum. *Climate of the Past*, 10(2), 759-769.

38. Embry, A., & Beauchamp, B. (2008). Sverdrup basin. *Sedimentary basins of the world*, 5, 451-471.
39. Estes, R., & Hutchison, J. H. (1980). Eocene lower vertebrates from Ellesmere Island, Canadian arctic archipelago. *Palaeogeography, Palaeoclimatology, Palaeoecology*, 30, 325-347.
40. Ferry, J. M., Passey, B. H., Vasconcelos, C., & Eiler, J. M. (2011). Formation of dolomite at 40–80° C in the Latemar carbonate buildup, Dolomites, Italy, from clumped isotope thermometry. *Geology*, 39(6), 571-574.
41. Flügel, E. (2010). Diagenesis, porosity, and dolomitization. (pp. 267-338). Berlin, Heidelberg: Springer Berlin Heidelberg.
42. Freytet, P., Plaziat, J.C., 1982. Continental carbonate sedimentation and pedogenesis—Late Cretaceous and early Tertiary of southern France. *Contributions to Sedimentology* 12, 213 pp.
43. Freytet, P. (1973). Petrography and paleo-environment of continental carbonate deposits with particular reference to the Upper Cretaceous and Lower Eocene of Languedoc (Southern France). *Sedimentary Geology*, 10(1), 25-60.
44. Freytet, P. (1984). Carbonate lacustrine sediments and their transformations by emersion and pedogenesis: importance of identifying them for paleogeographical reconstructions. *Bull. Cent. Res. Explor. Prod. Elf-Aquit*, 8, 223-247.
45. Galeotti, S., Krishnan, S., Pagani, M., Lanci, L., Gaudio, A., Zachos, J. C., ... Lourens, L. (2010). Orbital chronology of early Eocene hyperthermals from the Contessa Road section, Central Italy. *Earth and Planetary Science Letters*, 290(1), 192-200.
46. Gallagher, T. M., & Sheldon, N. D. (2016). Combining soil water balance and clumped isotopes to understand the nature and timing of pedogenic carbonate formation. *Chemical Geology*, 435, 79-91.
47. Ghosh, P., Adkins, J., Affek, H., Balta, B., Guo, W., Schauble, E. A., ... & Eiler, J. M. (2006).  $^{13}\text{C}$ – $^{18}\text{O}$  bonds in carbonate minerals: a new kind of paleothermometer. *Geochimica et Cosmochimica Acta*, 70(6), 1439-1456.
48. Gion, A. M., Williams, S. E., & Müller, R. D. (2017). A reconstruction of the Eureka Orogeny incorporating deformation constraints. *Tectonics*, 36(2), 304-320.
49. Gould, W. A., Reynolds, M., & Walker, D. A. (2003). Vegetation, plant biomass, and net primary productivity patterns in the Canadian Arctic. *Journal of Geophysical Research - Atmospheres*, 108(D2).
50. Grasby, S. E., & Beauchamp, B. (2008). Intrabasin variability of the carbon-isotope record across the Permian–Triassic transition, Sverdrup Basin, Arctic Canada. *Chemical Geology*, 253(3), 141-150.

51. Greenwood, D. R., & Wing, S. L. (1995). Eocene continental climates and latitudinal temperature gradients. *Geology*, 23(11), 1044-1048.
52. Greenwood, D. R., Basinger, J. F., & Smith, R. Y. (2010). How wet was the Arctic Eocene rain forest? Estimates of precipitation from Paleogene Arctic macrofloras. *Geology*, 38(1), 15-18.
53. Guemas, V., Doblas-Reyes, F. J., Andreu-Burillo, I., & Asif, M. (2013). Retrospective prediction of the global warming slowdown in the past decade. *Nature Climate Change*, 3(7), 649-653.
54. Guo, W., & Eiler, J. M. (2007). Temperatures of aqueous alteration and evidence for methane generation on the parent bodies of the CM chondrites. *Geochimica et Cosmochimica Acta*, 71(22), 5565-5575.
55. Gutjahr, M., Ridgwell, A., Sexton, P. F., Anagnostou, E., Pearson, P. N., Pälike, H., ... & Foster, G. L. (2017). Very large release of mostly volcanic carbon during the Palaeocene–Eocene Thermal Maximum. *Nature*, 548(7669), 573-577.
56. Harrison, J. C., Mayr, U., McNeil, D. H., Sweet, A. R., McIntyre, D. J., Eberle, J. J., ... & Nohr-Hansen, H. (1999). Correlation of Cenozoic sequences of the Canadian Arctic region and Greenland; implications for the tectonic history of northern North America. *Bulletin of Canadian Petroleum Geology*, 47(3), 223-254.
57. Harrison, J. C., Brent, T. A., & Oakey, G. N. (2011). Baffin Fan and its inverted rift system of Arctic eastern Canada: Stratigraphy, tectonics and petroleum resource potential. *Geological Society, London, Memoirs*, 35(1), 595-626.
58. Henkes, G. A., Passey, B. H., Grossman, E. L., Shenton, B. J., Pérez-Huerta, A., & Yancey, T. E. (2014). Temperature limits for preservation of primary calcite clumped isotope paleotemperatures. *Geochimica et Cosmochimica Acta*, 139, 362-382.
59. Hodson, K. R., Crider, J. G., & Huntington, K. W. (2016). Temperature and composition of carbonate cements record early structural control on cementation in a nascent deformation band fault zone: Moab Fault, Utah, USA. *Tectonophysics*, 690, 240-252.
60. Hollander, D. J., & McKenzie, J. A. (1991). CO<sub>2</sub> control on carbon-isotope fractionation during aqueous photosynthesis: A paleo-pCO<sub>2</sub> barometer. *Geology*, 19(9), 929-932.
61. Huber, M., & Goldner, A. (2012). Eocene monsoons. *Journal of Asian Earth Sciences*, 44, 3-23.
62. Huntington, K. W., & Lechler, A. R. (2015). Carbonate clumped isotope thermometry in continental tectonics. *Tectonophysics*, 647, 1-20.

63. Huntington, K. W., Eiler, J. M., Affek, H. P., Guo, W., Bonifacie, M., Yeung, L. Y., ... & Came, R. (2009). Methods and limitations of 'clumped' CO<sub>2</sub> isotope ( $\Delta 47$ ) analysis by gas source isotope ratio mass spectrometry. *Journal of Mass Spectrometry*, 44(9), 1318-1329.
64. Huntington, K. W., Budd, D. A., Wernicke, B. P., & Eiler, J. M. (2011). Use of clumped-isotope thermometry to constrain the crystallization temperature of diagenetic calcite. *Journal of Sedimentary Research*, 81(9), 656-669.
65. Hyland, E. G., & Sheldon, N. D. (2013). Coupled CO<sub>2</sub>-climate response during the Early Eocene climatic optimum. *Palaeogeography, Palaeoclimatology, Palaeoecology*, 369, 125-135.
66. IPCC, C. C. (2007). The physical science basis. Contribution of working group I to the fourth assessment report of the Intergovernmental Panel on Climate Change. Cambridge University Press, Cambridge, United Kingdom and New York, NY, USA, 996, 2007.
67. IPCC, W. (2013). IPCC, 2013: summary for policymakers. Climate change.
68. Irving, E., & Wynne, P. J. (1991). Paleomagnetic evidence for motions of parts of the Canadian Cordillera. *Tectonophysics*, 187(1-3), 259-275.
69. Jacques, F. M., Shi, G., Li, H., & Wang, W. (2014). An early–middle Eocene Antarctic summer monsoon: evidence of 'fossil climates'. *Gondwana Research*, 25(4), 1422-1428.
70. Jahren, A. H., & Sternberg, L. S. L. (2003). Humidity estimate for the middle Eocene Arctic rain forest. *Geology*, 31(5), 463.
71. Jahren, A. H., & Sternberg, L. S. L. (2008). Annual patterns within tree rings of the Arctic middle Eocene (ca. 45 ma): Isotopic signatures of precipitation, relative humidity, and deciduousness. *Geology*, 36(2), 99.
72. Jahren, A. H., Byrne, M. C., Graham, H. V., Sternberg, L. S. L., & Summons, R. E. (2009). The environmental water of the middle Eocene Arctic: Evidence from  $\delta D$ ,  $\delta 18O$  and  $\delta 13C$  within specific compounds. *Palaeogeography, Palaeoclimatology, Palaeoecology*, 271(1-2), 96-103.
73. Jahren, A. H. (2007). The Arctic forest of the middle Eocene. *Annual Review of Earth and Planetary Sciences*, 35, 509-540.
74. Kim, S. T., & O'Neil, J. R. (1997). Equilibrium and nonequilibrium oxygen isotope effects in synthetic carbonates. *Geochimica et Cosmochimica Acta*, 61(16), 3461-3475.
75. Kohn, M. J., & Welker, J. M. (2005). On the temperature correlation of  $\delta 18O$  in modern precipitation. *Earth and Planetary Science Letters*, 231(1-2), 87-96.

76. Leng, M. J., & Marshall, J. D. (2004). Palaeoclimate interpretation of stable isotope data from lake sediment archives. *Quaternary Science Reviews*, 23(7-8), 811-831.
77. Ludvigson, G. A., González, L. A., Fowle, D. A., Roberts, J. A., Driese, S. G., Villarreal, M. A., ... & Nordt, L. C. (2013). Paleoclimatic applications and modern process studies of pedogenic siderite. *New Frontiers in Paleopedology and Terrestrial Paleoclimatology*, SEPM (Society for Sedimentary Geology).
78. Marty, D., & Meyer, C. A. (2006). Depositional conditions of carbonate-dominated palustrine sedimentation around the K-T boundary (faciès rognacien, northeastern pyrenean foreland, southwestern France). *Geological Society of America Special Papers*, 416, 169.
79. McInerney, F. A., & Wing, S. L. (2011). The Paleocene-Eocene Thermal Maximum: A perturbation of carbon cycle, climate, and biosphere with implications for the future. *Annual Review of Earth and Planetary Sciences*, 39, 489.
80. McIver, E. E., & Basinger, J. F. (1999). Early Tertiary floral evolution in the Canadian high Arctic. *Annals of the Missouri Botanical Garden*, 523-545.
81. Melillo, J. M., Richmond, T. T., & Yohe, G. (2014). Climate change impacts in the United States. *Third national climate assessment*, 52.
82. Methner, K., Mulch, A., Fiebig, J., Wacker, U., Gerdes, A., Graham, S. A., & Chamberlain, C. P. (2016). Rapid middle Eocene temperature change in western North America. *Earth and Planetary Science Letters*, 450, 132-139.
83. Miall, A. D. (1986). The Eureka Sound Group (Upper Cretaceous-Oligocene), Canadian Arctic Islands. *Bulletin of Canadian Petroleum Geology*, 34(2), 240-270.
84. Miall, A. D. (1991). Stratigraphic sequences and their chronostratigraphic correlation. *Journal of Sedimentary Research*, 61(4), 497-505.
85. Mix, A. C., & Ruddiman, W. F. (1984). Oxygen-Isotope Analyses and Pleistocene Ice Volumes 1. *Quaternary Research*, 21(1), 1-20.
86. Nakai, N., Wada, H., Kiyosu, Y., & Takimoto, M. (1975). Stable isotope of water and studies on the origin and geological history salts in the Lake Vanda area, Antarctica. *Geochemical journal*, 9(1), 7-24.
87. Nelson, S. T., Wood, M. J., Mayo, A. L., Tingey, D. G., & Eggett, D. (2005). Shoreline tufa and tufaglomerate from Pleistocene Lake Bonneville, Utah, USA: stable isotopic and mineralogical records of lake conditions, processes, and climate. *Journal of Quaternary Science*, 20(1), 3-19.
88. Núñez-Betelu, L. K., Hills, L. V., Krause, F. F., & McIntyre, D. J. (1994). Upper Cretaceous paleoshorelines of the northeastern Sverdrup Basin, Ellesmere Island, Canadian Arctic Archipelago.

89. Oehlert, A. M., & Swart, P. K. (2014). Interpreting carbonate and organic carbon isotope covariance in the sedimentary record. *Nature Communications*, 5(1), 1-7.
90. Pagani, M., Pedentchouk, N., Huber, M., Sluijs, A., Schouten, S., Brinkhuis, H., ... Expedition 302 Scientists. (2006). Arctic hydrology during global warming at the Palaeocene/Eocene thermal maximum. *Nature*, 442(7103), 671-675.
91. Parrish, J. T., Hyland, E. G., Chan, M. A., & Hasiotis, S. T. (2018). Stable and clumped isotopes in desert carbonate spring and lake deposits reveal palaeohydrology: A case study of the Lower Jurassic Navajo Sandstone, south-western USA. *Sedimentology*, 66(1), 32-52.
92. Passey, B. H., & Henkes, G. A. (2012). Carbonate clumped isotope bond reordering and geospeedometry. *Earth and Planetary Science Letters*, 351-352, 223-236.
93. Peters, N. A., Huntington, K. W., & Hoke, G. D. (2013). Hot or not? Impact of seasonally variable soil carbonate formation on paleotemperature and O-isotope records from clumped isotope thermometry. *Earth and Planetary Science Letters*, 361, 208-218.
94. Petersen, S. V., Defliese, W. F., Saenger, C., Daëron, M., Huntington, K. W., John, C. M., ... & Olack, G. A. (2019). Effects of improved  $^{17}\text{O}$  correction on interlaboratory agreement in clumped isotope calibrations, estimates of mineral-specific offsets, and temperature dependence of acid digestion fractionation. *Geochemistry, Geophysics, Geosystems*, 20(7), 3495-3519.
95. Platt, N.H., 1989. Lacustrine carbonates and pedogenesis: sedimentology and origin of palustrine deposits from the early Cretaceous Rupelo Formation, W Cameros Basin, N Spain. *Sedimentology* 36, 665 – 684.
96. Price, G. D., & Passey, B. H. (2013). Dynamic polar climates in a greenhouse world: Evidence from clumped isotope thermometry of early Cretaceous belemnites. *Geology*, 41(8), 923-926.
97. Quade, J., Eiler, J., Daeron, M., & Achyuthan, H. (2013). The clumped isotope geothermometer in soil and paleosol carbonate. *Geochimica et Cosmochimica Acta*, 105, 92-107.
98. Riediger, C. L., & Bustin, R. M. (1987). The Eureka Sound Formation, southern Ellesmere Island. *Bulletin of Canadian Petroleum Geology*, 35(2), 123-142.
99. Reinhardt, L., Estrada, S., Andrulleit, H., Dohrmann, R., Piepjohn, K., von Gosen, W., ... & Davis, B. (2013). Altered volcanic ashes in Palaeocene and Eocene sediments of the Eureka Sound Group (Ellesmere Island, Nunavut, Arctic Canada). *Zeitschrift der deutschen Gesellschaft für Geowissenschaften*, 164(1), 131-147.
100. Ricketts, B. D., & Stephenson, R. A. (1994). The demise of Sverdrup Basin; Late Cretaceous-Paleogene sequence stratigraphy and forward modeling. *Journal of Sedimentary Research*, 64(4b), 516-530.

101. Ricketts, B. D., & McIntyre, D. J. (1986). The Eureka Sound Group of eastern Axel Heiberg Island: new data on the Eureka Orogeny. Geological Survey of Canada Paper, 86, 405-410.
102. Ricketts, B. D., (1986). New formations in the Eureka Sound Group, Canadian Arctic Islands. In: Current Research, Part B: Geological Survey of Canada, pp.363-374. Paper 86-1B.
103. Rozanski, K., Araguás Araguás, L., & Gonfiantini, R. (1993). Isotopic patterns in modern global precipitation. *Climate change in continental isotopic records*, 78, 1-36.
104. Ryan, W. B. F., S.M. Carbotte, J. Coplan, S. O'Hara, A. Melkonian, R. Arko, R.A. Weissel, V. Ferrini, A. Goodwillie, F. Nitsche, J. Bonczkowski, and R. Zemsky. (2009). Global Multi-Resolution Topography (GMRT) synthesis data set, Geochemistry, Geophysics, Geosystems. 10, Q03014. Program: GeoMapApp
105. Schaetzl, R., & Anderson, S. Soils. Genesis and geomorphology. (2005). Ch, 15, 619-652.
106. Schauer, A. J., Kelson, J., Saenger, C., & Huntington, K. W. (2016). Choice of 17O correction affects clumped isotope ( $\Delta 47$ ) values of CO<sub>2</sub> measured with mass spectrometry. *Rapid Communications in Mass Spectrometry*, 30(24), 2607-2616.
107. Schubert, B. A., Jahren, A. H., Eberle, J. J., Sternberg, L. S. L., & Eberth, D. A. (2012). A summertime rainy season in the Arctic forests of the Eocene. *Geology*, 40(6), 523-526.
108. Shellito, C. J., & Sloan, L. C. (2006). Reconstructing a lost Eocene Paradise, Part II: On the utility of dynamic global vegetation models in pre-Quaternary climate studies. *Global and Planetary Change*, 50(1-2), 18-32.
109. Shellito, C. J., Sloan, L. C., & Huber, M. (2003). Climate model sensitivity to atmospheric CO<sub>2</sub> levels in the early-middle Paleogene. *Palaeogeography, Palaeoclimatology, Palaeoecology*, 193(1), 113-123.
110. Stephenson, R. A., Ricketts, B., Cloetingh, S. A. P. L., & Beekman, F. (1990). Lithosphere folds in the Eureka Orogen, Arctic Canada. *Geology*, 18(7), 603-606.
111. Stewart, K. R., Embry, A. F., Goodarzi, F., & Skibo, D. N. (1992). Evaluation of organic maturity and hydrocarbon source potential of the Ringnes Formation, Sverdrup Basin, Arctic Canada. *Organic Geochemistry*, 18(3), 317-332.
112. Stolper, D. A., & Eiler, J. M. (2015). The kinetics of solid-state isotope-exchange reactions for clumped isotopes: A study of inorganic calcites and apatites from natural and experimental samples. *American Journal of Science*, 315(5), 363-411.

113. Tandon, S. K., & Andrews, J. E. (2001). Lithofacies associations and stable isotopes of palustrine and calcrete carbonates: examples from an Indian Maastrichtian regolith. *Sedimentology*, 48(2), 339-355.
114. Tauxe, L., & Clark, D. R. (1987). New paleomagnetic results from the Eureka Sound Group: Implications for the age of early Tertiary Arctic biota. *Geological Society of America Bulletin*, 99(6), 739-747.
115. Tipple, B. J., Meyers, S. R., & Pagani, M. (2010). Carbon isotope ratio of Cenozoic CO<sub>2</sub>: A comparative evaluation of available geochemical proxies. *Paleoceanography*, 25(3).
116. Trettin, H. P., & Balkwill, H. R. (1979). Contributions to the tectonic history of the Innuitian Province, Arctic Canada. *Canadian Journal of Earth Sciences*, 16(3), 748-769.
117. Tripathi, A. K., Hill, P. S., Eagle, R. A., Mosenfelder, J. L., Tang, J., Schauble, E. A., ... & Ries, J. B. (2015). Beyond temperature: Clumped isotope signatures in dissolved inorganic carbon species and the influence of solution chemistry on carbonate mineral composition. *Geochimica et Cosmochimica Acta*, 166, 344-371.
118. Urban, M. A., Nelson, D. M., Jiménez-Moreno, G., Châteauneuf, J. J., Pearson, A., & Hu, F. S. (2010). Isotopic evidence of C<sub>4</sub> grasses in southwestern Europe during the early Oligocene–middle Miocene. *Geology*, 38(12), 1091-1094.
119. Von Gosen, W., Reinhardt, L., Piepjohn, K., & Schmitz, M. D. (2019). Paleogene sedimentation and Eureka deformation in the Stenkul Fiord area of southeastern Ellesmere Island (Canadian Arctic): Evidence for a polyphase history. *Circum-Arctic Structural Events: Tectonic Evolution of the Arctic Margins and Trans-Arctic Links with Adjacent Orogens*, 541, 325.
120. West, R. M., Dawson, MR, D., & Hutchison, JH. (1977). Fossils from the Paleogene Eureka Sound Formation, NWT, Canada: occurrence, climatic and paleogeographic implications.
121. West, R. M., Dawson, M. R., Hickey, L. J., & Miall, A. D. (1981). Upper Cretaceous and Paleogene sedimentary rocks, eastern Canadian Arctic and related North Atlantic areas.
122. West, C. K., Greenwood, D. R., & Basinger, J. F. (2015). Was the Arctic Eocene 'rainforest' monsoonal? Estimates of seasonal precipitation from early Eocene megaflores from Ellesmere Island, Nunavut. *Earth and Planetary Science Letters*, 427, 18-30.
123. West, C. K. (2019). The late Paleocene to early Eocene polar forests of Canada: A paleobotanical reconstruction of climate and ecosystems (Doctoral dissertation, University of Saskatchewan).

124. Willard, D. A., Donders, T. H., Reichgelt, T., Greenwood, D. R., Sangiorgi, F., Peterse, F., ... & Sluijs, A. (2019). Arctic vegetation, temperature, and hydrology during early Eocene transient global warming events. *Global and planetary change*, 178, 139-152.
125. Winguth, A., Shellito, C., Shields, C., & Winguth, C. (2010). Climate response at the Paleocene–Eocene thermal maximum to greenhouse gas forcing—a model study with CCSM3. *Journal of Climate*, 23(10), 2562-2584.
126. Winkelstern, I. Z., & Lohmann, K. C. (2016). Shallow burial alteration of dolomite and limestone clumped isotope geochemistry. *Geology*, 44(6), 467-470.
127. Wolfe, J. A. (1994). Tertiary climatic changes at middle latitudes of western North America. *Palaeogeography, Palaeoclimatology, Palaeoecology*, 108(3-4), 195-205.
128. Wright, V.P., Alonso-Zarza, A.M., Sanz, M.E., Calvo, J.P., 1997. Diagenesis of Late Miocene micritic lacustrine carbonates, Madrid Basin, Spain. *Sedimentary Geology* 114, 81 – 95.
129. Young, S.B. 1971. The vascular flora of St. Lawrence Island with special reference to floristic zonation in the arctic regions. *Contributions from the Gray Herbarium*. 201:11-115.
130. Zachos, J., Pagani, M., Sloan, L., Thomas, E., & Billups, K. (2001). Trends, rhythms, and aberrations in global climate 65 Ma to present. *Science*, 292(5517), 686-693.
131. Zachos, J. C., Dickens, G. R., & Zeebe, R. E. (2008). An early Cenozoic perspective on greenhouse warming and carbon-cycle dynamics. *Nature*, 451(7176), 279-283.
132. Zhang, S., & Wang, B. (2008). Global summer monsoon rainy seasons. *International Journal of Climatology: A Journal of the Royal Meteorological Society*, 28(12), 1563-1578.
133. Zimov, S. A., Schuur, E. A., & Chapin III, F. S. (2006). Permafrost and the global carbon budget. *Science(Washington)*, 312(5780), 1612-1613.

**APPENDICES**

## APPENDIX A. Clumped Isotope Reordering Model

### Clumped Isotope Reordering Model Code and Parameters:

```

% Ashly Padgett
% Clumped Isotope Reordering Model - Burial through Time

% MGB-CC-1 optical calcite values, compositionally homogenous
%     MGB-CC-1 optical: kref = 2.92*10^(-6), Tref = 699.7 K
%     ActivationEnergy Ea = 197 kJ/mol

% NE-CC-1 void-filling spar calcite, labile, heterogeneous
%     NE-CC-1 labile spar: kref = 1.42*10^(-5), Tref = 745.9 K
%     ActivationEnergy Ea = 288 kJ/mol

% GENERAL VARIABLE DEFINITIONS
% Di = D47 value of mineral at timestep i
% The clumped values that the model actively calculates and saves as an array
% Di_o = starting formation temp of mineral converted to D47 with EQNS
% Formation temp of 2 C or 275 K, matches a clumped val of 0.7651
% Di_eq = Equilibrium value at i
% Di_eq = ((-3.407*10^9)/T^4)+((2.365*10^7)/T^3)-((2.607*10^3)/T^2)-(5.880/T)+0.280;

% dt = timestep at which cooling rate is applied, iterates at a million year timestep
% kref = rate constant for calcites at predetermined temp Tref
% Tref = reference temperature
% R = gas constant 8.314 J/mol
% Ea = Activation Energy using Arrhenius parameter for C-O reordering
% T = closure temperature, changes through time based on burial/uplift

% EQNS Used from Passey & Henkes (2012)
% EQN 5:
% Di_eq = ((-3.407*10^9)/T^4)+((2.365*10^7)/T^3)-((2.607*10^3)/T^2)-(5.880/T)+0.280;
% EQN 13:
% Di=(Di_o-Di_eq)*exp(-dt*kref*exp((Ea/R)*((1/Tref)-(1/T))))+Di_eq

% Defining variables and parameters
dt = 1000000*(3.154*10^7); % timestep, seconds in one million years
R = 0.008314; % Gas Constant in kJ/mol
kref = 2.92*10^(-6); % Rate constant - switch out based on optical/labile
Tref = 699.7; % in Kelvin - switch out based on O/L
Ea = 197; % Activation Energy optical kJ/mol - switch out based on O/L
surfaceT = 275; % in Kelvin, 2C CMMT formation at the surface
burialT = 431.15; % ADJUST TO FIND MAX BURIAL TEMP, in Kelvin

event1=10; % at mil years your rock reaches max burial depth
event2=20; % at mil years uplift begins
event3=45; % at mil years it reaches the surface

Tvector(1:event1)=[surfaceT:(burialT-surfaceT)/(event1-1):burialT];
Tvector(event1+1:event2)=[burialT];
Tvector(event2+1:event3)=[burialT:-((burialT-surfaceT)/(event3-event2-1)):surfaceT];
Tvector(event3+1:60)=[surfaceT];

Di_o = 0.7651; % initial clumped isotope value corresponding to 2C CMMT carbonate formation
Di_eq = ((-3.407*10^9)./Tvector.^4)+((2.365*10^7)./Tvector.^3)-((2.607*10^3)./Tvector.^2)-
(5.880./Tvector)+0.280;
Di_outputL = [];

n = 60; % running model for 60 million years

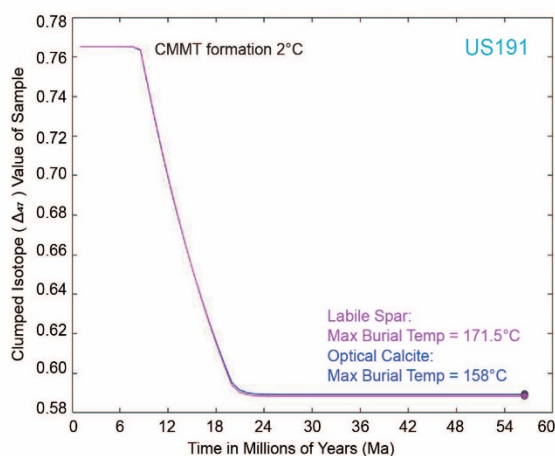
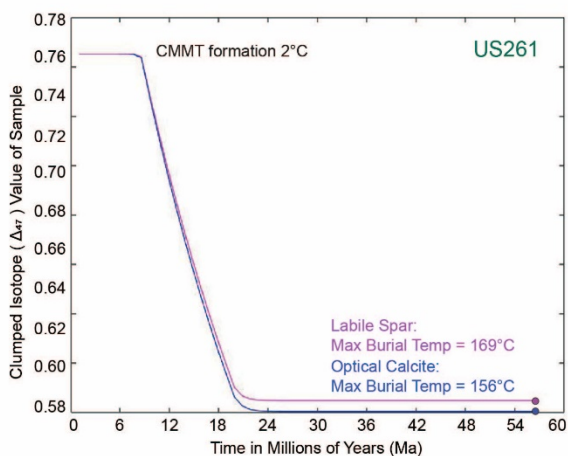
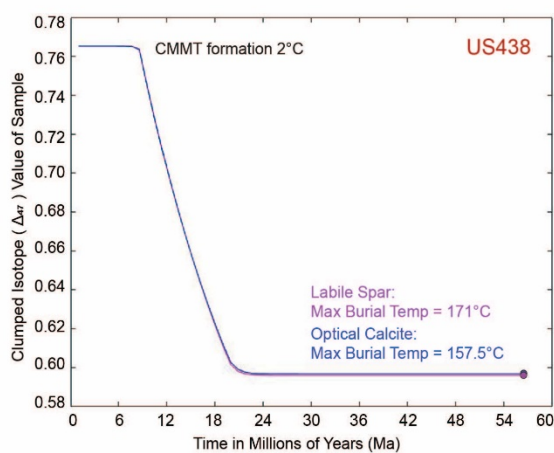
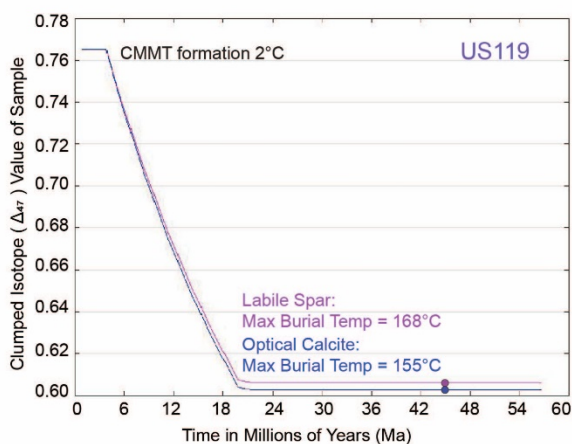
for time = 1:n
    if time == 1
        Di(time)=(Di_o-Di_eq(time))*exp(-dt*kref*exp((Ea/R)*((1/Tref)-(1/Tvector(time)))))+Di_eq(time);
    else
        Di(time)=(Di(time-1)-Di_eq(time))*exp(-dt*kref*exp((Ea/R)*((1/Tref)-
(1/Tvector(time)))))+Di_eq(time);
    end
    Di_outputL(time) = Di(time);
end

xArray = (1:n);
TimeAxis = dt*xArray;
plot(TimeAxis, Di_outputL, 'b');

```

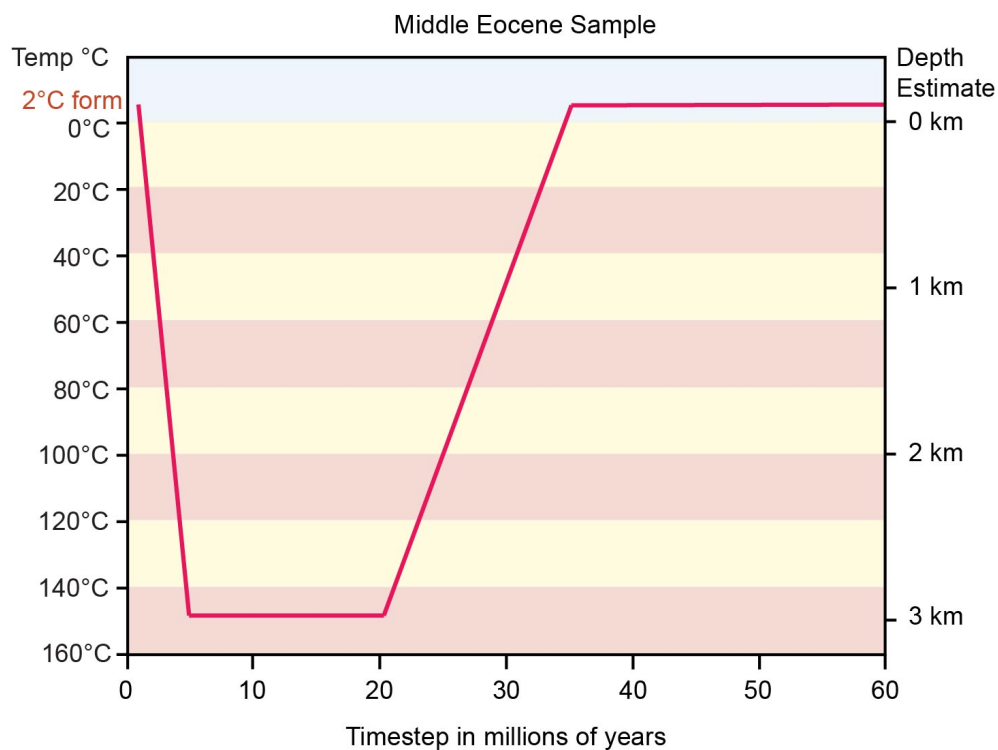
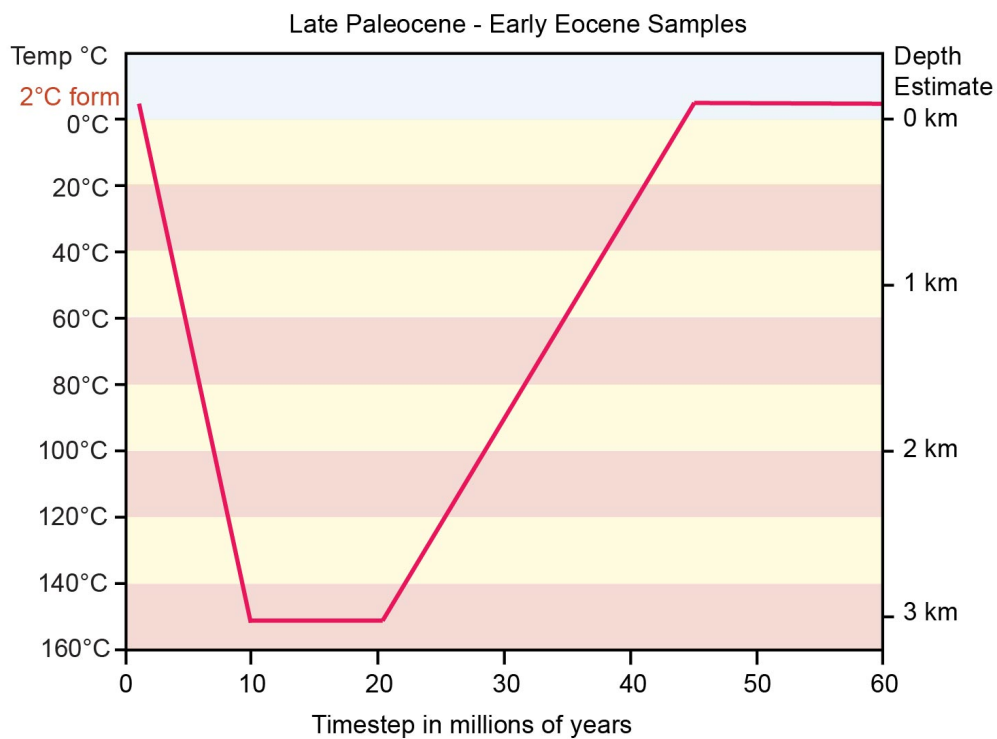
## Appendix A

Model simulation results for Optical Calcite plotted against Labile Spar to compare maximum burial temperatures. The parameters  $k_{ref}$  (rate constant for calcites at a predetermined  $T_{ref}$ ),  $T_{ref}$  (reference temperature),  $E_a$  (activation energy using Arrhenius parameter for C-O reordering) change based on the material (Optical or Labile). US119 is Buchanan Lake (45 Ma), US438 is Stenkul Fiord (56 Ma), US 261 is Lake Hazen (56 Ma), and US191 is Fosheim Anticline (56 Ma).



## Appendix A

Sample temperature paths used to model realistic burial and uplift events:



## APPENDIX B. Listed Data Output

Sample Name	Subsample	Carbon (VPDB)	Oxygen (VPDB)	D47 CDES (Final)	Lab Location
US119	I	2.4524	-19.4811	0.661	NC
US119	I	2.4395	-19.1407	0.606	NC
US119	II	2.69	-18.31	X	NC
US119	II	2.68	-18.25	X	NC
US119	II	2.68	-17.85		NC
US119	III	2.91		0.5612	UW
US119	III	3.26		0.58732	UW
US444	I	4.6587	-23.3867	0.6	NC
US444	I	4.6759	-23.3832	0.681	NC
US444	II	4.88	-22.98	X	NC
US444	II	4.79	-22.73		NC
US444	III	5.09		0.54214	UW
US444	III	5.07		0.57108	UW
US107	I	2.2715	-16.6122	0.546	NC
US107	I	2.2229	-16.4777	0.578	NC
US107	II	2.59	-16.78	X	NC
US107	II	2.78	-17.29	X	NC
US107	II	2.76	-17.15		NC
US107	III	2.58		0.51483	UW
US107	III	2.99		0.47881	UW
US108	I	2.894	-17.2516	0.48308	NC
US108	I	2.8842	-17.2869	0.45631	NC
US108	II	3.07	-17.37	X	NC
US108	II	3.06	-17.2		NC
US108	II	3.16	-17.47		NC
US108	II	3.14	-17.31		NC
US108	III	3.35		0.644	UW
US108	III	3.08		0.605	UW
US108	III	3.25		0.601	UW
US435	I	7.611	-18.2895	0.613	NC
US435	I	7.6151	-18.2984	0.564	NC
US435	II	7.86	-17.96	X	NC
US435	II	7.86	-17.8	X	NC
US435	II	7.83	-17.98	X	NC
US435	III	8.67		0.52459	UW
US435	III	8.2		0.56549	UW
US435	III	7.97			UW
US436	I	4.39	-17.87	0.531	NC

## Appendix B (continued)

Sample Name	Subsample	Carbon (VPDB)	Oxygen (VPDB)	D47 CDES (Final)	Lab Location
US436	I	4.51	-17.9977	0.584	NC
US436	II	4.38	-16.27	X	NC
US436	II	4.41	-16.43		NC
US436	III	7.3362		0.52649	UW
US436	III	7.4776		0.52571	UW
US438	I	6.4079	-17.3414	0.563	NC
US438	I	6.4614	-17.2942	0.696	NC
US438	I	6.3746	-17.4073	X	NC
US438	II	6.15	-16.78	0.637	NC
US438	II	6.08	-16.5	0.633	NC
US438	III	6.29		0.51738	UW
US438	III	6.45		0.56533	UW
US438	III	6.15		0.5635	UW
US438	III	6.41			UW
US261	I	12.366	-15.754	0.73	NC
US261	I	12.3621	-15.7142	X	NC
US261	I	12.4456	-15.7045		NC
US261	II	12.53	-15.49	X	NC
US261	III	12.59		0.60591	UW
US261	III	11.8		0.56087	UW
US261	III	12.17		0.58806	UW
US191	I	7.4362	-18.6469	0.693	NC
US191	I	7.2785	-18.8369	0.596	NC
US191	I	7.2839	-18.5651	X	NC
US191	II	7.32	-18.88	X	NC
US191	II	7.23	-18.77	X	NC
US191	III	7.27		0.53308	UW
US191	III	7.67		0.57476	UW
US191	III	6.32		0.55042	UW
US111	I	3.1094	-17.7448	0.594	NC
US111	I	3.0921	-17.5656	0.601	NC
US111	II	2.19	-16.29	0.584	NC
US111	II	2.67	-17.25	X	NC
US111	II	2.65	-17.03		NC
US111	III	2.34		0.5045	UW
US111	III	2.71		0.49147	UW
US251	I	1.2304	-19.6212	0.586	NC
US251	I	1.2057	-19.6044	0.538	NC

## Appendix B (continued)

Sample Name	Subsample	Carbon (VPDB)	Oxygen (VPDB)	D47 CDES (Final)	Lab Location
US251	II	1.59	-19.52	X	NC
US251	II	1.52	-18.68	X	NC
US251	III	1.72		0.4582	UW
US251	III	1.57		0.43818	UW
US422	I	2.0215	-15.4511	0.538	NC
US422	I	2.048	-15.5798	0.59	NC
US422	II	2.22	-15.49	0.627	NC
US422	II	2.13	-14.31	0.629	NC
US422	III	1.99		0.49843	UW
US422	III	2.1		0.53562	UW
US422	III	2.06		X	UW
US422	III	2.12			UW
US196	I	2.3389	-19.7629	0.656	NC
US196	I	2.3543	-19.9176	0.661	NC
US196	II	2.46	-19.26	0.675	NC
US196	II	2.47	-19.37	X	NC
US196	II	2.41	-19.17		NC
US196	II	2.35	-18.5		NC
US196	III	2.59		0.54175	UW
US196	III	2.53		0.55725	UW
US196	III	2.55			UW
US176	I	-4.3533	-18.5932		NC
US176	I	-4.1472	-18.8876		NC
US176	II	X	X	X	NC
US176	III	-5.01	-21.55	0.52515	UW
US176	III	-4.72	-22.26	0.52492	UW